TADF OLEDs: characterization, modelling and detailed degradation analysis

Stefano Sem

Sem, Stefano. 2023. “TADF OLEDs: characterization, modelling and detailed degradation analysis.” Augsburg: Universität Augsburg.

TADF OLEDs:
Characterization, Modelling and Detailed Degradation Analysis

Dissertation

zur Erlangung des akademischen Grades
Dr. rer. nat.

eingereicht an der
Mathematisch-Naturwissenschaftlich-Technischen Fakultät
der Universität Augsburg

vorgelegt von
Stefano Sem

Augsburg, Februar 2023

1. Gutachter: Prof. Dr. Wolfgang Brütting
2. Gutachter: Prof. Dr. Beat Ruhstaller
Tag der mündlichen Prüfung: 23. Februar 2023

CONTENTS

LIST OF FIGURES

LIST OF TABLES

ABSTRACT

The need of high quality and efficient displays is continuously increasing. The organic light-emitting diode (OLED) technology is certainly one of the most important in this sense, thanks to their high contrast, excellent color purity and wide viewing angle. Despite being already widely used in commercial products, scientific research on OLED materials is still ongoing to improve their efficiency and durability.

A new technology which might replace currently used emissive materials in OLED is the so called thermally-activated delayed fluorescence (TADF). With these emitters, the display efficiency can be improved without the need of expensive and pollutant heavy metal atoms. This PhD project is focused on these materials and their use in OLEDs. The study of TADF OLEDs presented in this thesis has been structured in three main parts.

The first study allows to clarify a frequent misconception about these emitters: the portion of excitons leading to an emissive event, usually approximated to 100%, can actually be much lower when electrically excited. A method to estimate this value is provided from the analysis of transient and steady state optical measurements.

In a state-of-the-art OLED, the emission layer (EML) consists of two or more components. The adjustment of each material component and the optimization of the concentration largely impact the OLED performance. In the second study, OLEDs containing different concentrations of the TADF molecule in the emissive layer are investigated. Several experimental techniques are used and, with the use of software simulations the effect of emission layer composition on the charge and excitonic processes is analysed.

The key aspect which must be improved in order to make TADF a suitable technology in commercial products, is the lifetime. Two studies about this topic have been included in this thesis.

To effectively measure the lifetime of emissive devices, one would need to operate them for several thousands of hours. This approach is definitely not applicable on a large scale, when a multitude of different devices need to be tested, since it requires a lot of time and resources. Such characterization is therefore typically done under accelerated stressing conditions, with high currents and/or temperatures. The use of appropriate scaling laws allows to estimate the durability of the device in standard operating conditions from the accelerated ones. In the first study described in this work, several identical TADF OLEDs have been stressed with different current at different temperature, and the complete set of luminance decay is fed into a global fitting algorithm. With this approach the expected lifetime can be estimated in a shorter amount of time, yet with a high accuracy.

To improve the device lifetime, a detailed understanding of the processes causing it is necessary. The second study on device lifetime goes more into detail of the degradation processes occurring in a specific TADF OLED stack. The devices are stressed with constant current, and during stressing interruption a series of experimental techniques are used. Electrical device simulations are used to model these OLEDs and qualitatively identify the degradation causes. Specifically, it is found that the generation of trap states causes a variation of the charge injection and accumulation inside the device.

1

INTRODUCTION

In the first part of this introduction I will briefly dive into the organic light emitting diodes (OLEDs) technology, compare it with liquid crystal displays (LCDs) and describe the different generations which brought us to the current level of efficiency and lifetime. In the second part, the general structure of an OLED is introduced together with the concept of excitons. Finally, the physics behind thermally activated delayed fluorescence (TADF) emitters is described in detail, since this luminescence mechanism is at the heart of all the studies carried out in this PhD work and also the European project TADFlife, from which this work received financial support.

1.1 DISPLAY TECHNOLOGIES

The display market is continuously growing. At the moment of writing it is valued 148.4 billion USD, and it is expected to reach 177.1 billion USD by 2026.[1] Displays are nowadays used everywhere: TVs, laptops, phones, tablets, medical-based equipment and virtual/augmented reality (VR/AR). Scientific research is extremely important in order to meet the demand for displays with better quality, higher efficiencies and be able to meet requirements for new applications.

In the last decades different technologies have been developed. The most common technology, talking about flat panels, is liquid crystal displays (LCDs). In an LCD several components are necessary: a back-light, polarizers, liquid crystal cells and color filters. The polarized light originated from the back of the screen passes through the liquid crystal cells, that are placed before the second polarizer. The application of an electric field across the liquid crystal cell induces a rotation of the polarization of the light. In this way the intensity of the light leaving the screen can be controlled. In color displays each pixel is composed by three sub-pixels with a different color filter in front. This brief, and surely oversimplified, description of LCDs is necessary to fully understand the differences, advantages and weaknesses of the OLED technology, which is the subject of this thesis.

An OLED is an thin film device made of organic materials (carbon-based compounds). It consists of several organic layers sandwiched between two electrodes and when current is applied to the device, light is generated and emitted. The variate of colors in a display are achieved by a combination of three sub-pixels (red, green and blue) and, in contrast with the LCD technology, each sub-pixel is an emitting device, therefore no back-light is necessary. This fact allows OLED displays to have two really important advantages compared to LCDs: an almost infinite contrast ratio (since when a black image is displayed the pixel is literally switched off) and a wider viewing angle.[2, 3] Another key property of OLEDs is the possibility to produce flexible displays. At the moment of writing already several devices containing flexible displays are on the market, such as foldable phones or tablets. Additional advantages of this technology are the very fast response time, important especially in the gaming industry, the possibility to produce paper-thin or transparent displays and the high pixel density. On the other hand, there are a few weaknesses of this technology compared to LCDs, such as: shorter lifetime - especially caused by the blue sub-pixel - and slightly poorer color accuracy. Additionally, the cost of OLED screens is still higher than LCDs. The main reason being the higher level of maturity of LCD technology with its large fabrication capacity. The cost difference is expected to further decrease in coming years as the production volume of OLED displays increases.

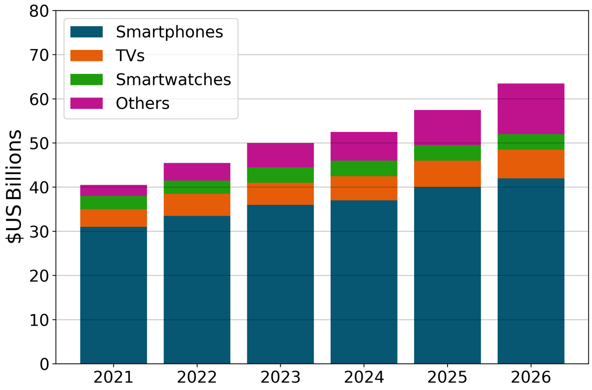

Figure 1.1: OLED market forecasts 2021-2026. Others contains: automotive, notebook PC, gaming, tablet, AR/VR, monitor, others. Adapted from source: DSCC-2021.

1.2 OLED GENERATIONS

In the last decades, continuous research has brought the OLED technology on the market, specifically in terms of new materials, device concept and improved manufacturing. In Figure 1.1 the OLED market forecasts clearly show an increase in any application. When evaluating a new emissive molecule or device structure, different characteristics are evaluated: device efficiency, lifetime, the color coordinates and environmental issues, which of course must be avoided.

Blue emitters have always been challenging in OLED displays in respect of efficiency and lifetime.[4] In the first generation of emitters, purely fluorescent materials were used. Fluorescent emitters have an intrinsic limit in the internal quantum efficiency (IQE) of 25%, and considering the fact that only a reduced portion of light is effectively able to leave the device in the correct direction, the maximum external quantum efficiency (EQE) of this type of OLED was only ~ 5 %.[5] With the second generation, the use of heavy-metal compounds induced phosphorescence to be the main physical process behind emission, and larger efficiencies were reached.[6] However, the long living triplet states, combined with the large bandgap required in blue emitters, give rise to high energy excited states, which might cause a degradation of the OLED.[7] Blue pixels in nowaday's displays employ a combination of fluorescent (1st generation) and triplet-triplet-fusion (TTF) emitters, in which TTF allows to reach a theoretical IQE limit of 62.5%.

In the 3rd generation, TADF emitters are used. TADF OLEDs have gained the attention of both academic and industrial research in the last years.[8, 9] The main property of these materials is their ability to up-convert non-radiative triplet states into radiative singlet ones, which allows moving the limit of 25% internal quantum efficiency in normal fluorescent OLEDs up to theoretically 100%.[10, 11] With respect to the 2ndnd generation, the use of heavy-metal atoms, which are not ideal for environmental and high cost reasons, is avoided. These factors make TADF a very interesting technology for replacing fluorescent and phosphorescent emitters in today's commercial OLED products. However, the device stability and efficiency has still to be improved and both are within the focus of active ongoing research.[12, 13]

In recent years the so called hyperfluorescent technology has been introduced. It consists of a combination between TADF and other materials and they are usually indicated as 4th generation. In Section 1.6.3 a brief description of this technology is provided.

1.3 MOTIVATION

The goal of this PhD project is to gain insights into device mechanisms and processes in TADF OLEDs, which can help the community to improve the efficiency and lifetime of these devices. To tackle this goal I first studied the emissive material, then the performances of actual OLEDs, and at the end the degradation of these devices.

The first study reported in this thesis (Chapter 3) focuses on TADF films (not embedded in a complete device). In particular, the effect of non-radiative decay rates on the EQE is evaluated. Additionally, a fitting algorithm was implemented to estimate the exciton decay rates from optical experiments with single film devices.

The performance of an OLED depends not only on the emissive layer, but also on the entire stack. Specifically, charge injection and transport, excitonic and other effect such as spontaneous orientation polarization (SOP), play an important role. In order to analyse these effects, a simple evaluation of the efficiency or standard current-voltage-luminance (JVL) is not sufficient. Instead, a more sophisticated approach is required to draw precise conclusions. In Chapter 4 an in-depth analysis is provided, where a combination of several experimental techniques and simulations allows a detailed investigation of an OLED stack. This study has been conducted on four OLEDs with a different concentration of the emissive molecule.

As clearly stated in this introduction, it is fundamentally important to understand and reduce the degradation of TADF emitters. This topic is faced in the last two chapters of this thesis. In the first part of this study (Chapter 5) the device degradation under different accelerated stressing conditions has been investigated. The data analysis is done using a global fit algorithm, which is based on a widely-used analytical model describing the degradation of organic and inorganic LEDs. With this approach two main results can be achieved: provide an estimation of the OLED's lifetime in standard operation conditions from accelerated ones; estimate the luminance decay at any specific temperature and current. The second part of this study (Chapter 6) is centered on understanding the degradation mechanisms in a TADF device. An advanced electro-optical characterization is performed during stress interruptions in which steady-state, transient and impedance measurements are carried out. With the support of device modeling the physical processes happening during degradation can be identified.

1.4 BASIC OLED STRUCTURE

An OLED is a multi-layer structure where each layer has its specific purpose (see Figure 1.2). Starting from the substrate side, we have the bottom contact, the hole-injection layer (HIL), the hole-transport layer (HTL), the electron-blocking layer (EBL), the emissive layer (EML), the hole-blocking layer (HBL), the electron-transport layer (ETL), the electron-injection layer (EIL) and the top contact. Upon applying a sufficiently high voltage between the electrodes, electrons and holes are injected through the respective injection and transport layers. The encounter of an electron and a hole inside the EML generates an exciton, and when it decays radiatively a photon is emitted. Each layer indicated before must therefore be optimized in order to obtain good performance in terms of efficiency, stability and emitted color. [14]

In the following, a brief description of each layer is given. In Figure 1.2, a schematics of the injection-exciton formation-recombination processes are shown in the energy diagram. As anode, indium-tin-oxide (ITO) is the most widely used material. Its electrical conductivity, optical transparency and high work function make this material a perfect solution for display applications. [16] OLED samples fabricated for research, as the ones studied in this thesis, are made by evaporating the organic layers on top of glass substrates which already

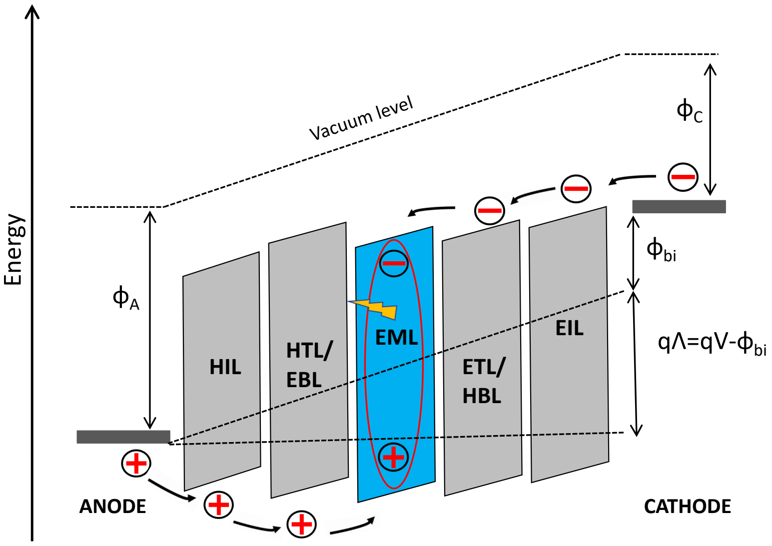

Figure 1.2: (a) Energy diagram of an OLED during operation adapted from [15]. Electrons and holes are injected from the cathode and the anode respectively. In the EML the two charge carrier types meet and excitons are formed. When an exciton decays radiatively, a photon is emitted. Φ_A: anode work function, Φ_C: cathode work function, Φ_{bi}: built-in potential, V: applied voltage, Λ: effective voltage across the OLED, q: elementary charge.

contain predefined ITO structures. As cathode, metals with a low work function are used, in order to facilitate injection of electrons into the device. Often, materials like calcium or aluminum are used.[17] In order to promote injection of holes to the HOMO level and electrons to the LUMO level of the organic materials, HIL and EIL are necessary. Frequently PEDOT:PSS is spin-coated on top of the ITO contact as HIL. [18] The EIL consist of a few nanometers of LiF. [19] A crucial role in the OLED's performance is played by the transport layers. A good transport layer must possess several characteristics: high charge carrier mobility, to ensure balanced charge injection; a good alignment of the HOMO(HTL)/LUMO(ETL) level with respect to the EML's ones, to guarantee low charge accumulation and good injection; high thermal stability, to avoid fast degradation[20]; high exciton energies, to ensure no diffusion of excitons from the EML. Regarding the HTL, the most common materials used in OLEDs are triarylamine derivatives, spiro-derivatives, carbazole derivatives and fluorene derivatives like 1,1-bis[(di-4-tolylamino)phenyl]cyclohexane (TAPC), N,N′-bis-(1-naphthyl)-N,N′-diphenyl benzidine (α-NPD), tris(4-carbazoyl-9-ylphenyl)amine (TCTA), N,N′-di-1-naphthalenyl-N,N′-diphenyl-[1,1′:4′,1″:4″,1‴-quaterphenyl]-4,4‴-diamine (4P-NPD), N,N′-bis(I)naphthyl)-N,N′-diphenyl-1,1′-biphenyl-4,4′-diamine (NPB),N,N′-bis(metatolyl)-N,N′-diphenylbenzidine (TPD), 4,4′,4″-tris((3-methylphenyl)phenyl amino)triphenylamine (m-MTDATA) etc.[20–23] The typical hole mobility of these HTLs is roughly one or two order of magnitude higher than the electron mobility of ETLs. Commonly used ETLs are: tris(8-quinolinolato) aluminum (Alq_3), 4-biphenyloxolate aluminium(III) bis(2-methyl-8-quinolinato)-4-phenylphenolate (BAlq) 1,3,5-tri(phenyl-2-benzimidazole)benzene (TPBi), 3-phenyl-4(10-naphthyl)-5-phenyl-1,2,4-triazole (TAZ), 4,7-Diphenyl-1,10-phenanthrolin (BPhen), and 2,9-dimethyl-4,7-diphenyl-1,10-phenanthroline (BCP). [20, 24–26] Additional layers could be included to block charge carriers escaping the EML. In this case an HBL might be evaporated in between the ETL and the EML, and an EBL in between the HTL and the EML. A good HBL must have a deep HOMO level, such that the energy barrier from the HOMO of the EML is sufficiently high to guarantee that no holes escape to the cathode side (on the other side, the energy barrier from the LUMO of the EML to the one of the EBL must be large enough). It is important that the HBL and EBL possess also a LUMO/HOMO which is aligned with the one at the respective transport layer and the EML, such that energy barriers are avoided. [27] In most cases, the previously mentioned transport layers play the role of blocking layers as well, so that the two properties can be combined into a single layer.

The EML is the layer where electrons and holes recombine, generating light. The EML is usually composed by the emissive material, embedded into a host matrix. The choice of the host molecule is extremely important for several reasons, which are briefly described in the following paragraphs. One of the most important property of the host material is the triplet energy. In order to confine triplet excitons on the emissive molecule, a large triplet energy is required. In case of blue emitters a triplet energy of at least 3 eV is necessary.[28] Another important aspect of the host material is its ability to ensure a balanced charge transport. This characteristic is important for the OLED operation in terms of efficiency and lifetime. Ideally, charge transport occurs on host molecules, and therefore a balanced electron and hole mobility is desirable.[29, 30] However, having transport on the host or guest molecules might depend on the relative concentration between the two, as investigated in Chapter 4.[31]

Besides the electrical characteristics, it has been shown that the host molecule can also influence the energetic states of the emissive molecule, which results in a change of the excitonic transfer properties. [32, 33]

The most important component of an OLED, the emissive material, is described in Section 1.6.

1.5 EXCITONS

An exciton is a quasi-particle which is generated from an encounter of an electron and an hole. The two charges are attracted to each other thanks to their Coulomb interaction. Excitons can be distinguished in two types, depending on the properties of the material in which they form: Wannier-Mott excitons and Frenkel excitons. Wannier-Mott excitons form usually in materials which possess a large dielectric constant (≈ 11-16), like inorganic semiconductors. The large dielectric constant causes the binding energy of the exciton to be small (14.7 meV for Si, 4.7 meV for GaAs, 2.7 meV for Ge) and therefore the distance between the positive and negative charges is large (4-10 nm). Frenkel excitons instead form in materials with a low dielectric constant (≈ 3-4), like organic semiconductors. In this case the binding energy of the exciton is much larger and therefore the electron-hole pair is closer, forming small-range excitons (0.5-1 nm).

Since the exciton is a composition of two particles with half-integer spin, an electron and a hole, the total spin can be either 0 (singlet exciton) or 1 (triplet exciton). The energy of the two states is not identical, the singlet exciton has a larger energy than a triplet exciton (the singlet-triplet energy difference is a key factor in TADF emitters, and is described in the next chapter). When an exciton recombines, energy is released in different forms: heat, creation of a defect state and photochemical changes of the excited material (classified as non-radiative recombination) or by the generation of a photon (radiative-recombination). Of course in the context of OLEDs, the goal is to minimize the first one and maximize the second one such that the efficiency of the device is maximized. The terms fluorescence and phosphorescence are used to refer to the radiative recombination of a singlet and triplet exciton, respectively. The generation of singlet and triplet excitons is not equal, and it is governed by spin-statistics. In the case of electrical excitation, only 25% of excitons are singlet, while 75% are triplets.

TADF are fluorescent materials with the peculiarity of being able to take advantage of the large triplet population. A key role is played by the energy difference between the singlet and triplet states, which will be discussed in Section 1.6.1.

Once an exciton is formed, it can move from molecule to molecule. Exciton transport is governed by two non-radiative mechanisms, Dexter and Forster energy transfer, shown in Figure 1.3. These two mechanisms describe the transfer of excited states from a donor molecule (D) to an acceptor molecule (A). The asterisk in Figure 1.3 indicates the excited molecule. Förster energy transfer is a mechanism in which no direct movement of charge is involved and the process is governed by the dipole-dipole interaction (Coulomb coupling). The Förster transfer rate can be quantified as:

$$k_F = k_0 \frac{9(\ln 10)\kappa^2 \phi_D}{128\pi^5 N_A n^4} \cdot J_s \cdot \frac{1}{R_{DA}^6} = k_0 \left[\frac{R_0}{R_{DA}}\right]^6 \tag{1.1}$$

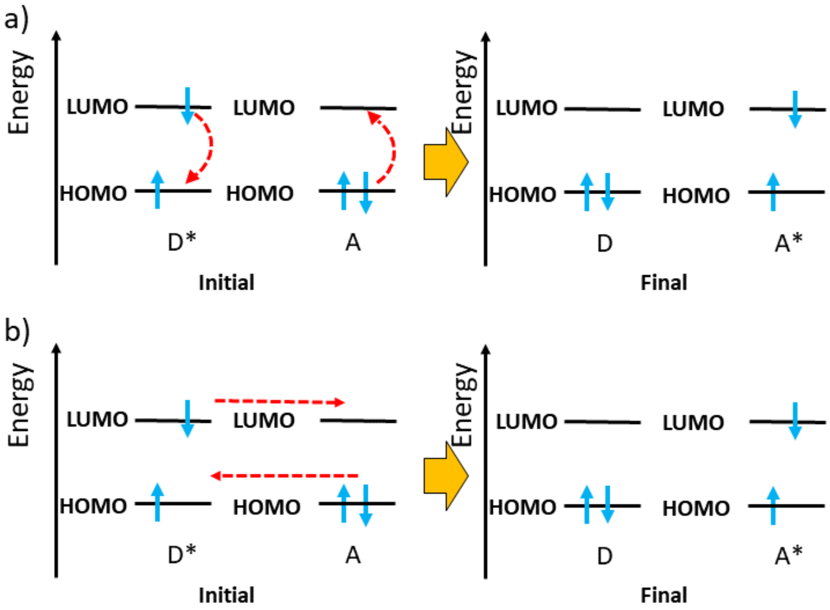

Figure 1.3: Schematics of Förster (a) and Dexter (b) energy transfer mechanisms.

where k_0 is the rate constant of the excited D without the presence of A, κ is the orientation factor, N_A is the Avogadro's number, ϕ_D is the luminescence quantum yield of D, n is the refractive index, R_{DA} is the distance between D and A and J_s is the spectral overlap between the emission of D and the absorption of A. The formula can be re-written by defining the Förster radius, R_0. Dexter transfer instead involves the actual transfer of electrons. This mechanism is governed by the exchange integral and it decays exponentially with the distance between D and A. The transfer rate can be indicated as:

$$k_D = \frac{2\pi}{\hbar} K^2 \cdot J_s \cdot e^{-2R_{DA}/L} \tag{1.2}$$

where K is a constant and L is the sum of the van der Waals radii. R_{DA} and J_s have already been defined above. It is noteworthy that both Förster and Dexter transfer rates are proportional to J_s, which is the spectral overlap between the donor emission spectra $I_D(\nu)$ and the acceptor absorption spectra $\alpha(\nu)$:

$$J_s = \int_0^\infty I_D(\nu)\alpha(\nu)d\nu \tag{1.3}$$

therefore a good overlap between the emission spectra of D and absorption spectra of A is required for both mechanisms.

In general, Dexter transfer is considered a short-range interaction ($\approx$ 1 nm), while Förster transfer is still efficient at longer range ($\approx$ 10 nm).[34] Another difference between the two transfer mechanisms is that Förster transfer is in general more efficient for singlet states, while Dexter transfer for triplet states. This result is a consequence of the different spin-wavefunctions contained in the Coulomb and exchange coupling, governing the Förster and Dexter transfer respectively. For additional details, the reader is referred to the literature.[35]

1.6 THERMALLY-ACTIVATED DELAYED FLUORESCENCE (TADF)

The peculiarity of these fluorescent emitters is that non-emissive triplet states are efficiently converted into singlet states, which can radiatively decay. The process of conversion from triplet to singlet states is called reverse-intersystem crossing (RISC). In this section I will dive in detail about the physics of TADF emitters and the main processes which influence the RISC process. Afterwards, an overview of the different molecular structures of TADF emitters is provided.

1.6.1 *Singlet-triplet energy levels and reverse intersystem-crossing process*

In Section 1.5 an introduction of excitons is given. The present section provides a more detailed discussion about the exciton energy and transition which occurs in TADF systems. A complete picture of the exciton energy and transitions in organic material is well described by the Jablonski diagram, see Figure 1.4. S_0 is the ground state, S_1, S_2, T_1 and T_2 are the first and second singlet and triplet excited states. For each of these states the vibrational states are indicated. In this scheme several transfer and relaxation processes are shown: fluorescence, intersystem-crossing (ISC), reverse intersystem-crossing (RISC), vibrational relaxation and internal conversion.

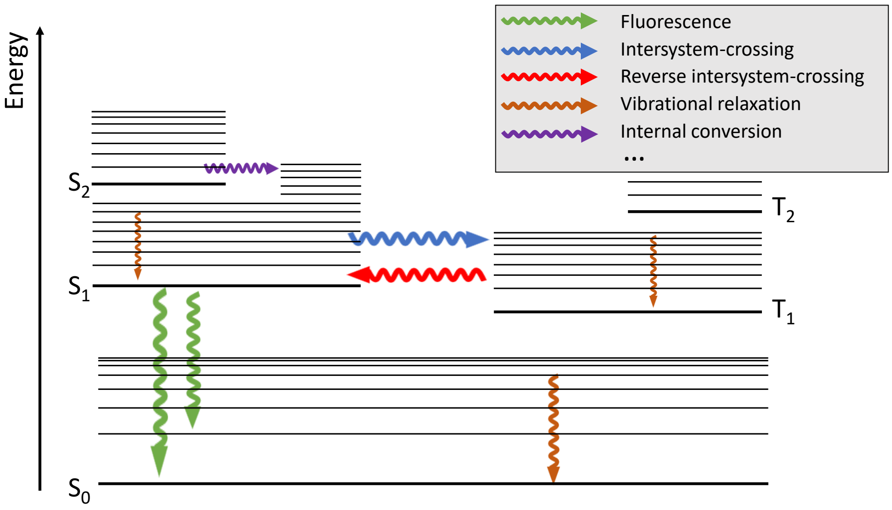

Figure 1.4: Example of a Jablonski diagram of a TADF system. The singlet states are indicated with S, while triplet states with T.

The RISC process is the key element in TADF compounds. This mechanism consist of a transition of an exciton from a triplet state to a singlet one. This process is energetically unfavourable, since the triplet state has a lower energy with respect to the singlet one. In TADF molecules the energetic difference between singlet and triplet is so small that solely the thermal energy at room temperature is sufficient to guarantee a strong RISC. It is clear that reducing the energy splitting between singlet and triplet states will favor the RISC mechanism.[10] Details about how to design TADF molecules in order to minimize the energy splitting will be discussed in the next section.

Besides the energetic aspect, during the RISC process the spin of the exciton must change from the singlet to the triplet state. With the use of heavy atoms such as iodine, bromine or transition metal atoms like Pt, Ir or Ru, the spin-flip process is enhanced by spin-orbit coupling (SOC).[36] In TADF materials instead, an efficient RISC process can be achieved without the use of heavy elements. The role of SOC in TADF materials is currently subject of intense research.[37] In several studies it has been suggested that the SOC between charge transfer triplet and singlet states is mediated by vibronically-coupled local excited triplet states. [38–40] In some molecules the hyperfine coupling is responsible for the spin-transition.[41] Going more in detail about this mechanism goes beyond the scope of this work.

In Figure 1.5, a simplified schematics of a TADF system is shown. S_1 and T_1 are the first excited singlet and triplet states while S_0 is the ground state (the y-axes represents the energy). k_f is the fluorescence decay rate, k_{nrs} and k_{nrt} are the non-radiative decay rate associated to the singlet and triplet states, k_{isc} is the inter-system crossing rate (transfer from the singlet to the triplet state) and k_{risc} is the reverse-intersystem crossing rate (transfer from the triplet to the singlet state). In this description phosphorescence is omitted, since I am dealing with fluorescent materials the radiative decay rate of the triplet state can be considered negligible.

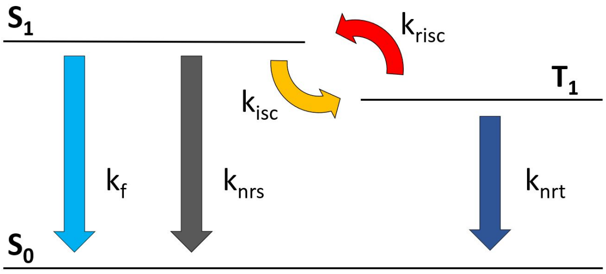

Figure 1.5: Simplified schematic illustration of a TADF system. S_0 is the singlet ground state, S_1 and T_1 are the singlet and triplet excited states. Five processes are considered: radiative and non-radiative decay of S_1 (k_f; k_{nrs}), intersystem-crossing (k_{isc}), reverse intersystem-crossing (k_{risc}) and non-radiative decay of T_1 (k_{nrt}).

Referring to Figure 1.5, I can now discuss the energy splitting between the singlet and triplet states. The singlet and triplet energy is well described by Cai *et al.*:[42]

$$E_s = E_0 + K + J \tag{1.4}$$

$$E_t = E_0 + K - J \tag{1.5}$$

$$\Delta E_{st} = E_s - E_t = 2J \tag{1.6}$$

$$J \approx \left(\frac{e^2}{r_1 - r_2} \right) \langle \varphi_H(1)\varphi_L(2) | \varphi_H(2)\varphi_L(1) \rangle \tag{1.7}$$

where E_s, E_t, E_0 represent the singlet energy, triplet energy and the one-electron orbital energy without electron-electron interaction. K is the classic Coulombic repulsion energy and $r_1 - r_2$ is the distance between the two charges. J is the exchange energy and, assuming the same half-filled orbital configuration of S_1 and T_1, the matrix element for J can be expressed as Equation 1.7. (1) and (2) represents the two charges occupying the frontier molecular orbital. φ_H and φ_L are HOMO and LUMO wavefunctions.

From this formulation it is clear that ΔE_{st} is proportional to the overlap integral between the HOMO and LUMO wavefunctions, and inversely proportional to the distance between the two charges.[43] Therefore, one way to reduce the overlap integral is to design molecules with spatially separated HOMO/LUMO. In this case the so called donor-acceptor (D-A) units, located far away from each other in the molecule, enables the creation of charge-transfer states (CT) [44]. Another rule which can reduce ΔE_{st} is to have the D and A units orthogonal to each other.[45, 46] However, it must be noted that the fluorescence decay rate ($\mathrm{k_f}$) depends quadratically on the product $\varphi_H(2)\varphi_L(1)$.[43] Therefore, an excessive reduction of the wavefunction overlap is not beneficial to the overall emission, since $\mathrm{k_f}$ would also be reduced.

1.6.2 *Typical donor-acceptor systems*

One of the most common structures of pure organic TADF molecules is the donor-acceptor architecture with usually multiple D-A units. Having spatially separated D-A units allows for a small ΔE_{st}. However, to ensure an integral molecular system, required for fluorescent emission, an appropriate choice of connecting bridge between D-A is necessary. [43] Commonly used donor units are carbazole[47–49], phenoxazine[50, 51], diphenylamine[52, 53], and derivatives. Typical acceptor units are: cyano[54, 55], diphenyl sulfoxide[47] and nitrogen -based systems[10, 56, 57].

In Chapter 3 and Chapter 4 I have studied films and devices where the emissive TADF molecule is DMAC-TRZ. In Figure 1.6a the structure of the molecule is shown, and is composed of 9,9-dimethyl-

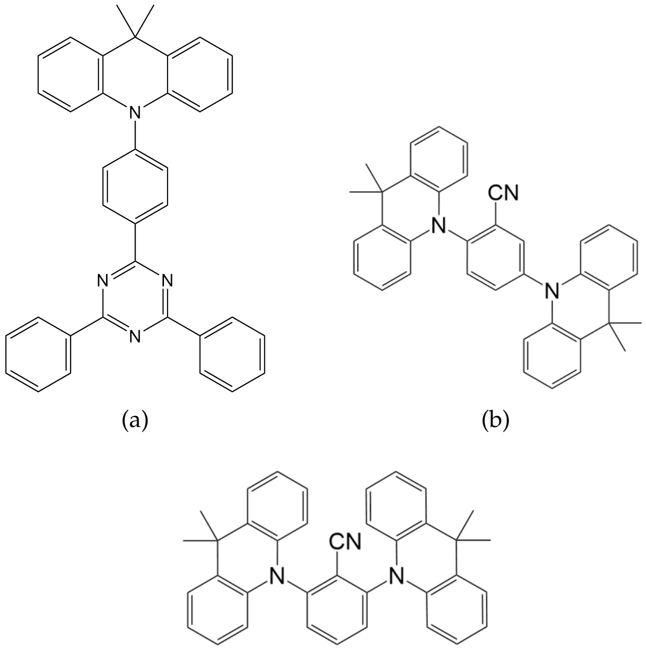

(a)

(b)

(c)

Figure 1.6: Molecular structure of DMAC-TRZ (a), 25ACA (b) and 26ACA (c).

9,10-dihydroacridine (DMAC) as donor unit, and 2,4,6-triphenyl-1,3,5-triazine (TRZ) as acceptor unit with a dihedral angle between the two of about 90°.[58] DMAC-TRZ was firstly reported by Tsai *et al.*[59] and has been widely investigated in recent years. Different values of ΔE_{st} have been reported, depending on the specific host in which the molecule was embedded. In a study of Stavrou *et al.* [46] a detailed photophysical analysis of this molecule is conducted. In their work ΔE_{st} spans from 170 meV (in Zeonex, solution processed), to even negative values of -42 meV (in DPEPO and neat film) and -20 meV (in Toluene, solution processed); in mCBPCN, the host used in Chapter 4, a value of 24 meV is reported. In Chapter 3 instead, I studied TADF films, not yet incorporated into devices. For this study two emissive molecules have been investigated: 25ACA (2,5-bis(9,9-dimethyl-9,10-dihydroacridin-10-yl)benzonitrile) and 26ACA (2,6-bis(9,9-dimethyl-9,10-dihydroacridin-10-yl)benzonitrile). These two molecules have been firstly reported by Gudeika *et al.* [60] and subsequently investigated by Danos *et al.* [61]. The structure of the two molecules is indicated in Figure 1.6b and Figure 1.6c.

1.6.3 *Multiresonance TADF and hyperfluorescence*

An alternative design principle has been introduced by Hatakeyama *et al.*[62] in 2015, later indicated as multiresonance TADF (MR-TADF).

This TADF design method has not been investigated in this thesis, however, a short description is given for completeness.

Differently from the classic D-A design, where the two units are located at different sides of the molecule, MR-TADF is characterized by having electron-donating (donor) atoms and electron-deficient (acceptor) atoms. The donor and acceptor atoms are located throughout the entire molecule disposed *para* to each other.[63] The fact that the HOMO and LUMO orbitals are shifted by one atom provides a relatively small exchange integral which ensures a small ΔE_{st}. In contrast to common D-A structure, this design allows for a narrow emission spectra, thanks to the rigidity of the molecule.[64]

An interesting study employing these materials has been conducted by Hatakeyama *et al.* in 2016 [65], in which two DABNA structures were reported. These two molecules exhibit a deep blue emission (459 and 467 nm) with a full width at half maximum (FWHM) of 28 nm and CIE coordinates of (0.13, 0.09) and (0.12, 0.13) respectively. CIE is the color space defined in 1931 by the *Commission Internationale de l'éclairage* and quantitatively links the wavelength of an electromagnetic wave in the visible spectrum and the color perceived by human eye.[66]

In Figure 1.7 the molecular structure of ν-DABNA is shown.[67, 68]

Thanks to the narrow and deep blue emission of this type of molecules, they have been used in the so called hyperfluorescence concept, firstly proposed by the group of professor Adachi.[11] In this case, the emissive layer is composed of the host, a pure TADF molecule and a MR-TADF molecule. The basic working principle of these EMLs is that the conversion of triplets into singlets takes place on the pure-TADF molecules. Subsequently the singlet excitons are transferred to the MR molecule by Förster energy transfer, where they radiatively decay to the ground state. In this way the narrow and deep blue emission of MR molecule can be coupled with a strong triplet harvesting of the pure TADF material.[69, 70]

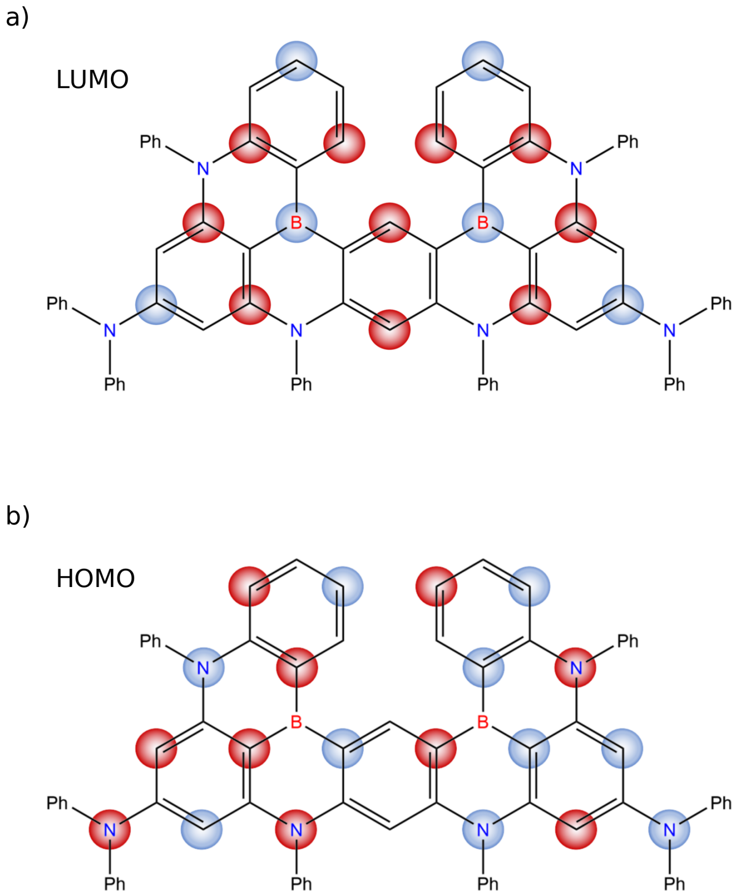

Figure 1.7: Molecular structure and HOMO(b)/LUMO(a) diagrams of *ν*-DABNA. Adapted from [67].

2

METHODS

2.1 ELECTRO-OPTICAL CHARACTERIZATION

The OLEDs presented in this thesis have been electro-optically characterized with the all-in-one experimental setup *Paios*, shown in Figure 2.1, from Fluxim AG.[71].

Figure 2.1: *Paios* measurement instrument.

Paios is an instrument used to characterize both OLEDs and solar cells. Depending on which device is measured the setup slightly changes, but the main structure is identical and it is composed by two main units:

- Function Generator Unit, which is used to apply voltage to the sample
- Digitizer Unit, which is used to measure the actual current flowing through the OLED and the voltage signal from the photodetector (in case of solar cells this component is replaced with an LED)

Paios is controlled with the software interface called *Characterization Suite*. With *Characterization Suite* the user can:

- Define the experimental protocol containing the list of experiments to be performed
- Perform post-processing analysis on the experimental results (i.g. calculating RC effect from impedance data, mobility from CELIV data, ...)

- Plot, store and export experimental results
- Compare experimental data with simulations performed with *Setfos* through the so called *Setfos-Paios integration* (SPI)

In the following sections, the experimental techniques used in this thesis are briefly described.

2.1.1 *Current-Voltage-Luminance (JVL)*

The current-voltage-luminance is the basic steady state experimental technique to characterize an OLED. A voltage scan is applied to the device and current and luminance are recorded. With *Paios* this experiment can be performed with three methods: ramped, sequential, and pulsed. In this work only the pulsed method is used, in which each voltage point is measured individually with a voltage pulse. This method allows to avoid heating of the device during the measurement and to improve the current resolution (down to 10 pA) thanks to averaging the current during the voltage pulse. At each voltage pulse the emission of the OLED is measured with the photodetector. The emitted light can be expressed as Luminance (cd/m²) only when a reference measurement with a calibrated spectrometer is performed.

In Figure 2.2 an example of a voltage-current and a voltage-luminance curves measured with *Paios* is shown.

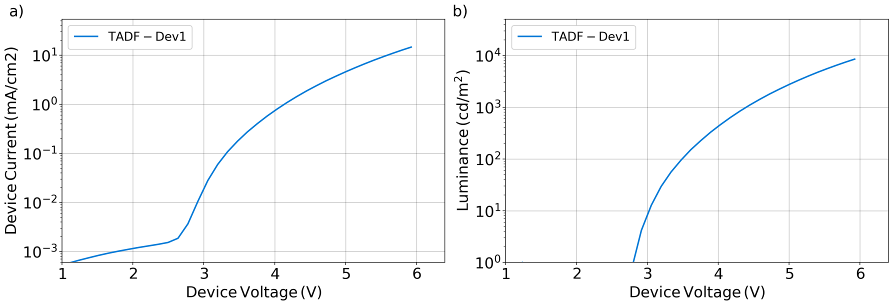

Figure 2.2: Example of pulsed JVL technique performed on a TADF device. The pulse duration is 100 ms. (a) current density vs voltage; (b) luminance vs voltage.

2.1.2 *Carrier extraction by linearly increasing voltage (CELIV)*

This technique was introduced by Juska *et al.*[72] and is a transient experiment in which the applied voltage varies linearly over time and the current is measured. In this thesis injection-CELIV is exploited, in which a constant voltage (V_{offset}) is applied to the OLED prior to the voltage ramp. During the initial offset, charges are injected into the device and subsequently extracted by the voltage ramp. The measured current consists of a plateau, given by the displacement current, with possibly one or more peaks on top, given by the re-extracted charges. Injection-CELIV is mostly used with OLEDs, and it allows to estimate charge carrier mobilities and charge carrier density. CELIV is also widely used to investigate solar cells, in this case the charge are created by exciting the sample with a light pulse (photo-CELIV).

In Figure 2.3 an example of the injection-CELIV experimental result is shown.

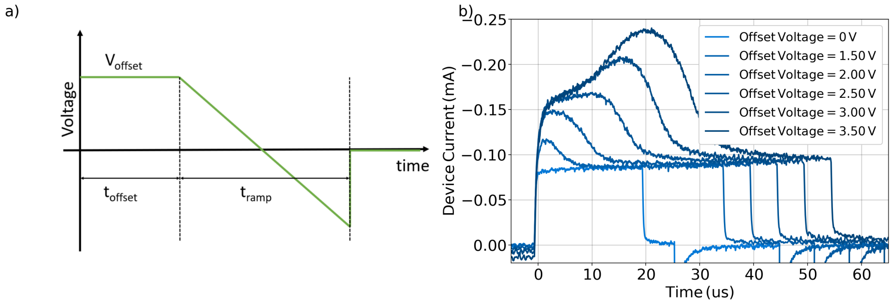

Figure 2.3: Example of injection-CELIV technique performed on a TADF device. (a) Schematics of the applied transient voltage; (b) Device current with different V_{offset} applied.

2.1.3 *Impedance spectroscopy*

Impedance spectroscopy is a common characterization technique used to investigate OLED and solar cells. The OLED (or solar cell) is, for all-intents, an electrical component with a specific transfer function. A sinusoidal voltage is applied to the device and the current is recorded, the real and imaginary part of the transfer function can be reconstructed and important information extracted. Following the analysis described by Novy *et al.* [73], we can define the steps necessary to calculate the impedance, starting from the applied sinusoidal voltage:

$$V(t) = V_{\mathrm{DC}} + V_{\mathrm{AC}} = V_{\mathrm{offset}} + V_{\mathrm{amp}} \sin(\omega t) \tag{2.1}$$

where V_{DC} is the constant voltage offset, V_{amp} is the sinusoidal voltage amplitude and ω is the angular frequency ($\omega = 2\pi f$). One requirement is that V_{amp} should be small enough, so that the system can be considered linear. The recorded current is also sinusoidal:

$$I(t) = I_{\mathrm{DC}} + I_{\mathrm{AC}} = I_{\mathrm{offset}} + I_{\mathrm{amp}} \sin(\omega t + \phi) \tag{2.2}$$

where ϕ is the phase shift introduced by the OLED. By measuring the current, the complex impedance can be simply computed with the formula:

$$\overline{Z}(f) = \frac{\overline{V}}{\overline{I}} = Z_{\mathrm{real}} + i \cdot Z_{\mathrm{imaginary}} \tag{2.3}$$

where $\overline{V}$ and $\overline{I}$ are the voltage and current, indicated with the complex notation. The capacitance (C) and conductance (G) can be calculated:

$$C = \frac{1}{2\pi f} \cdot \frac{-Z_{\text{imaginary}}}{|\overline{Z}|} \qquad G = \frac{Z_{\text{real}}}{|\overline{Z}|} \tag{2.4}$$

In this thesis I mainly focus on the imaginary part of the impedance which contains the capacitance. This experiment can be performed at different V_{offset}, and we refer to it as C-V, or at different frequencies, and we call it C-f.

Alternatively, a frequently used representation of the impedance is the Cole-Cole plot, where the real part of the impedance is plotted on the x-axis and the imaginary on the y-axis.

A capacitance-voltage example is shown in Figure 2.4a. At low/negative voltage the device is completely empty of charges and the measured capacitance is the geometrical one of the entire OLED (C_{geo}). When V_{offset} is increased, charges are injected to the device causing the capacitance to increase.[74] When both charge types - electrons and holes - are injected, they can recombine in the emissive layer and emit photons. In this condition the OLED is a conductive element and therefore the capacitance drops. The voltage at which the capacitance peaks is considered to be a good estimation of the built-in voltage of the OLED (V_{bi}).[73]

A capacitance-frequency example is shown in Figure 2.4b. At high frequency, the capacitance plateau again represents the total C_{geo} of the OLED (10^6 Hz in Figure 2.4b). At larger frequencies, we see a sudden decrease of the capacitance caused by the *RC* effect. At lower frequencies, the C-f plot might show plateaus (as the one located at 10^4 Hz in Figure 2.4b), indicating an injection and accumulation of charges inside the OLED.

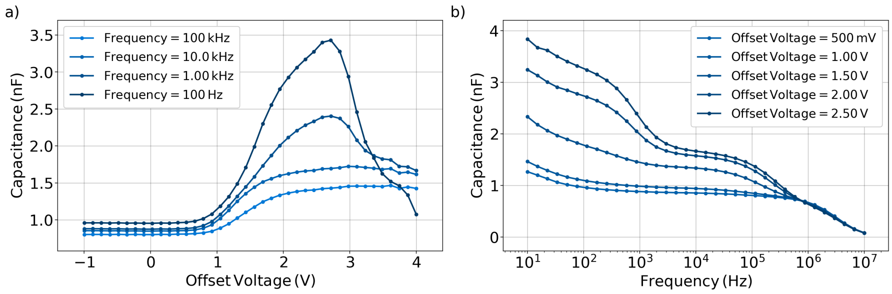

Figure 2.4: Example of impedance spectroscopy technique performed on a TADF device. (a) C-V performed at four frequencies (100 kHz, 10 kHz, 1 kHz, 0.1 kHz); (b) C-f performed at different V_{offset} (0.5 V, 1 V, 1.5 V, 2 V, 2.5 V).

Another impedance measurement performed in this thesis is the transient capacitance. In this case, the device is first preconditioned at a specific voltage (V_{prec}) and afterwards the capacitance is measured (at a fixed applied voltage (V_{meas}) and frequency) with a different time delay with respect to the preconditioning. A schematics of the applied voltage and an example are provided in Figure 2.5.

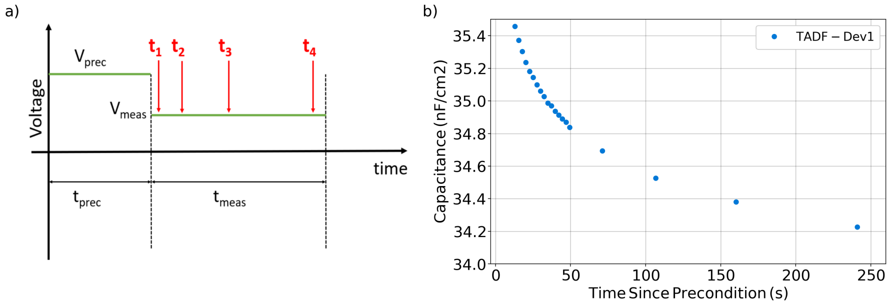

Figure 2.5: Example of transient impedance technique performed on a TADF device. (a)Schematics of the applied voltage; (b) Transient capacitance performed with $V_{meas} = 1.5\,V$ and frequency $= 100\,Hz$.

To summarize, impedance spectroscopy is a vastly used characterization technique which can provide important information about charge transport [75] and energy barriers[76, 77]. In unipolar devices (electron only or hole only devices) impedance spectroscopy is used to quantify the polarity of specific materials[78] or to determine the dielectric characteristics.[79]

2.1.4 *Transient electroluminescence (TEL)*

Transient electroluminescence, as the name suggests, is a transient experiment in which a voltage pulse is applied to the OLED and current and luminance are recorded. This technique is widely used to investigate charge carrier mobilities and excitonic parameters.[80, 81]

An important aspect to mention when describing this experimental technique is the *RC* effect, which influences the current decay (rise). In fact, the contact between the contact probe and the electrodes of the sample possess a certain resistance while the device itself possess a geometric capacintance, the series of the two acts as a low pass filter and can be represented as an *RC* circuit. The consequence is that the speed of the applied electrical pulse is limited by the *RC* constant $\tau = RC$. The *RC* effect can be lowered in two ways: decreasing *R* (i. e. by evaporanting a thin layer of low resistance metal on top of the contacts) or decreasing *C* of the pixels (by decreasing the area).

Particularly interesting is the emission of the OLED during turn-on and turn-off. In several studies a delayed emission occurring in the first microseconds has been observed and explained with trapping-detrapping processes or by assuming a split emission zone at the two sides of the EML.[82–84] In TADF devices, the luminance decay is of particular interest since might contain important information regarding the delayed component, which is given by the conversion of triplet states into singlet ones. [85]

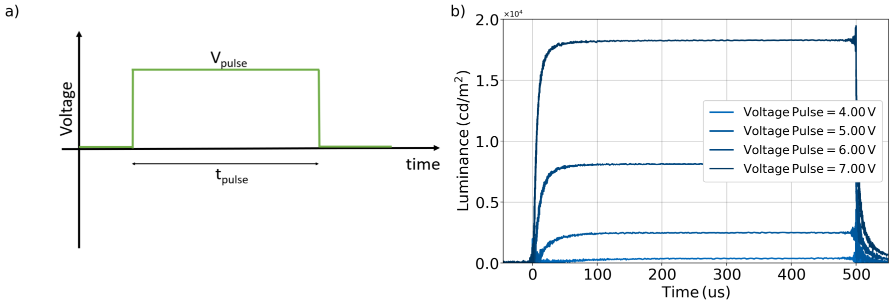

Figure 2.6: Example of TEL technique performed on a TADF device. (a) Schematics of the applied transient voltage; (b) Luminance with different V_{pulse} applied.

2.2 PLATFORM FOR DEGRADATION ANALYSIS

In the introduction I have already described the importance of studying and understanding the degradation processes in blue TADF OLEDs. The platform *Litos* is used for this purpose.

As visible from Figure 2.7, *Litos* is equipped with four chambers in which temperature and atmosphere can be independently controlled. Moreover, in each chamber four pixels can be electrically stressed with a specific current density. With this setup, a total of sixteen pixels can be stressed in parallel. During stressing, two quantities are measured for each pixel: the applied voltage and the emission. Each chamber is equipped with four photodiodes, with which the emission of the pixels is measured.

The user can control *Litos* with the same interface used to control *Paios*, *Characterization Suite*.

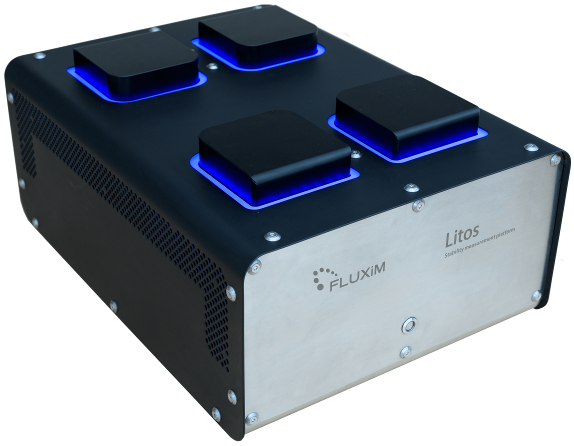

Figure 2.7: *Litos* measurement instrument.

2.2.1 *Litos-Paios integration*

Litos and *Paios* can be used in combination. With this setup a detailed electro-optical characterization can be performed automatically during degradation. In Figure 2.8 a picture of the two systems used in combination is shown.

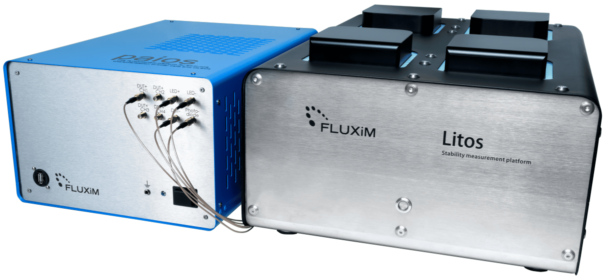

Figure 2.8: *Litos-Paios* combination.

From literature, several experimental techniques are used to investigate and quantify the degradation mechanisms affecting OLEDs. In the study conducted by G. W. Lee *et al.*[86], the degradation of fluorescent blue OLED is explored observing the change in JV measurements. More sophisticated technique such as TEL can provide additional indication about the nature of the degradation mechanisms. For instance, Q. Niu *et al.*[87] analyzed the change of the delay time (delay between the application of the voltage pulse and the appearance of electroluminescence) during degradation on phosphorescent OLED. With this analysis they were able to indicate that electron transport is the main cause of degradation and that is mainly caused by creation of electron trap states in the emissive layer. Another technique frequently used to investigate the degradation of OLED is impedance spectroscopy.[73, 88] A combination of several techniques allows an even better understanding of the underlying mechanisms. The study conducted by T. D. Schmidt *et al.*[89] on a phosphorescent OLED shows that the degradation in this case is mainly caused by a decrease of the charge carrier balance and a reduced radiative quantum efficiency, both induced by the formation of trap states in the EML. Several other studies showed the importance of having such an in-depth approach.[90–92]

To conclude, in order to perform a thorough investigation of the degradation mechanisms in OLEDs, the simple luminance decay over time or steady-state analysis is not sufficient to draw meaningful conclusions. A more systematic strategy comprising a wider spectra of experimental techniques is therefore required.

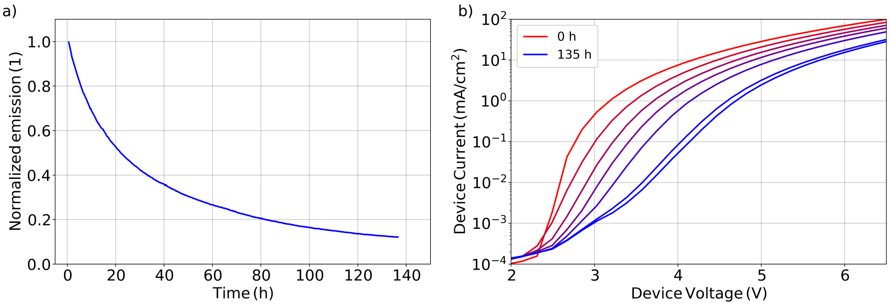

Figure 2.9: Example of the experimental results from *Litos-Paios* integration. The stress with *Litos* is performed with 20 mA/cm² at 283 K on TADF OLEDs. (a) emission decay over time measured with *Litos*. (b) JV curve at different stressing times (0, 16, 34, 51, 72, 119 and 135 hours).

2.3 SIMULATIONS

The modeling software used is this thesis is *Setfos* version 5.2.[93] *Setfos* comprises four modules (*Advanced optics*, *Absorption*, *Drift-diffusion* and *Emission*), which can be activated for the specific use. In this work, since I am investigating OLEDs, the *Drift-diffusion* and *Emission* modules are used. In Figure 2.10 a schematic of the coupling between the *Drift-diffusion*, excitonic model and *Emission* is shown.

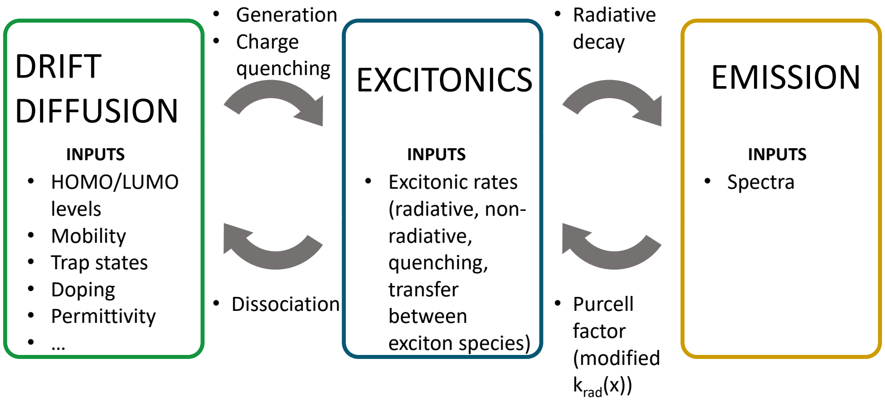

Figure 2.10: Schematics of the coupling between the *Drift-diffusion*, excitonics and *Emission* in *Setfos*.

2.3.1 *Electrical model*

The drift-diffusion formalism is widely used to model electric transport in organic materials.[94–96] With *Setfos*, the charge motion in the semiconducting media is described by a set of equations, defined in one dimension (x). This approach is justified by the fact that the lateral dimension are 10^5 larger than the total thickness of the device. The following mathematical derivation is adapted from the *Setfos'* manual.[97]

Setfos allows for the definition of disordered systems, in which the energy levels (HOMO-LUMO) of each layer are defined with a distribution (*Extended Gaussian disordered model* (EGDM) or *Extended Correlated disordered model* (ECDM)). However, with *Setfos* impedance simulations of multi-layer structures, defined with EGDM or ECDM, can not be performed. Therefore, in this thesis this possibility is not exploited and for each material a discrete energy is defined.

The first step of a drift-diffusion model is the current continuity equation:

$$\frac{\partial n_e}{\partial t}(x,t) = \frac{1}{e} \cdot \frac{\partial j_e}{\partial x}(x,t) - R_{t-e}(x,t) - R(x,t) \tag{2.5}$$

$$\frac{\partial n_h}{\partial t}(x,t) = -\frac{1}{e} \cdot \frac{\partial j_h}{\partial x}(x,t) - R_{t-h}(x,t) - R(x,t) \tag{2.6}$$

where n_e and n_h indicate the density of electrons and holes, j_e and j_h are the current density of electrons and holes and e is the elementary charge. The recombination terms are indicated as R (bimolecular recombination) and $R_\text{t-e}$-$R_\text{t-h}$ (recombination caused by traps, also known as Shockley-Read-Hall recombination (SRH)). When an external light source is considered in the model, an additional term to represent the photon absorption is included - $G_\mathrm{opt} \cdot g(x)$ - where the first term indicate the optical generation efficiency and the second the generation profile. The recombination process is described by the Langevin model [98] since organic semiconductors are materials with relatively low mobility of charges:

$$R = \eta \frac{e}{\epsilon_0 \epsilon_\mathrm{r}} (\mu_\mathrm{e} + \mu_\mathrm{h})(n_e n_h - n_\mathrm{i}^2) \tag{2.7}$$

Where μ_e and μ_h are the electron and hole mobilities, n_i is the intrinsic charge concentration at thermal equilibrium and η is a phenomenological parameter defined as Langevin recombination efficiency. The mobility of electrons and holes can be defined as constant, field-dependent or field-temperature-dependent. In this thesis only the first two models are used, and its choice depends on the specific material.

The electron and hole currents are defined as:

$$j_e(x,t) = -e \cdot n_\mathrm{e}(x,t) \cdot \vec{v}_\mathrm{e}(x,t) + e \cdot D_\mathrm{e} \cdot \frac{\partial n_e}{\partial x}(x,t) \tag{2.8}$$

$$j_h(x,t) = +e \cdot n_\mathrm{h}(x,t) \cdot \vec{v}_\mathrm{h}(x,t) - e \cdot D_\mathrm{h} \cdot \frac{\partial n_h}{\partial x}(x,t) \tag{2.9}$$

The first terms of the two equations are the drift components and the velocity can be expressed as:

$$\vec{v}_{\mathrm{e}}(x,t) = -\mu_{\mathrm{e}} \cdot \vec{E}(x,t) \tag{2.10}$$

$$\vec{v}_{\mathrm{h}}(x,t) = +\mu_{\mathrm{h}} \cdot \vec{E}(x,t) \tag{2.11}$$

while the second terms are the diffusion components and they can be defined with the classical Einstein relation (when no disorder is taken into account):

$$D_{\mathrm{e}} = \mu_{\mathrm{e}} \cdot \frac{kT}{e} \tag{2.12}$$

$$D_{\mathrm{h}} = \mu_{\mathrm{h}} \cdot \frac{kT}{e} \tag{2.13}$$

By inserting the drift and diffusive terms in Equation 2.8 and Equation 2.9 the current equations can be re-written as:

$$j_e\,(x,t) = n_e\,(x,t) \cdot e \cdot \mu_e \cdot E\,(x,t) + \mu_e \cdot k_B \cdot T \cdot \frac{\partial n_e}{\partial x}(x,t) \tag{2.14}$$

$$j_h\,(x,t) = n_h\,(x,t) \cdot e \cdot \mu_h \cdot E\,(x,t) - \mu_h \cdot k_B \cdot T \cdot \frac{\partial n_h}{\partial x}(x,t) \tag{2.15}$$

The charge densities are coupled with the electric field through the Poisson equation:

$$\frac{\partial E}{\partial x}(x,t) = -\frac{e}{\epsilon_0 \epsilon_r} \cdot [n_h(x,t) - n_e(x,t) - n_{n-doping} + n_{p-doping} + n_{t-h}t(x,t) - n_{t-e}(x,t)] \tag{2.16}$$

where $n_{n-doping}$ and $n_{p-doping}$ are the acceptor and donor doping densities and $n_{\text{t-e}}(x,t)$ and $n_{\text{t-h}}(x,t)$ are the electron and hole trap densities. In *Setfos* a trap state is modeled with three parameters: trap density, energetic trap depth and the charge capture rate. When SRH or trap-trap recombination are activated an additional parameter must be indicated (SRH: capture rate of the opposite charge carrier; trap-trap: trap-trap recombination rate).

The following equation provides the boundary conditions for the previous equations:

$$V_{dev}(t) = \frac{1}{e} \int_0^d E(x,t)\,dx + V_{bi} \tag{2.17}$$

The reader can refer to [99] or [100] for further details about this derivation.

2.3.2 *Modeling of TADF emitters*

In TADF materials, the concept of exciton plays a fundamental role. In *Setfos* as many exciton species as necessary can be defined and they are modeled with the excitonic equation described in this section. For a TADF system one needs at least two excitons, a singlet and a triplet. In the model used in this thesis the exciton generation is coupled with the recombination profile (calculated by the *Drift-diffusion* module) and the emission (calculated by the *Emission* module) is in turn coupled with the exciton profile.

The excitonic equation solved by *Setfos* is:

$$
\begin{aligned}
\frac{\partial S_\mathrm{i}}{\partial t}(x) =& g_\mathrm{i} R(x) + \vec{\nabla} \cdot \vec{J}_{\mathrm{S,i}}(x) - (k_{\mathrm{rad,i}}(x) + k_{\mathrm{non\text{-}rad,i}}) \cdot S_\mathrm{i}(x) + \\
& - k_{\mathrm{annih,i}} \cdot S_\mathrm{i}(x)^2 + \sum_{j=1}^{n_\mathrm{exc}} (tts_\mathrm{ji} \cdot k_{\mathrm{annih,j}} \cdot S_\mathrm{j}(x)^2) + \\
& - \sum_{j=1}^{n_\mathrm{exc}} k_{\mathrm{annih,ij}} \cdot S_\mathrm{i}(x) S_\mathrm{j}(x) + \sum_{j=1}^{n_\mathrm{exc}} \sum_{l=1}^{n_\mathrm{exc}} \frac{1}{2} stt_\mathrm{jli} k_{\mathrm{annih,jl}} S_\mathrm{j}(x) S_\mathrm{l}(x) + \\
& - k_{\mathrm{p\text{-}h,i}} S_\mathrm{i}(x) n_h(x) - k_{\mathrm{p\text{-}e,i}} S_\mathrm{i}(x) n_e(x) + \\
& + \sum_{j=1}^{n_\mathrm{exc}} (k_\mathrm{ji} \cdot S_\mathrm{j}(x) - k_\mathrm{ij} \cdot S_\mathrm{i}(x)) + \\
& + \sum_{j=1}^{n_\mathrm{exc}} \left(k_\mathrm{ij} \cdot exp\left(\frac{-\Delta E_\mathrm{ji}}{k_\mathrm{b} T} \right) \cdot S_\mathrm{j}(x) - k_\mathrm{ji} \cdot exp\left(\frac{-\Delta E_\mathrm{ij}}{k_\mathrm{b} T} \right) \cdot S_\mathrm{i}(x) \right)
\end{aligned}
\tag{2.18}
$$

a line-by-line explanation of the terms follows:

- first line: $R(x)$ is the recombination term from Equation 2.5 and Equation 2.6 and g_i is the generation efficiency. I. e. in a classical view of singlet and a triplet states, the generation efficiency is 0.25 for the singlet exciton and 0.75 for the triplet. The second term is the diffusion term. The third term indicates the loss of excitons through radiative or non-radiative decay processes.

- second line: $k_{annih,i}$ is the annihilation rate from the same exciton specie (i. e. singlet-singlet annihilation or triplet-triplet annihilation), this process might lead to the creation of another exciton with a specific prefactor (tts_ji), indicated in the second term of the line.[35]

- third line: $k_{annih,ij}$ is the annihilation rate from different species of excitons (i. e. singlet-triplet annihilation). The second term contains the generation of excitons from this annihilation process, in this case the prefactor is tts_jli.[35]

- fourth line: $k_{\mathrm{p\text{-}h,i}}$ is the exciton-polaron quenching with holes and $k_{\mathrm{p\text{-}e,i}}$ is the exciton-polaron quenching with electrons.

- fifth line: transfer from and to other exciton species is also possible (k_{ji} and k_{ij}), for example the intersystem crossing (ISC) of a TADF system.
- sixth line: thermally activated exciton transfer from and to other exciton species are indicated in this line. The reverse-intersystem crossing (RISC) of TADF materials is the perfect example of such a process. In *Setfos* when this term is activated the prefactor k_{ji} is automatically taken from the fifth line (ISC rate). However in this thesis the reverse-intersystem crossing process is modeled by simply defining an additional rate in the fifth line.

2.3.3 *Optical model*

The calculation of the passive optical properties are based on the transfer matrix approach in *Setfos*.[97] With this model, the reflection ($R(\lambda)$), absorption ($A(\lambda)$) and transmission ($T(\lambda)$) of the light are calculated by imposing $R(\lambda) + A(\lambda) + T(\lambda) = 1$. This model describes the plane wave propagation and is based on the fact that the electric field across different media is governed by continuity equations. With this method each layer is represented as a matrix containing the thickness and the refractive index. The system matrix, representing the entire stack, can be simply calculated as a multiplication of the single-layer matrices.

The emission module of *Setfos* is based on the dipole model, where the emission of a single molecule can be approximated as that from an Hertzian dipole. However, an OLED is a thin multilayer structure with two electrodes at the extremities (typically one highly reflective). In this conditions, the molecule is embedded in an optical cavity, where the reflected electric field has a strong influence on the dipole emission. This mechanism is termed Purcell effect, and it can be taken into account with the so called Purcell factor. In this way the emission rate of the molecule becomes dependent on its position inside the optical cavity. The non-radiative component of the dipole instead is not influenced by the Purcell factor, and remains constant.[101] Once the effective position-dependent radiative decay rate of the emissive exciton species is calculated, the light emission is computed. In the remaining part of the chapter the mathematical derivation of these quantities is provided.

Approximating the molecule as an Hertzian dipole, the dynamics of its oscillation can be described with:

$$\frac{d^2}{dt^2}\vec{p} + b_0\frac{d}{dt}\vec{p} + \omega^2\vec{p} = \frac{e^2}{m}\vec{E}_R(\omega) \tag{2.19}$$

where b_0 is the intrinsic power of the dipole, ω is the oscillator frequency of the dipole in the undamped case, e is the elementary charge, m is the effective mass of the dipole and $\vec{E_R}$ is the interface-reflected field at the dipole position. In an infinite birefringent medium, with an ordinary and extraordinary refractive index n_{or} and n_{ex}, the radiative power of an horizontal and perpendicular dipole can be expressed by:

$$q_0 b_{0\perp} = \frac{|p|^2 \omega k_0^3}{12\pi\epsilon_0} n_{or} \tag{2.20}$$

$$q_0 b_{0||} = \frac{|p|^2 \omega k_0^3}{12\pi\epsilon_0} n_{or} \left(\frac{3n_{or}^2 + n_{ex}^2}{4n_{or}^2} \right) \tag{2.21}$$

In both cases the intrinsic power of the dipole is:

$$b_0 = b_0 q_0 + (1 - q_0) b_0 \tag{2.22}$$

where the first component is the radiative fraction, and the second the non-radiative. The fact that the dipole is immerse in an optical cavity requires to include an additional term to take into account the effect of the reflected electric field, and the equation can be rewritten:

$$b = b_0 q_0 F + (1 - q_0) b_0 \tag{2.23}$$

where F is the Purcell factor and is multiplied to the solely radiative term, this because the non-radiative is not impacted by the cavity effect. F can be expressed by a parametrization of the in-plane wave-vector as:

$$F = \int_0^\infty f(u)\, du \tag{2.24}$$

where $u = \frac{k_{||}}{k_0 n_{or}}$ for ordinary waves and $u = \frac{k_{||}}{k_0 n_{ex}}$ for extraordinary waves. $k_{||}$ is the in-plane wave vector and k_0 is the wave-vector in vacuum. The function $f(u) = f_x(u, \lambda)$ is the infinitesimal dipole radiation (at a given angle, dipole position and wavelength).

Finally, the total lifetime can be calculated from the intrinsic lifetime, τ_0:

$$\frac{\tau_0}{\tau} = \frac{b}{b_0} = 1 - q_0 + q_0 F \tag{2.25}$$

and the reflection-modified apparent quantum efficiency, q, is:

$$q = \frac{q_0 F}{q_0 F + 1 - q_0} \tag{2.26}$$

When excitons are included in the model, instead of τ_0 and q_0 the user must input the radiative and non-radiative decay rates for each exciton species, k_{r0} and k_{nr0}. As said before, the radiative component is modified by the Purcell factor and becomes position dependent, $k_r(x)$, while the non-radiative is not. The excitonic formalism is univocally related to the τ-q one by:

$$\frac{1}{\tau} = k_r + k_{nr} \tag{2.27}$$

$$q = \frac{k_r}{k_r + k_{nr}} \tag{2.28}$$

3

DETERMINING NON-RADIATIVE DECAY RATES IN TADF COMPOUNDS USING COUPLED TRANSIENT AND STEADY STATE OPTICAL DATA.

As a first study, I investigated the fundamental properties of TADF emitters and their potential impact on the efficiency of the final device. More specifically, I studied how the non-radiative decay rates of singlet and triplet states could influence the efficiency of the OLED.

Additionally, a global fitting algorithm has been defined. With this approach, by taking into account steady-state and transient photoluminescence measurements, performed on TADF films, I was able to determine the entire set of decay rates: fluorescence, intersystem-crossing, reverse intersystem-crossing and non-radiative decay rates of singlet and triplet states.

This chapter reports the peer-reviewed article "Determining non-radiative decay rates in TADF compounds using coupled transient and steady state optical data"[102]. The co-authors supported with the following contributions: Dr. Sandra Jenatsch and Prof. Beat Ruhstaller contributed with scientific discussions and with support in the scientific development of the article; Kleitos Stavrou and Dr. Andrew Danos and Prof. Andrew P. Monkman provided the experimental optical data. All the co-authors contributed with proof-reading of the publication.

3.1 INTRODUCTION

In recent years, the TADF mechanism has been deeply investigated and the underlying processes elucidated. The transition from triplet to singlet state, which governs the TADF process, has been found to occur in a complex manner where multiple excited states are involved (charge-transfer and local-excited states) and additional phenomena play a crucial role (spin-orbit and vibronic-coupling).[103, 104] Despite the complexity of the TADF process, the emissive properties of new materials are frequently characterized using a simpler model where only three states are considered: the ground state (S_0), the first excited singlet (S_1) and triplet states (T_1).[105] The three-state model was considered in detail by Haase *et al.* and used to directly fit transient photoluminescence (TrPL) decay measurements on TADF films.[106, 107] With their method they can quantify the key rates involved in the process (k_f, k_{isc}, k_{risc}) as parameters in a set of ordinary differential equations (ODE), providing a simple method to evaluate TADF emitters. Nonetheless, their method assumes no non-radiative decay from the triplet state, and while that was confirmed experimentally for the specific materials they examined, it is unlikely to be true in general.

Another recent study based on the three-level model by Tsuchiya *et al.* addresses the same topic by deriving the analytic exact solution of the model. However, when applying this to experimental results, the non-radiative decay rates of singlet or triplet states cannot be fit uniquely without additional experimental data or are simply assumed to be absent.[107] The work of Vázquez *et al.* reports on a proposed new method to calculate rISC rates, [108] but this more specialised technique was not used in this work. In this study I investigate the effect of TADF rates on the device efficiency. I start my analysis by writing the expression of the EQE of an OLED:

$$EQE = \eta_{\mathrm{out}}\eta_{\mathrm{rec}}\eta_{\mathrm{S/T}}PLQY \tag{3.1}$$

where η_{out} is the optical outcoupling factor, η_{rec} is the probability of electrons (e) and holes (h) to recombine instead of escaping through the opposite electrode, $\eta_{\mathrm{S/T}}$ is the fraction of exciton leading to an emissive state and the PLQY is the photoluminescence quantum yield of the material.[35] In a pure fluorescence materials, in which only singlets are responsible for emission, $\eta_{\mathrm{S/T}}$ can be simply considered equal to 0.25. In TADF emitters, this value is usually considered equal to 1, since the triplet states can be converted into singlet one. But this is just an approximation, the dynamic nature of the RISC process requires a more precise calculation of the $\eta_{\mathrm{S/T}}$, which results to be dependent also on the non-radiative decay rates of the singlet and triplet states. The presence of non-radiative decays influences also the PLQY, in this study we define the multiplication of $\eta_{\mathrm{S/T}}$ and the PLQY as electroluminescence quantum yield (ELQY), or maximum IQE (when η_{rec} equals 1).

In the optimal case, TADF emitters can exhibit a PLQY equal to 100% when there is no significant non-radiative decay from either singlet or triplet states, which implies an ELQY of 100%.[46, 109] Instead, when non-radiative decays are present (either from a singlet or triplet state) both PLQY and $\eta_{\mathrm{S/T}}$ decrease, causing a reduction of the EQE.[110, 111] In this more realistic case, it is important to be able to allocate where the non-radiative decay is originating from.

In the first part of the study, I highlight the importance of considering non-radiative decay processes and its influence on the EQE. Interestingly, it is found that the ELQY may decrease to 50% with respect to the PLQY depending strongly on the relative distribution of non-radiative rates between singlet and triplet. Hence, knowing those rates is essential to predict the potential performance of TADF emitters. In a second step I define a fitting method to do this, which takes both TrPL and steady state PLQY data as input to determine all the excitonic rates. Finally, the method is applied to experimental data of two recent TADF emitters: 25ACA (2,5-bis(9,9-dimethyl-9,10-dihydroacridin-10-yl)benzonitrile) and 26ACA (2,6-bis(9,9-dimethyl-9,10-dihydroacridin-10-yl)benzonitrile).[61] From the extracted rates I can observe that all the rates are similar apart from the singlet non-radiative decay rate which is almost two orders of magnitude larger in 25ACA than in 26ACA.

3.2 MODEL AND METHODS

As a first step, I define the system of ODEs describing the time dependent TADF process where, for simplicity, I consider the involvement of only two excited states, singlet and triplet (see Figure 3.1) [105, 107] wherein k_{nrs} and k_{nrt} denote the non-radiative transfer rates for singlet and triplet states, respectively. In Table 3.1 and Table 3.2 I compare the ODEs describing the evolution of the singlet and triplet populations (S(t) and T(t)) for both optical and electrical excitation and provide an expression for the steady-state singlet population ($\overline{S}$) as well as for the PLQY and ELQY in the two cases.

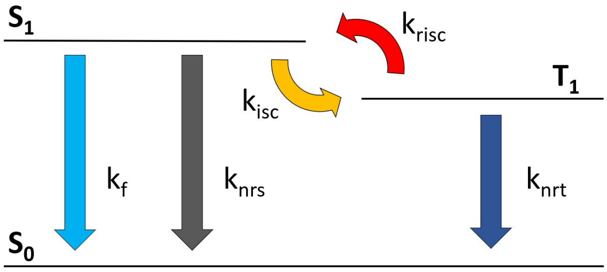

Figure 3.1: Schematic illustration of the TADF model described in this study. S_0 is the singlet ground state, S_1 and T_1 are the singlet and triplet excited states. Five processes are considered: radiative and non-radiative decay of S_1 (k_f; k_{nrs}), intersystem-crossing (k_{isc}), reverse intersystem-crossing (k_{risc}) and non-radiative decay of T_1 (k_{nrt}).

In Table 3.1 and Table 3.2 the term A has been introduced for better readability $(k_{risc} + k_{nrt})/k_{isc}$. The steady state solutions, indicated in the second line of Table 3.1 and Table 3.2, can be easily calculated by imposing the steady state condition to the systems. The quantum yield is defined as the number of emitted photons divided by the number of generated excitons G. The emitted photons can be expressed by the sum of the multiplication between the steady state population of each emissive state and its radiative decay rate, in this case I have assumed phosphorescence to be absent and therefore only the singlet state contributes to photon emission ($k_f{*}\overline{S}$), as indicated in the third line of Table 3.1 and Table 3.2. In the case of optical excitation, G generates only singlet states, while under electrical excitation one quarter of the generated exciton are singlets and three quarters are triplets. Having different generation terms in the two systems has the

Optical excitation
$\begin{cases} \dfrac{dS(t)}{dt} = G - (k_{\mathrm{f}} + k_{\mathrm{isc}} + k_{\mathrm{nrs}}) \cdot S(t) + k_{\mathrm{risc}} \cdot T(t) \\ \dfrac{dT(t)}{dt} = -(k_{\mathrm{risc}} + k_{\mathrm{nrt}}) \cdot T(t) + k_{\mathrm{isc}} \cdot S(t) \end{cases}$
$\overline{S} = \dfrac{G \cdot A}{(k_{\mathrm{f}} + k_{\mathrm{nrs}}) \cdot A + k_{\mathrm{nrt}}}$
$PLQY = \dfrac{k_{\mathrm{f}} \cdot \overline{S}}{G}$

Table 3.1: Mathematical formulas describing the system under optical excitation: rate equation system, singlet population solution at steady state and luminescence quantum yield formula. A is defined as $(k_{\mathrm{risc}} + k_{\mathrm{nrt}})/k_{\mathrm{isc}}$.

Electrical excitation
$\begin{cases} \dfrac{dS(t)}{dt} = \dfrac{1}{4}G - (k_{\mathrm{f}} + k_{\mathrm{isc}} + k_{\mathrm{nrs}}) \cdot S(t) + k_{\mathrm{risc}} \cdot T(t) \\ \dfrac{dT(t)}{dt} = \dfrac{3}{4}G - (k_{\mathrm{risc}} + k_{\mathrm{nrt}}) \cdot T(t) + k_{\mathrm{isc}} \cdot S(t) \end{cases}$
$\overline{S} = \dfrac{G}{4} \cdot \left(1 + \dfrac{3 \cdot k_{\mathrm{risc}}}{k_{\mathrm{risc}} + k_{\mathrm{nrt}}}\right) \cdot \left(\dfrac{A}{A \cdot (k_{\mathrm{f}} + k_{\mathrm{isc}} + k_{\mathrm{nrs}}) - k_{\mathrm{risc}}}\right)$
$ELQY = \dfrac{k_{\mathrm{f}} \cdot \overline{S}}{G}$

Table 3.2: Mathematical formulas describing the system under electrical excitation: rate equation system, singlet population solution at steady state and luminescence quantum yield formula. A is defined as $(k_{\mathrm{risc}} + k_{\mathrm{nrt}})/k_{\mathrm{isc}}$.

effect of modifying the steady state population of singlet $\overline{S}$ and triplet $\overline{T}$ states, and this causes the PLQY and ELQY to be different in the two cases. Imposing steady-state conditions gives expressions for the relevant singlet state populations and corresponding ELQY and PLQY. The equations shown in Table 3.1 and Table 3.2 are solved numerically with Python. The global fit described in the next section is performed using the Trust Region Reflective algorithm. The numerical analysis of the zero-dimensional ODEs presented here is a simpler alternative to the full electro-optical models in *Setfos*, where coupled 1D partial differential equations (PDEs) are solved for studying exciton dynamics and their interaction with electrical charges and the optical cavity.[31, 93, 112]

3.3 RESULT AND DISCUSSION

In this section I first show the change between PLQY and ELQY calculated with specific decay rates. Afterwards, I define the systems of equations describing two additional typical experimental technique used to characterize TADF films, PLQY with oxygen and TrPL. Finally, I use global fitting, with which I can estimate the entire set of decay rates from the three experimental results.

3.3.1 *Impact of the non-radiative decay rates and exciton populations*

In this section I will analyse the dependence of the PLQY and ELQY with k_{nrs} and k_{nrt}. The crucial point of the analysis is that the rate of non-radiative decay events is defined as the multiplication between rate constant and population, namely $k_{nrs}S$ or $k_{nrt}T$, respectively. In TADF OLEDs the population of triplets is usually much larger than the population of singlets[10], and therefore k_{nrt} produces a larger number of non-radiative decay events with respect to k_{nrs}. Moreover, as I have already seen, the steady state populations in case of optical and electrical excitation are different and therefore the number of non-radiative decay events will also change. In other words, conclusions drawn from the popular analysis of the luminescence quantum yield by optical excitation may be misleading and the electrical excitation present in OLED display and lighting applications will be affected more strongly by realistic values of non-radiative decay rates. The main message delivered in this section is: supposing a certain PLQY is measured experimentally, which value of ELQY is expected? To reply to this question, I assume the PLQY to be known and, from the PLQY formula in Table 3.1, I calculate the non-radiative decay rates which lead to this PLQY value. Subsequently, the ELQY is calculated with the rates found. In this analysis I assume k_f, k_{isc}, k_{risc} to be known. To calculate the non-radiative decay rates from the optical system I can simply revert the PLQY equation in Table 3.1 and express k_{nrs} as

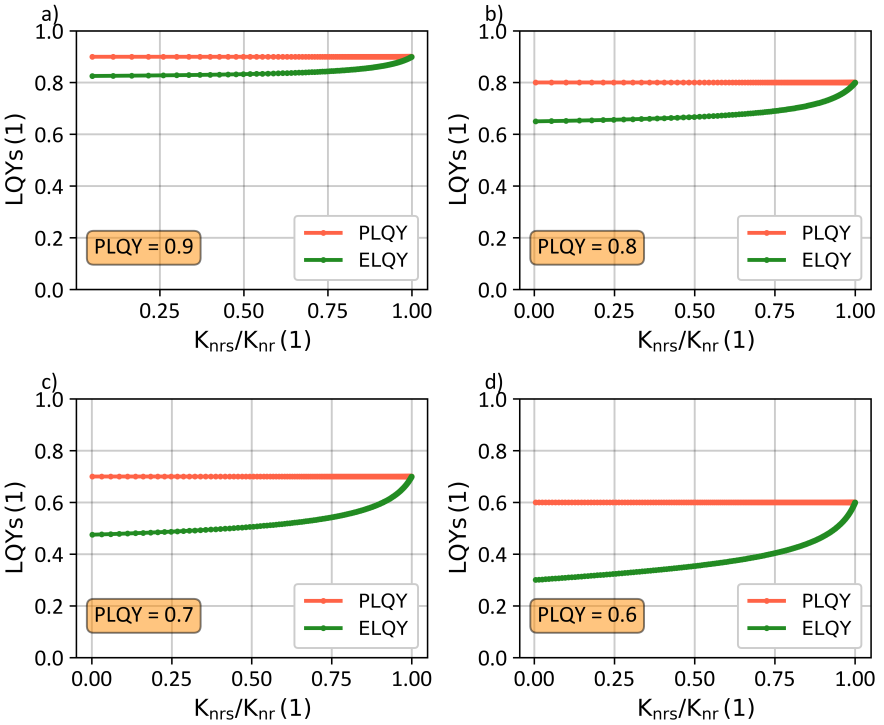

Figure 3.2: For a fixed PLQY of 0.9(a), 0.8(b), 0.7(c), 0.6(d) the ELQY is calculated for all possible couples knrs-knrt which are solutions of equation (1). In this calculation the other rates have been supposed known ($k_f = 10^7$ 1/s, $k_{isc} = 10^7$ 1/s and $k_{risc} = 10^6$ 1/s). On the x-axis $k_{nr} = k_{nrs} + k_{nrt}$.

a function of $\mathrm{k}_{\mathrm{nrt}}$ Equation 3.2. The solution of this equation is not unique since both $\mathrm{k}_{\mathrm{nrs}}$ and $\mathrm{k}_{\mathrm{nrt}}$ are unknown, however, since the goal of this work is to give an idea about the impact of the two rates on the yields, I can simply solve this equation with a fixed $\mathrm{k}_{\mathrm{nrt}}$ finding the corresponding $\mathrm{k}_{\mathrm{nrs}}$. In this way I will end up with many different couples ($\mathrm{k}_{\mathrm{nrs}}$; $\mathrm{k}_{\mathrm{nrt}}$) which are solutions of the equation. The ELQY is then calculated with the formula in Table 3.2 for each couple.

$$k_{nrs} = k_f \cdot \left[\frac{1 - PLQY}{PLQY}\right] - \frac{k_{nrt}}{A} \tag{3.2}$$

In Figure 3.2 the result of this analysis considering four PLQYs is shown. On the x-axis the quantity $k_{nrs}/k_{nr} = k_{nrs}/(k_{nrs} + k_{nrt})$ is used, denoting the relative strength of non-radiative singlet decay. Obviously, the PLQY remains constant at the chosen value for each point on the x-axis. I can observe that when $k_{nrs} = 0 \rightarrow k_{nr} = k_{nrt}$ ELQY is the lowest while when $k_{nrt} = 0 \rightarrow k_{nr} = k_{nrs}$ the ELQY is maximized and coincides with the PLQY. It is important to note that in the case of high PLQY values, the difference with the ELQY is small (Figure 3.2a), 82%-90% in case of PLQY=90%. Instead, considering a PLQY of 60%, as in Figure 3.2d, the calculated ELQY decreases significantly, from 60% to 31% (roughly a 50% reduction). This means that a film with an experimentally measured PLQY of 60% might exhibit an ELQY as low as 31%. The result of this parameter variation illustrates the importance of non-radiative triplet decay as it strongly affects the luminescence quantum yield for electrical excitation. This effect must be considered when estimating the EQE of TADF devices, especially when PLQY differs significantly from 100%.

3.3.2 *Photoluminescence quantum yield with oxygen ($PLQY_{O2}$)*

In the previous analysis I solved one equation with two unknowns, ending up with many k_{nrs}-k_{nrt} solutions of the system. To continue the analysis and extract all excitonic parameters, I need to take into account additional experimental results. A common experiment used to characterize TADF compounds is the measurement of the $PLQY_{O2}$.[113, 114] The presence of oxygen molecules has the effect of quenching the triplet states and therefore the contribution of delayed emission is not present, causing the $PLQY_{O2}$to be lower than the PLQY. In this condition, the equation of triplet can be removed from the system indicated in Table 3.1 and thus the sole equation of singlet states remains.

$$\frac{dS(t)}{dt} = G - (k_f + k_{isc} + k_{nrs}) \cdot S(t) \tag{3.3}$$

As before, the PLQY can be calculated from the steady state solution.

$$PLQY_{O2} = \frac{k_f}{k_f + k_{isc} + k_{nrs}} \tag{3.4}$$

In the above formula I made the approximation that the entire triplet population is quenched by oxygen. I must note that this is a good approximation when the host permeability to oxygen is high.[115] If this condition is not met the calculated PLQY will underestimate the value measured experimentally. Singlet quenching in the presence of oxygen is also possible[116, 117] but in a much smaller scale compared to triplet quenching. Therefore this effect is not taken into consideration.

3.3.3 *Modelling of a transient photoluminescence experiment*

Until now, I have assumed knowledge of the other rates involved in the ODE systems, namely k_f, $k_{isc}$and k_{risc}. An established way to estimate these quantities is to perform a TrPL experiment and perform a mathematical fit. Following the analysis of Haase *et al.*[106] I defined the system indicated in Equation 3.5. In contrast to their work I introduce non-radiative decay for singlets and triplets in the ODE system.

$$\begin{cases} \dfrac{dS(t)}{dt} = -(k_\mathrm{f} + k_\mathrm{isc} + k_\mathrm{nrs}) \cdot S(t) + k_\mathrm{risc} \cdot T(t) \\ \dfrac{dT(t)}{dt} = -(k_\mathrm{risc} + k_\mathrm{nrt}) \cdot T(t) + k_\mathrm{isc} \cdot S(t) \end{cases} \tag{3.5}$$

3.3.4 *Global Fit*

I have now a set of three systems of differential equations which describes three experiments: PLQY (Table 3.1-3rd line), PLQYO2 (Equation 3.4) and TrPL (Equation 3.5). The estimation of the decay rates (k_f, k_{isc}, k_{risc}, k_{nrs} and k_{nrt}) can now be performed with an appropriate fitting algorithm. The best strategy when dealing with different experiments described by equations having several parameters in common is to perform a global fit, where the three sets of experimental data are fitted at the same time. This approach allows the extracted parameters to be more reliable since a potential correlation between them will be reduced.[92] In Figure 3.3 a schematic representation of the inputs/outputs of the fitting algorithm is shown. It is important to mention that the three experimental results are of different shape from a numerical point of view, the TrPL consist of a curve with several data points, while the PLQYs have only one data point each. Clearly, the optimization algorithm will tend to reach a solution where the TrPL experiment is well fitted at the expenses of the other two if each fitting target has the same weight. In order to obtain a well-balanced fit, it is necessary to include different weights of the error for the three experiments, essentially, I should give more importance to the PLQY values.

3.4 EXPERIMENTAL RESULT

The methodology is applied to experimental data from two host-guest systems, in the form of films, one containing 25ACA and the other 26ACA as emissive TADF molecule at 1wt% in Zeonex as host. The samples were fabricated by Dalius Gudeika and Juozas Grazulevicius from Kaunas University of Technology. The experimental results were obtained by Andrew Danos from University of Durham. The experimental data for PLQY and $PLQY_{O2}$for the two films are indicated in Table 3.3. Figure 3.4 shows the experimental data and the resulting fit. The fit reproduces almost perfectly the TrPL and PLQYs of the experimental data. In both cases, but most predominantly in the case of 26ACA, the PLQYO2 fit shows a discrepancy with the experimental value (0.12 instead of 0.15 in 25ACA and 0.21 instead of 0.41 in 26ACA). A possible explanation could be that in Equation 3.3

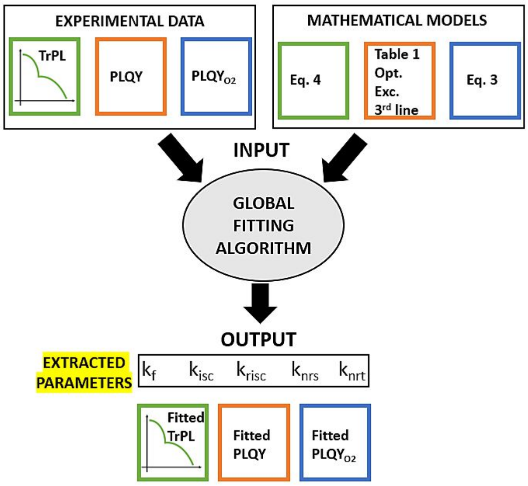

Figure 3.3: The global fitting algorithm uses the parametrized mathematical model in order to minimize the difference between experimental (target) and fitted PLQY, PLQY$_{O2}$and TrPL data by adjusting the 5 excitonic parameters.

	PLQY	PLQY$_{O2}$
25ACA	0.42	0.15
26ACA	0.71	0.41

Table 3.3: Experimental values of PLQY and PLQY$_{O2}$for the two films, 25ACA and 26ACA. These two values represent two targets of the fitting algorithm.

and Equation 3.4 I considered the entire population of triplets to be quenched by oxygen, while in the experiment this might not be entirely the case.[118] Consistent with this possibility the fit of PLQY$_{O2}$has considerably larger error.

The extracted parameters are indicated in Table 3.4 and shown in Figure 3.5 for a direct comparison. The results suggest that k_f, k_{isc}, and k_{risc} are all higher in 26ACA, similar to what was previously reported in DPEPO (25ACA: $k_f = 3.6 \times 10^6$ 1/s; $k_{isc} = 1.5 \times 10^7$ 1/s; $k_{risc} = 0.6 \times 10^6$ 1/s . 26ACA: $k_f = 4.3 \times 10^6$ 1/s; $k_{isc} = 2.7 \times 10^7$ 1/s; $k_{risc} = 1.8 \times 10^6$ 1/s).[61] Uniquely to this work, I am also able to estimate the non-radiative decay rate of the singlet and triplet states, showing that k_{nrs} in 26ACA is almost two orders of magnitude smaller than in 25ACA while k_{nrt} is quite similar between the two. I must observe that the error associated to the non-radiative decay rate of singlet states is quite large compared to the other parameters. This fact is however expected because the non-radiative decay rate is the parameter which influences the experimental results the least: k_{nrs} mainly influences the prompt decay of the TrPL and PLQYO2 but since k_f and k_{isc} are usually two or three orders of magnitude larger, k_{nrs} has a comparably smaller effect. Therefore, it is more difficult for the

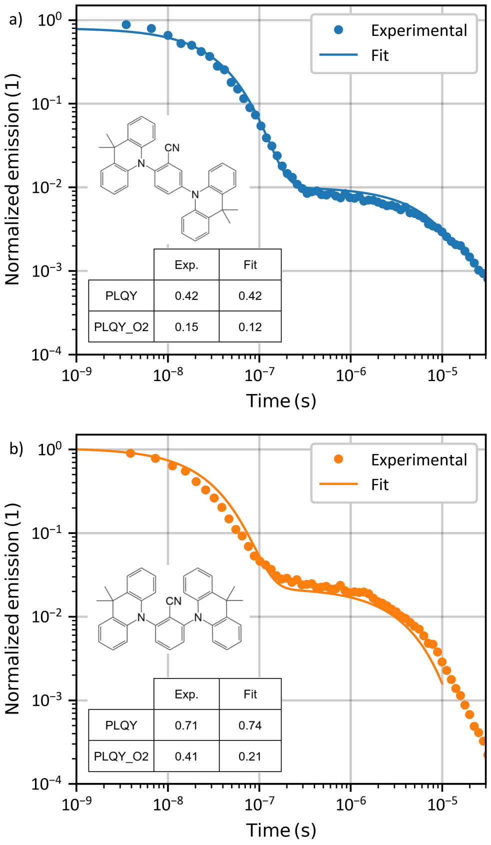

Figure 3.4: Result of the global fit applied to two TADF films: 25ACA (a) and 26ACA (b). The experimental TrPL decay is shown with the resulting fit. The inset table indicates the experimental and fitted values for PLQY and PLQY_{O2}.

fitting algorithm to estimate it properly. As a final step I can calculate the expected ELQY for the two films, using the formula indicated in Table 3.2 with the extracted rates. The resulting ELQY, or maximum IQE, is 0.36 for 25ACA and 0.69 for 26ACA. The traditional way of calculating the IQE, assuming $\eta_{S/T} = 1$, would have predicted values of 0.42 and 0.71 for 25ACA and 26ACA, respectively. It is important to note that in this case the difference between PLQYs and ELQYs is minimal, but as showed in Figure 3.2 it can be much larger depending on the specific rates considered.

3.5 ADDITIONAL ANALYSIS AND FURTHER MODELLING WITH A FULL ELECTRO-OPTICAL MODEL

The model I defined is not particularly complex, only two excited states are considered, and phosphorescence is assumed to be absent. The complexity of the system can be increased by including additional excited states. However, this possibility requires new equations to

Extracted parameters	25ACA	26ACA
k_f[1/s]	$(3.2 \pm 0.3) \times 10^6$	$(7.2 \pm 0.1) \times 10^6$
k_{isc}[1/s]	$(23 \pm 0.1) \times 10^6$	$(26.8 \pm 0.5) \times 10^6$
k_{risc}[1/s]	$(3.5 \pm 0.1) \times 10^5$	$(8.5 \pm 0.2) \times 10^5$
k_{nrs}[1/s]	$(9.1 \pm 36) \times 10^4$	$(1.1 \pm 5.8) \times 10^3$
k_{nrt}[1/s]	$(8.0 \pm 0.1) \times 10^4$	$(8.9 \pm 0.5) \times 10^4$

Table 3.4: Decay rates extracted from the fitting algorithm. The error is calculated from the Jacobian matrix, which is an output of the fitting algorithm.

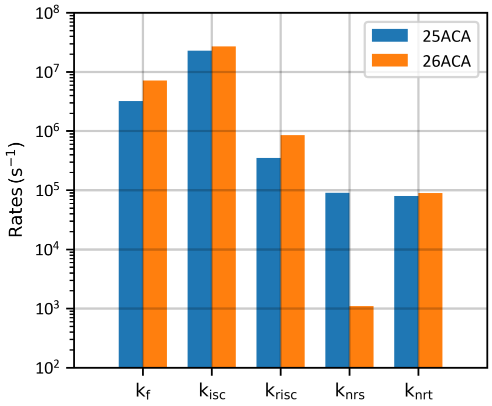

Figure 3.5: Plot of the decay rates extracted from the fitting algorithm for 25ACA and 26ACA.

be defined, which will increase the number of unknown parameters significantly. Having a large number of free parameters in a fitting algorithm will probably result in overfitting which would decrease the confidence of the extracted values. I therefore followed the premise of making the model as complex as necessary but as simple as possible. Nevertheless, I would like to briefly discuss here how the proposed model can be extended in future studies. Additional complexity can be introduced by including the radiative decay of the triplet state. In case phosphorescence is found to contribute significantly to the emission (i. e., if clearly observed from transient spectral data at low temperatures) it could be easily considered in the model by modifying the triplet equation with a k_{ph}term. Other phenomena that could be included in the model are annihilation processes such as singlet-singlet, singlet-triplet and triplet-triplet annihilation. As these processes are exciton-density dependent, it would be beneficial to include experiments performed with different laser intensities. Moreover, in this case the equations become non-linear and therefore it is necessary to quantify the exciton density from independent experiments or simulations.[119] Finally, the effect of exciton-polaron quenching should be considered for a complete analysis and powerful prediction of the maximum IQE in an OLED device. The model extension would be feasible. But clearly, additional data such as transient electroluminescence from full devices[83, 120] or TrPL on full or single-carrier devices would be required as fitting target. Also, the number of charge carriers would need to be provided, for example by using device simulations.[121] Once the entire set of excitonic parameters are extracted with this simple ODE method, they could be used in a 1D full electro-optical model such as *Setfos*.[93] This option would allow to simulate the OLED by taking into account the actual optical characteristics of the entire stack and important phenomena like spatial dependency of the radiative decay rates (Purcell factor) and charge/exciton distribution, which is required when calculating the annihilation and exciton-quenching losses.[8, 92] Further details can be added by including the 3D Master-Equation model, which consider non-local exciton energy transfer (Förster, Dexter), energy transfer across layer interfaces and correlated/uncorrelated energetic disorder.[122]

3.6 CONCLUSIONS

In this work I studied a TADF system described as a three-levels model including non-radiative decays of singlet and triplet states. The influence of non-radiative processes on the EQE has been deeply investigated and quantified. A global fitting algorithm which takes as input data from transient and steady state experiments (TrPL, PLQY and $\mathrm{PLQY}_{\mathrm{O2}}$) was introduced. Besides the determination of k_f, k_{isc} and k_{risc}, which themselves are easily inferable with a simple TrPL fit, this algorithm allows the extraction of k_{nrs} and k_{nrt}, which are usually more difficult to assess separately. Finally, I applied this fitting method to experimental results of two emissive films. The result of this analysis shows that the rates are quite similar among the two materials apart from the non-radiative decay of singlet states which is almost two orders of magnitude larger in 25ACA than in 26ACA. This study aims to provide a new and simple method to estimate all the relevant processes in TADF emitter systems, allowing a better estimation of the maximal EQE in a real TADF OLED.

4

DETAILED ELECTRO-OPTICAL MODELING OF THERMALLY-ACTIVATED DELAYED FLUORESCENT OLEDS WITH DIFFERENT HOST-GUEST CONCENTRATIONS.

In the previous chapter I investigated the fundamental properties of TADF emitters, analyzing optical experimental results obtained on TADF films. The next step is to study the effects occurring in these emitters when embedded in a complete OLED.

Herein, I analyse four thermally activated delayed fluorescence OLEDs with varied host-guest ratio in the emissive layer. These devices are characterized and modelled in steady-state, under transient conditions and in the frequency domain.

This chapter reports the peer-reviewed article "Detailed electro-optical modeling of thermally-activated delayed fluorescent OLEDs with different host-guest concentrations"[31]. The co-authors supported with the following contributions: Dr. Sandra Jenatsch, Dr. Simon Züfle, Prof. Beat Ruhstaller and Prof. Wolfgang Brütting contributed with scientific discussions and with support in the scientific development of the article; Prakhar Sahay contributed with the fabrication of the OLEDs and the TADF films; Markus Schmid provided the transient photoluminescence measurements.

4.1 INTRODUCTION

The simplest emissive layers (EMLs) of TADF OLEDs consist of the emissive TADF molecules (guest) embedded in a matrix (host). A key role, in this context, is played by the host-guest ratio, which has a strong impact on the OLED's performance. I can identify the two main processes impacted by the host-guest ratio to be: 1) modified charge injection and transport in the emissive layer[29, 123] and 2) aggregation of guest molecules. Studies have shown that at high concentrations the guest molecules tend to form aggregates and agglomerates.[124–126] This might lead to a reduction of the external quantum efficiency (EQE) caused by the surge of second-order non-radiative decays such as triplet-triplet annihilation (TTA), singlet-polaron quenching (SQP) and triplet-polaron quenching (TPQ)[127] or concentration quenching, which reduces the photoluminescence quantum yield (PLQY).[128, 129] In addition, especially in blue-emitting compounds, the energy released by those loss mechanisms is large enough to cause bond cleavage and therefore a faster degradation of the device.[130] Consequently, it is extremely important to fully understand and investigate these processes and optimize the OLED accordingly. Often, the host-guest ratio is simply optimized by time-consuming and costly trial-and-error experiments. A more elegant way would be to replace this process by combining advanced characterization techniques and subsequent predictive device simulations. This dual approach allows to gain a deeper comprehension of all relevant processes and their roles in the final performance of the OLED. In this study I analyse a series of TADF OLEDs with systematically varied host-guest concentrations. As a first step I analysed transient electroluminescence data (TEL), from which I identified that for low concentration the emitter molecules act as trap state. With this assumption, I can quantitively simulate the steady-state, transient and impedance response of all devices at once. The final and excellent correspondence between experiments and simulations guarantees that the model has been defined in a correct way and that all the important processes are captured. Moreover, this analysis allows us to estimate the electro-optical properties of the emissive layer composed of a host-guest mixture of specific concentration. In the last section I focused my attention on the efficiency curves, where I investigated the role of TTA, TPQ-n and TPQ-p in the efficiency roll-off behaviour for each device. I would like to emphasize the importance of analysing multiple experimental techniques. Only with this strategy a reliable estimation of the modeling parameters can be obtained [92] which is a key requirement for further optimizations.

4.2 FABRICATION

The devices were fabricated at Augsburg University by Prakhar Sahay.

Fabrication of the devices was carried out on pre-patterned 90 nm thick Indium Tin Oxide (ITO) on glass substrates provided by Kintec. Substrate preparation for deposition includes cleaning which is carried out in clean room using Acetone and Isopropyl alcohol bath in ultrasonicator each for 10 minutes respectively followed by UV-Ozone treatment with a mercury lamp for 15 minutes. The substrates are then spin coated with PEDOT:PSS (Clevios^{TM} PEDOT:PSS; AI 4083 from Heraeus) and dried on a hot plate for 30 minutes at 150 degrees Celsius under ambient conditions to get rid of the water content. The ITO and PEDOT:PSS together act as the anode for these OLED devices. The substrates are then transported to the glovebox in wafer trays wrapped in parafilm followed by loading them in the vacuum chamber located inside the glovebox thus under Nitrogen environment.

The deposition of organic layers by thermal deposition was carried under a vacuum of $\sim 10^{-7}$ mbar. The device structure includes 10 nm Molybdenum Oxide (MoOx) (supplied by sigma Aldrich), 5 nm 3,3′-Di(9H-carbazol-9-yl)-1,1′-biphenyl (mCBP) (from Lumtec) and 20 nm tris(4-carbazoyl-9-ylphenyl)amine (TCTA) (from Lumtec) as hole transport side (HTL). The EML consist of 20 nm of mCBP-CN and DMAC-TRZ (both supplied by Lumtec) as host-guest system and the concentration of DMAC-TRZ is varied to 5 wt%, 10 wt%, 20 wt% and 50 wt%. This is followed by the deposition of 5nm Bis[2-(diphenylphosphino)phenyl]ether oxide (DPEPO) (supplied by TCI) as an exciton blocking layer. For electron transport layer (ETL), 50 nm 2,2′,2″-(1,3,5-Benzinetriyl)-tris(1-phenyl-1-H-benzimidazole) (TPBi) (from Lumtec) is evaporated, topped off with 0.5 nm Lithium Fluoride (LiF) (from Lumtec) and 100 nm Aluminium (supplied by Lesker) as the cathode.

The device structure with the energy levels is shown in Table 4.2.

4.3 EXPERIMENTAL RESULTS

In this section, the employed experimental techniques and obtained results are described and discussed. The all-in-one measurement platform Paios was used to perform all DC, AC and time-dependent opto-electronic characterization experiments. The reader can refer to Chapter 2 for the details about the experimental techniques.

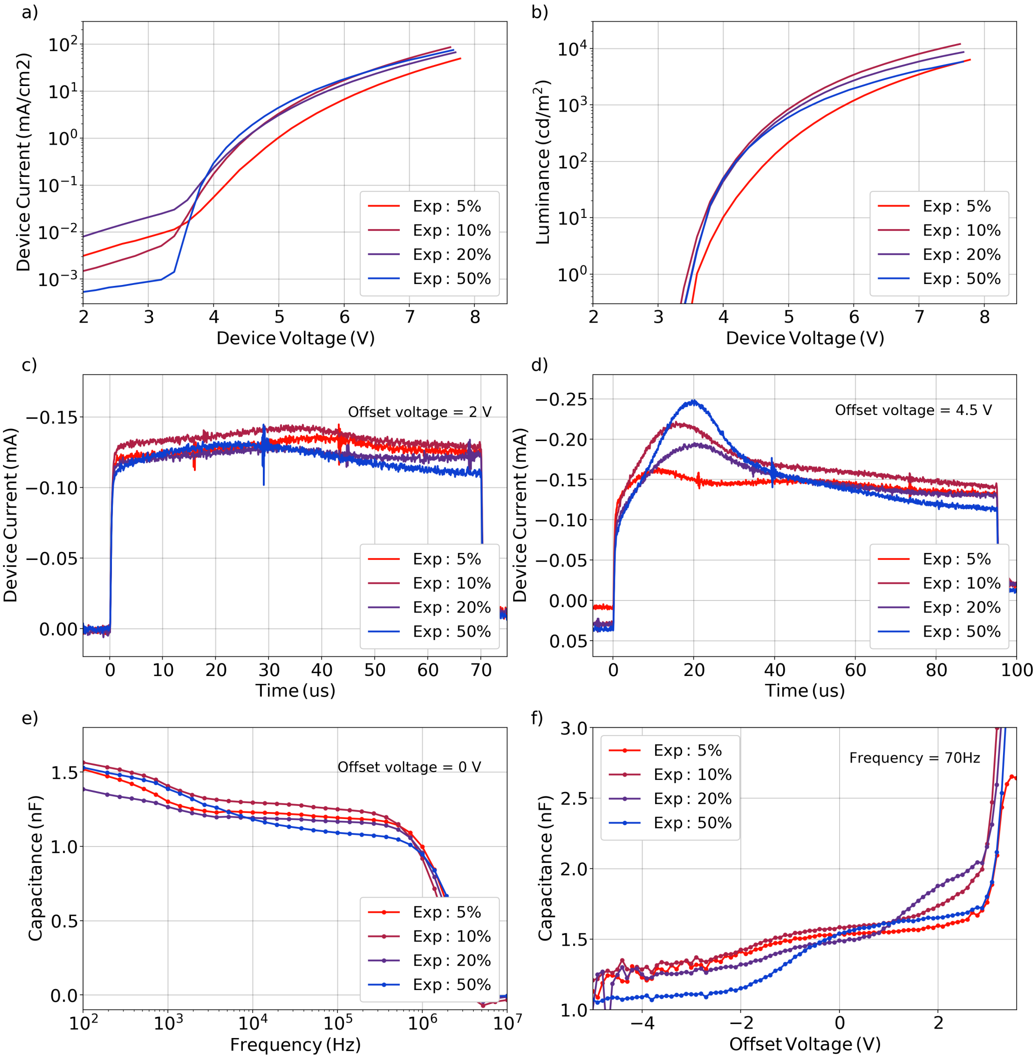

Figure 4.1: Experimental results of each device: (a) JV; (b) Luminance vs voltage; (c) injection-CELIV with V_{offset} = 2 V; (d) injection-CELIV with V_{offset} = 4.5 V; (e) C-f with V_{offset} = 0 V; (f) C-V with frequency = 70 Hz.

4.3.1 *Current-voltage-luminance (JVL) curves*

From the experimental results in Figure 4.1a, the device with 5% concentration gives a lower current with respect to all the other devices. The currents for the 10, 20 and 50% concentration are very similar, but with a slightly steeper turn on of the 50% device. For all devices the turn-on voltage is approx. 3.5 V.

4.3.2 *Injection-CELIV*

This experiment was performed with different V_{offset}, from 1 V to 6 V with 0.5 V step. The ramp rate is 0.1 V/µs for each of the measurements, the final voltage is -5 V. From the experimental results the formation of two separate peaks can be observed in all the devices, a broad one is already visible with an $V_{\text{offset}} = 2$ V, below turn on (Figure 4.1c), while the second one, much larger, appears only above turn on voltage (Figure 4.1d). Note that the peak at longer times is still present in the 4.5 V experiments, even if partially covered by the initial one. The occurrences of a peak with an $V_{\text{offset}} = 2$ V indicates the presence of charges in the devices well below the turn on voltage of the OLED. I can also remark that increasing the guest concentration causes a shift of the peak to the left i. e. to shorter carrier extraction times. Depending on which charge carrier is already present in the device, this suggests a change in the transport properties of the EML. When using a $V_{\text{offset}} = 4.5$ V an additional, significantly larger peak can be seen. This is expected since at 4.5 V the devices are already above turn-on which occurs at approx. 3.5 V. I can also observe that the height of the peak is different for all devices. This is directly related to the amount of charges flowing through the device during the V_{offset}. This initial peak is attributed to injected charge carriers and exhibits the opposite trend in peak time vs guest concentration compared to the broad peak which is present below turn on.

4.3.3 *Impedance spectroscopy*

Figure 4.1e shows the C-f plot at a fixed V_{DC} of 0 V. For all the devices the capacitance is increasing at low frequency, it reaches a plateau in the range of 10 kHz-300 kHz – which is attributed to the geometrical capacitance of the (empty) device – and then decreases sharply at 1 MHz because of the series resistance. The most interesting result from the C-f plot is the additional capacitance plateau present at low frequency. This result suggests that at 0 V charges are already injected into the stack and accumulate at a particular interface. Figure 4.1f shows the C-V plot at a fixed frequency of 70 Hz. For all the devices a similar effect can be seen, where below -2V the capacitance is the geometric one (C_{geo}, with values in the range of 1.1-1.3 nF for all the devices); with increasing voltage I can observe a clear transition from C_{geo} to a plateau (C_{plat}) at a transition voltage (V_t) of roughly -2 V, suggesting the injection of charges already at this negative bias; finally, above 3 V, the capacitance sharply increases and then drops, which indicates injection of electrons and holes and subsequent recombination. From Figure 4.1f it can be observed that the 50% device has a slightly lower geometrical capacitance. This is an indication that this device has an unintentionally larger thickness. However, this small difference does not affect the overall results of this study.

Device	Plateau	Calculated thickness
5%	1.55 nF	68 nm
10%	1.60 nF	66 nm
20%	1.50 nF	70 nm
50%	1.65 nF	65 nm

Table 4.1: Calculated thickness associated to plateau in CV experimental results.

4.3.4 *Analysis of C-V results*

From the experimental C-V shown in Figure 4.1f, a capacitance plateau occurring between 0 V and 1 V can be observed at slightly different voltage for each device. The increase of capacitance below 0 V is a clear signature of the presence of one or multiple polar layers.[96, 131] Assuming a permittivity of 3 I calculated the thicknesses associated to the plateaus (Table 4.1) from the formula $C = \frac{\epsilon_0 \epsilon_r A}{d}$.

According to the nominal thickness described in the fabrication paragraph the thickness of TPBi + DPEPO is 55 nm and EML + TPBi + DPEPO is 75 nm. The interpretation is that for all the devices there is an early injection of holes starting at around -2 V which accumulate at the TCTA/EML or EML/DPEPO interface. Simulations described in the next sections confirm this hypothesis. Additionally, there are three aspects that I want to comment briefly. First, at reversed bias the 50% device shows a lower C_{geo} with respect to the other devices which can be attributed to an unintended larger thickness of this device. Second, the device with 20% concentration shows an additional shoulder starting at 1 V. At the moment, I cannot explain this feature in detail. I speculate that at 1 V holes already accumulated at the TCTA/EML or EML/DPEPO interface are able to overcome it, which would result in an increased capacitance. This feature could not yet be reproduced in my simulations but is further investigated. It is also worth to mention that this feature disappears for C-V measurements at different frequencies. Third, in 50% device the capacitance shift from C_{geo} to C_{plat} occurs at -1 V, slightly higher than the other devices. It could be explained by considering a different polarity of the EML in this device, as explained in Section 4.4.5.

4.3.5 *Transient electroluminescence*

TEL is performed with an offset voltage of -5 V and a pulse duration of 500 µs (Figure 4.2a-inset). This experiment was performed with different pulse height, from 3 V to 7 V. In Figure 4.2a, the normalized emission decay of the four devices is shown with a voltage pulse of 6 V. From the experimental result it is important to note that in the 5% device a clear overshoot in the first 2-3 µs of the turn-off electroluminescence decay is observed, while the other three samples show a monotonic decay. This overshoot has already been investigated by Regnat *et al.*[83] and attributed to emission zone splitting. In this publication Regnat *et al.* explained that during steady state charges accumulate at the respective blocking layers inside the EML and once the voltage switches to reverse bias electrons and holes start flowing backwards to Al and ITO, respectively, thereby a large number of electrons and holes will meet approximately in the middle of the EML, giving rise to the short-lived TEL overshoot. Although this explanation cannot be ruled out completely, it is difficult to reason why this effect is here only present in the 5% device. In previous work, this TEL overshoot after turn-off has alternatively been explained by the presence of trap states.[132] Indeed, this effect could be reproduced with simulations by including traps in the EML. Figure 4.2b shows that an increased trap density in the EML give rise to a TEL overshoot. This result is an indication that for 5% the guest molecules in the EML act as trap states, while for higher concentration they don't.

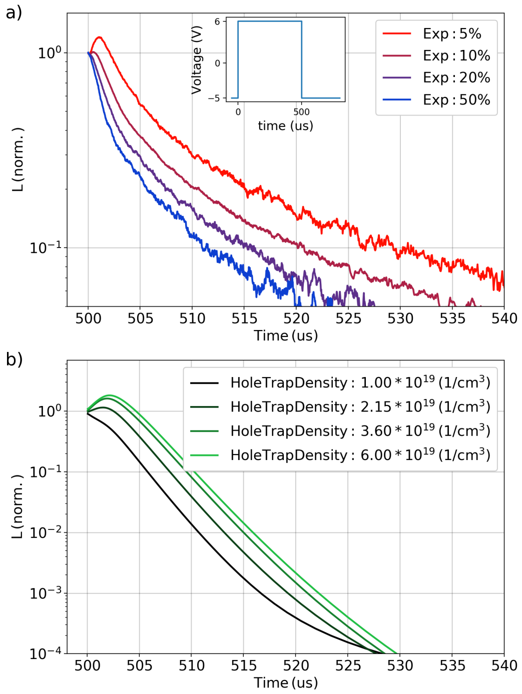

Figure 4.2: Transient EL analysis: (a) experimental TEL turn-off normalized emission with a voltage pulse of 6 V (inset: schematics of the applied voltage pulse); (b) simulated TEL turn-off normalized emission with different hole trap density in the EML.

4.4 SIMULATIONS

To analyse and understand the results described in the experimental section, I modelled the device behaviour with the simulation software Setfos. For details about *Setfos* the reader can refer to Section 2.3.

In these sections the key physical processes governing these OLEDs are discussed and explained with the support of simulations. The final simulations are performed with the parameters indicated in Table 4.2 and the resulting plots are shown in Figure 4.4. The modelled stack is presented in Figure 4.3. I must note that with Setfos different molecular species cannot be included in a single layer and therefore the EML is modelled with an effective HOMO/LUMO energy level and electron/hole mobility. Another approximation done in the study is related to the presence of multiple polar layers inside the stack (DPEPO, mCBPCN and TPBi). For simplicity, only TPBi is considered polar in simulations (apart from the device 50%, where the polarity of the EML appears to play an important role, see Section 4.4.5).

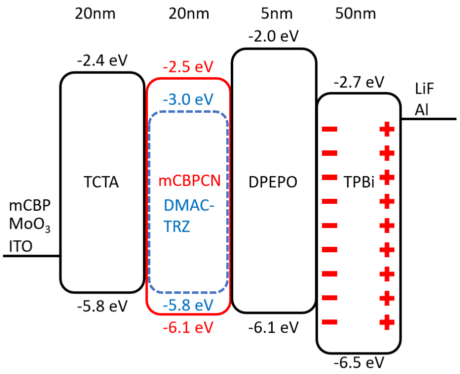

Figure 4.3: Device structure considered in simulation. TPBi has been assumed to be the only polar layer in the stack for 5-10-20% devices. The energy levels indicated in the image are the ones found in literature, see Table 4.2.

4.4.1 *Charge transport in the EML*

Before going into detail about the modeling of the different devices, I tackle the process of charge transport in the EML, which is concentration-dependent. As seen from the energetic diagram in Figure 4.3, there is a significant HOMO/LUMO energy difference between the host and the guest molecules. It is reasonable to infer that for small guest concentrations, the guest molecules act as trap states. In this case the large distance between guest molecules precludes any transport among them. Increasing the dye dopant concentration, the distance between guest molecules decreases, allowing charge transport via the guest molecules.[133] With the support of the TEL simulation's result, I can identify two distinct regimes depending on the guest concentration: the “low concentration” regime, where transport occurs on the host molecules and the guest molecules act as trap states, and the “high concentration” regime, where injection and transport occurs on the guest molecules. To replicate these two regimes in simulations, I assume the HOMO/LUMO energy levels of the EML to be similar to the guest (host) ones and exclude (include) trap states in case of high (low) guest concentration. The “low concentration” regime is applied to the device with 5% guest concentration while the ”high concentration” regime to all the other devices (see Table 4.3 and Table 4.4).

4.4.2 *Additional simulation details*

From the previous sections it is clear that in multiple experiments there is an initial injection of charges in the stack already at negative bias (injection-CELIV, IS (C-f, C-V)). These results suggest the presence of a polar layer. As described by W. Brütting *et al.*[15], having a polar layer inside the stack introduces an additional (fixed) electric field inside the polar layer. The origin of this electric field is spontaneous orientation polarization and it can be expressed by a net positive and negative sheet charge density at the two extremities of the layer. This phenomenon can be simulated with Setfos as described in S. Altazin *et al.*[96] with the use of two thin boundary layers with positive and negative carrier doping. Modeling of TPBi plays a crucial role in these simulations. TPBi molecules possess a large permanent dipole moment, which - combined with a strong molecular orientation - induce the whole layer to be polar. According to Coehoorn *et al.*[134] a direct consequence of the strong dipole moment of TPBi is that electron transport is highly dispersive. Differently from the approach taken by Coehoorn *et al.*, I modelled these two effects separately: polarity can be recreated in *Setfos* with fixed positive and negative charge densities at the two extremities of TPBi, as described above, while the dispersive transport is taken into consideration by adding trap states for electrons. The excitonic parameters used in simulations are indicated in Table 4.5, and they are estimated from transient PL experiments with use of a specific fitting procedure.[135] Details about the method and experimental results are shown in the next section. In my simulations, the excitonic model is implemented with customizable 1D rate equations which are fully coupled to the charge densities obtained from the drift-diffusion model.[112, 136] For each exciton, several parameters must be defined: generation coefficient, radiative decay rate, non-radiative decay rate, triplet-triplet annihilation rate, singlet-singlet annihilation rate and optionally other parameters. I can distinguish mono-molecular (like radiative, non-radiative, intersystem crossing, . . .) and bi-molecular (like triplet-triplet annihilation, triplet-polaron quenching, . . .) excitonic rates. The first type does not depend on the exciton or charge density, and therefore the unit of these rates is s-1, while the second instead depends on the exciton or charge density, and the unit, in this case, is cm^3s^{-1}. Alternatively, for further in-depth analysis and consideration of long-range interactions across nearest neighbours and layer interfaces a 3D master equation model for exciton dynamics is available in Setfos.[112] The use of this hybrid and coupled 1D drift-diffusion and 3D master equation model is beyond the scope of this study and will be subject of follow-up work.

4.4.3 *Simulation parameters*

The simulation software requires several input parameters such as the refractive indices, the layer thicknesses, HOMO/LUMO energy levels and electron/hole mobilities. In Table 4.2 all the values used in simulations are indicated. Obviously, the material parameters of the mixed host-guest EML with various concentrations has not been characterized before in detail. Therefore, one of the goals of this study is to be able to provide an estimation for the electrical material parameters by optimizing the agreement between experimental and simulation results. The extracted parameters of the EML layer are shown in Table 4.3 and Table 4.4. The excitonic parameters were extracted from transient PL performed on films (see Table 4.5).

Parameter	Reference	Used in simulation
Hole injection barrier (eV)	-	0.2
TCTA HOMO LUMO level (eV)	5.8/2.4 [133]	5.8/2.4
TCTA hole mobility ($cm^2V^{-1}s^{-1}$)	3×10^{-4} [137]	3×10^{-4}
TCTA electron mobility ($cm^2V^{-1}s^{-1}$)	-	1×10^{-6}
DPEPO HOMO LUMO level (eV)	6.1/2.0 [138]	6.1/2.25
DPEPO hole mobility ($cm^2V^{-1}s^{-1}$)	-	1×10^{-9}
DPEPO electron mobility ($cm^2V^{-1}s^{-1}$)	5.62×10^{-6} [139]	5.62×10^{-6}
TPBi HOMO LUMO level (eV)	(6.2-6.7)/2.7 [140, 141]	6.5/2.5
TPBi hole mobility ($cm^2V^{-1}s^{-1}$)	-	1×10^{-6}
TPBi electron mobility ($cm^2V^{-1}s^{-1}$)	3.16×10^{-5} [142]	3.16×10^{-5}
TPBi sheet charge density (mC/m^2)	0.93-1.1 [143]; 1.4 [144]; 2.6 [145]	2.64
TPBi electron trap density (cm^{-3})	-	5.48×10^{18}
TPBi electron trap depth (eV)	-	0.225
TPBi electron trap capture rate (cm^3s^{-1})	-	1×10^{-10}
Electron injection barrier (eV)	-	0.1
DMAC-TRZ HOMO LUMO level (eV)	-	see Table 4.3 and Table 4.4
mCBPCN HOMO LUMO level (eV)	6.1/2.5	see Table 4.3 and Table 4.4

Table 4.2: In the "Reference" column the values from literature are indicated. The actual values used in simulation are indicated in the "Used in simulation" column.

Parameter	5%	10%
EML HOMO LUMO level (eV)	6.0/2.25	5.9/3
EML zero field hole mobility ($cm^2V^{-1}s^{-1}$)	7×10^{-7}	3.87×10^{-7}
EML field-enhancement coefficient for holes ($m^{1/2}V^{-1/2}$)	4.64×10^{-5}	4.64×10^{-5}
EML zero field electron mobility ($cm^2V^{-1}s^{-1}$)	1×10^{-6}	6×10^{-7}
EML field-enhancement coefficient for electrons ($m^{1/2}V^{-1/2}$)	2×10^{-5}	2×10^{-5}
EML sheet charge density (mC/m^2)	-	-
EML electron trap density (cm^{-3})	1×10^{17}	-
EML electron trap depth (eV)	0.75	-
EML electron trap capture rate (cm^3s^{-1})	1×10^{-12}	-
EML hole trap density (cm^{-3})	1×10^{17}	-
EML hole trap depth (eV)	0.2	-
EML hole trap capture rate (cm^3s^{-1})	1×10^{-12}	-

Table 4.3: EML parameters used in simulations (5% and 10%).

Parameter	20%	50%
EML HOMO LUMO level (eV)	5.9/3	5.9/3
EML zero field hole mobility ($cm^2V^{-1}s^{-1}$)	2.44×10^{-7}	2.7×10^{-7}
EML field-enhancement coefficient for holes ($m^{1/2}V^{-1/2}$)	4.64×10^{-5}	4.64×10^{-5}
EML zero field electron mobility ($cm^2V^{-1}s^{-1}$)	3×10^{-7}	4.37×10^{-7}
EML field-enhancement coefficient for electrons ($m^{1/2}V^{-1/2}$)	2×10^{-5}	2×10^{-5}
EML sheet charge density (mC/m^2)	-	-0.7
EML electron trap density (cm^{-3})	-	-
EML electron trap depth (eV)	-	-
EML electron trap capture rate (cm^3s^{-1})	-	-
EML hole trap density (cm^{-3})	-	-
EML hole trap depth (eV)	-	-
EML hole trap capture rate (cm^3s^{-1})	-	-

Table 4.4: EML parameters used in simulations (20% and 50%).

Parameter	5%	10%
Radiative decay rate – singlet (s^{-1})	2.38×10^{7}	2.06×10^{7}
Intersystem crossing rate (s^{-1})	2.92×10^{7}	2.68×10^{5}
Reverse intersystem crossing rate (s^{-1})	7.5×10^{5}	7.5×10^{5}
Generation efficiency – singlet	0.25	0.25
Generation efficiency – triplet	0.75	0.75

Table 4.5: Excitonic parameter extracted from TrPL fitting (5% and 10%).

Parameter	20%	50%
Radiative decay rate – singlet (s^{-1})	2.12×10^{7}	1.81×10^{7}
Intersystem crossing rate (s^{-1})	2.46×10^{7}	2.34×10^{5}
Reverse intersystem crossing rate (s^{-1})	8×10^{5}	8.3×10^{5}
Generation efficiency – singlet	0.25	0.25
Generation efficiency – triplet	0.75	0.75

Table 4.6: Excitonic parameter extracted from TrPL fitting (20% and 50%).

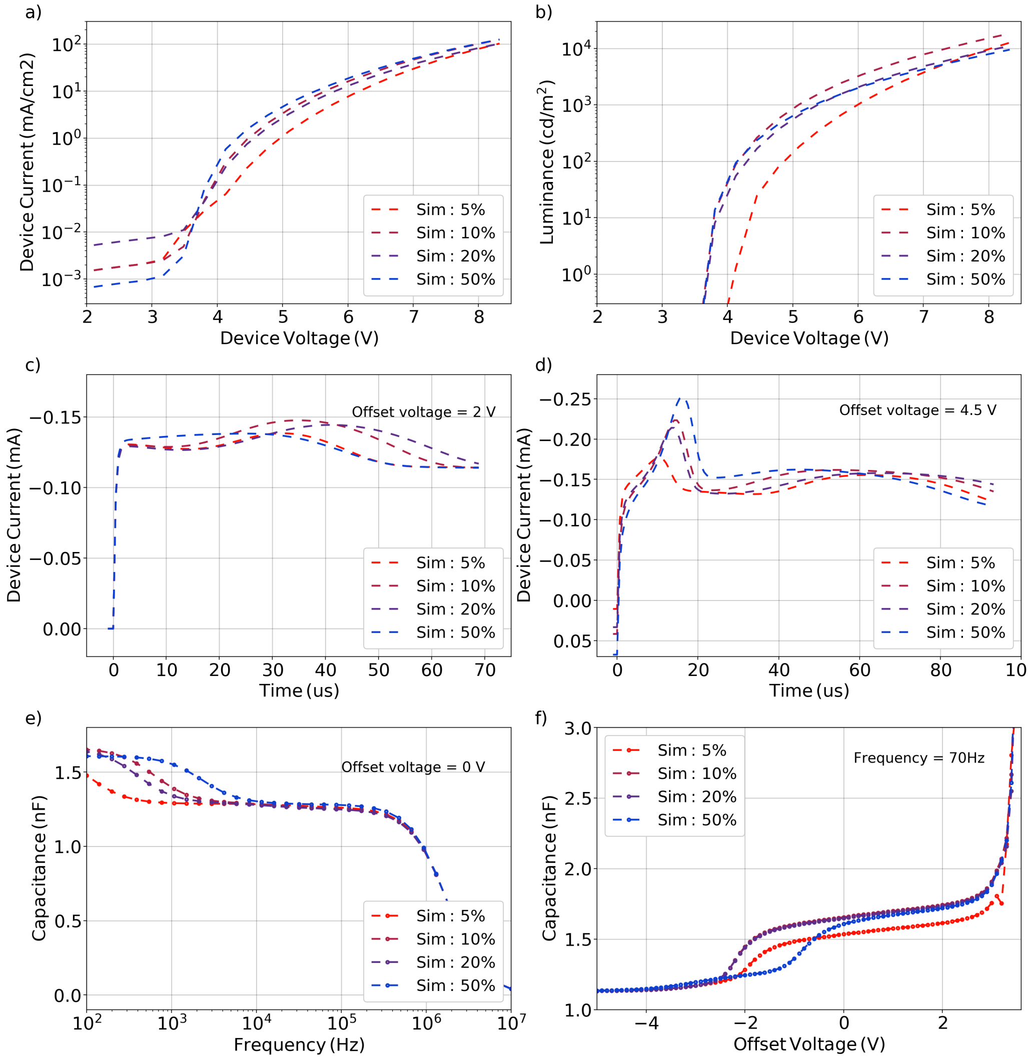

Figure 4.4: Simulation results of each device: (a) JV; (b) Luminance vs voltage; (c) injection-CELIV with V_{offset} = 2 V; (d) injection-CELIV with V_{offset} = 4.5 V; (e) C-f with V_{offset} = 0 V; (f) C-V with frequency = 70 Hz.

4.4.4 *Transient photoluminescence fit*

The fit of the TrPL curves is shown in Figure 4.5. The experiments were performed by Dr. Markus Schmid at Augsburg University. To estimate the excitonic parameters of the TADF EMLs, the transient photoluminescence experiments (TrPL) was performed. The camera used in the experiment is 4Picos (Stanford Computer Optics) with a Chromex 250 IS spectrograph. The laser is a Nitrogen Laser LTB MNL 200 (wavelength 337 nm, pulse duration 700 ps, repetition rate 20 Hz). The experimental data were subsequently fitted with the method described by N. Haase *et al.*[106] I can observe that the extracted values, indicated in the main paper in Table 4.5 and Table 4.6, are rather similar between the different samples. The similarity of these rates indicates very similar intrinsic emissive properties of the devices with different emitter concentration. Only the different recombination profiles and/or quenching processes (discussed below) lead to the noticeable differences in EQE. This again demonstrates the importance of considering electronic charge parameters to really optimize the OLED for a specific emitter.

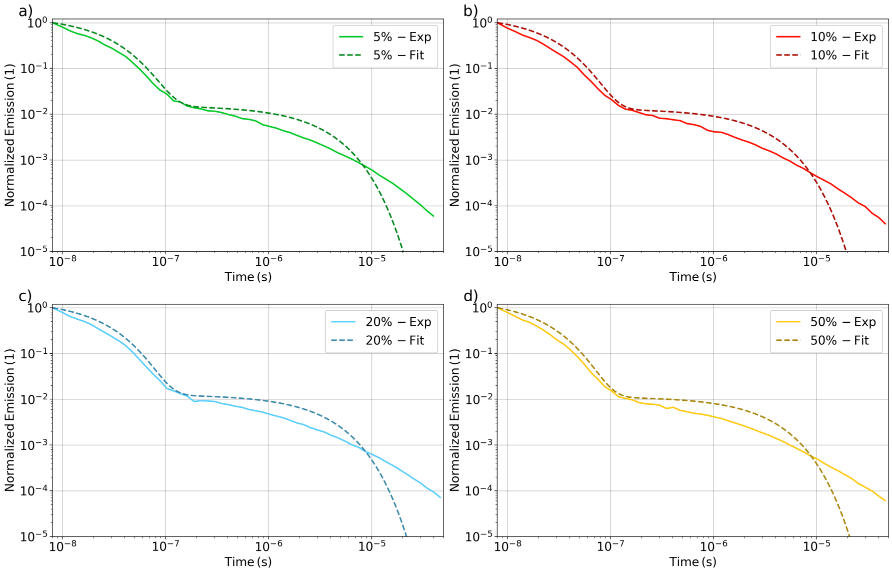

Figure 4.5: Transient PL experimental data and corresponding fit. Experimental results obtained by Markus Schmid at Augsburg University.

4.4.5 *Effect of polarity and focus on 50%*

Assuming TPBi to be the only polar layer [146], with simulations I obtain a good agreement for all the experiments for 5-10-20% devices. A sheet charge density of 2.64 mC/m^2 is extracted (positive charge at the TPBi/Al and negative at the DPEPO/TPBi). Having a polar layer inside the stack influences the entire electrical characteristic of the OLED, but the clearest evidence is visible in C-V, C-f and injection-CELIV. In C-V there is a negative V_t, in C-f (V_{offset} = 2 V) an increase of capacitance is visible at low frequency and in injection-CELIV (V_{offset} = 2 V) a clear peak is present, indicating the extraction of accumulated charges. In Figure 4.4 I can observe that all the three results are well reproduced by simulations. Further simulation results are indicated in the next section, where the charge profile is analysed at different voltage, clearly showing that the accumulation of holes occurs mainly at the TCTA/EML and EML/DPEPO interface. In the device with 50% guest concentration there are three main differences with respect to the other devices: in JV there is a slightly lower current turn-on, in capacitance-voltage V_t is shifted from -2 to -1 V and in injection-CELIV with V_{offset} = 2 V the rise attributed to hole accumulation starts at 0 µs (as soon as the linear reversed ramp is applied). All these experimental results indicate a different polarity effect in this device, and as the only difference to the other devices is the EML, the initial approximation supposing a non-polar EML does not hold anymore. Since both the host (mCBP-CN) and the guest molecules (DMAC-TRZ) possess a permanent dipole moment, it is challenging to understand the role of increasing guest concentration. One could assume that in 5%-10%-20% devices the EML possess a certain polarity which is reduced when increasing guest concentration to 50%. In my case, having assumed 5%-10%-20% to have a non-polar EML, I suppose the EML with 50% to be polar and the best agreement with the experimental results is obtained with a sheet charge density of -0.7 mC/m² (opposite direction with respect to TPBi). From Figure 4.6, the comparison of the experimental results and simulations considering a polar and non-polar EML for device 50% is shown. Clearly, this additional complexity in the model is required to explain the various measurements.

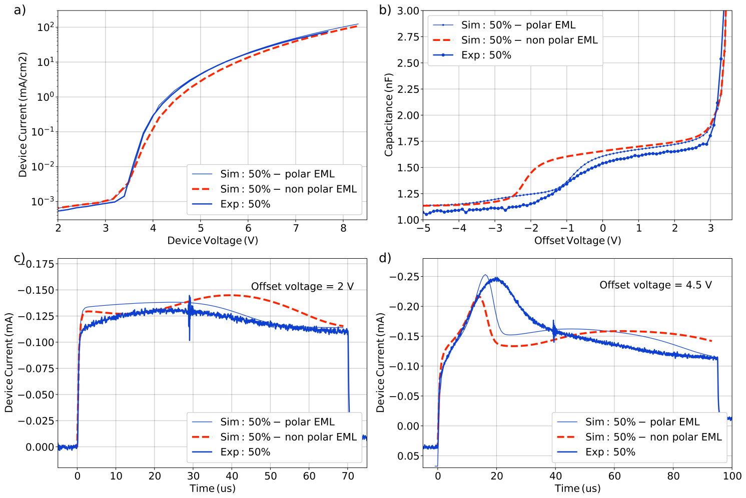

Figure 4.6: Experimental and simulated results of device with 50% guest concentration considering the EML polar and non-polar. (a) JV; (b) C-V with frequency = 70 Hz; (c) injection-CELIV with V_{offset} = 2 V; (d) injection-CELIV with V_{offset} = 4.5 V).

4.4.6 *Charge accumulation*

The effect of having a polar TPBi layer has been already discussed so far. An injection of holes from the ITO contact well below turn-on has been found to strongly affect the device operation. Indication of the early injected holes was inferable from several experiments, C-V, C-f and injection CELIV. In Figure 4.7 I can observe the simulated holes and electron distribution inside the stack at various voltage. At 0 V the hole distribution in the EML is already high while the electron density is basically null below 3 V.

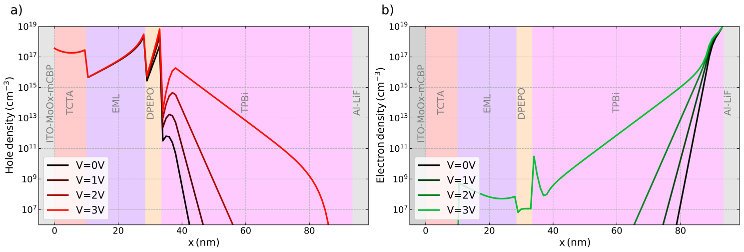

Figure 4.7: Simulated charge density profile at different voltage (0-1-2-3V). (a) hole density and (b) electron density.

4.4.7 *Analysis of efficiency roll-off*

The efficiency roll-off is the result of an interaction of many processes: triplet-triplet annihilation (TTA), singlet-triplet annihilation (STA), singlet-singlet annihilation (SSA), triplet-polaron quenching with electrons (TPQ-n), triplet-polaron quenching with holes (TPQ-p), singlet-polaron quenching with electrons (SPQ-n) and singlet-polaron quenching with holes (SPQ-q)[147]. In TADF emitters the population of triplets is usually larger than the population of singlets and this causes density-dependent annihilation processes involving triplets (TTA, TPQ-n and TPQ-p) to be the most critical processes influencing the efficiency roll-off.[148, 149] For this reason I will include only them in the model. In some cases also SPQ has been found to play an important role, however I assume it to be absent in this study. Estimating those rates from a roll-off curve has been done in several studies,[148, 150] but I are aware that being able to distinguish those rates from a simple roll-off curve can be challenging. Nevertheless, I performed a fit of the luminance efficiency for all the devices, leaving the three parameters free for each device. In this way, for each device, a set of three parameters is extracted (TTA, TPQ-n and TPQ-p rates). The resulting fit is shown in Figure 4.8a. At high currents, the fit well replicates all the experimental results, while for low currents the 5% simulation shows a lower efficiency. The reason could be that I modelled the 5% device such that transport in the EML occurs purely on the host molecules. It might be that a small amount of charge can be injected directly on the guest molecules even with only 5% concentration. In this case, the energy barrier between ETL and EML is reduced, and the emission starts at lower voltage. In Figure 4.8b the correlation matrix of the resulting fit is shown for the 10% device. The correlation is relatively high especially for TTA and TPQ-n ($\rho_{TTA-TPQ-n}(10\%) = 0.92$). This result is an indication that it is rather difficult to distinguish the two effects separately, which makes the specific extracted numbers not extremely solid. TPQ-p shows instead an acceptable correlation with the other two effects. The reason is that I found the TPQ-p to have a greater impact on the luminance efficiency curve at lower currents while TTA and TPQ-n rates affect the curves at higher currents. This effect is totally in line with what I described above, the polarity of TPBi induces an injection of holes already below turn-on voltage and the high density of holes already at low voltage causes the TPQ-p to be the prevalent loss mechanism at low currents. This effect can be easily identified using the exciton losses plot, which is a direct output from Setfos 5.2. In Figure 4.8c the different contributions to triplet losses for the 10% concentration device is shown. At low currents,the dominant loss is coming from TPQ-p while at higher currents TTA and TPQ-n give a much larger contribution. The plot in Figure 4.8d displays the extracted values of TTA, TPQ-n and TPQ-p for the four devices. I can observe that all the three rates are increasing with concentration. In particular, I find an empirical logarithmic relation with the concentration for concentration higher than 5%. Equation 4.1 was used to produce the fit in Figure 4.8d. Table 4.7 provides the resulting c_1 and c_2 values.

$$f(x) = c_1 \ln (c_2 x) \tag{4.1}$$

The dependence of the TTA rate with concentration has already been investigated by Ligthart *et al.*[151] and Zhang et al[152]. In both studies, they show that an increase in guest concentration produces a larger TTA rate. This happens because, at higher guest concentrations, the average distance between guest molecules decreases, and the annihilation event is facilitated. In the case of TPQ instead, a direct relation between guest concentration and TPQ rate has not been found in the literature. An alternative possibility would be to maintain the TPQ rates concentration-independent in the fitting procedure. However, I believe that in such a case, where no direct information from literature can be found, leaving the three parameters (TTA, TPQ-n and TPQ-p) completely free to be optimized for each device is a good approach. I would like to comment on the correlation between TTA and TPQ-n. As previously described, the effect of TTA and TPQ-n on the efficiency roll-off is very difficult to distinguish. Additional and more sophisticated experimental techniques have been performed, as described by Wehrmeister *et al.*[121] In this study these two processes are investigated by combining transient PL with electroluminescence. However, this type of analysis goes beyond the scope of this study.

4.5 CONCLUSIONS

In this study I have shown that charge transport in host-guest TADF emitter layers can electrically be modelled within two distinct regimes depending on the concentration of the TADF guest molecules (high

	c_1 (cm^3s^{-1})	c_2
TTA	1.8×10^{-13}	9.31
TPQ-n	1.6×10^{-12}	1.33
TPQ-p	1.5×10^{-14}	0.14

Table 4.7: Extracted coefficient of Equation 4.1; the fit is shown in Figure 4.8d.

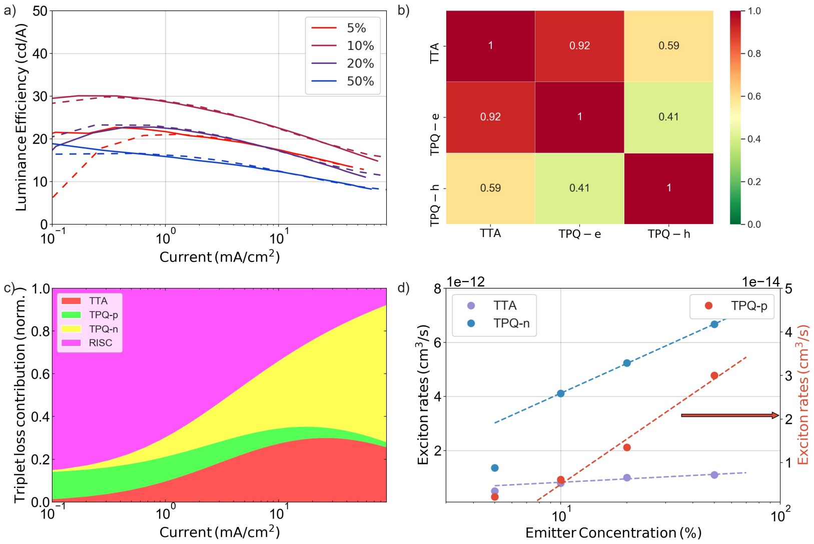

Figure 4.8: The efficiency roll-off is analysed. (a) Experimental data (solid line) and fit (dashed line) of the luminance efficiency roll-off for all the devices; (b) correlation matrix of the luminance efficiency roll-off fit shown in (a) for device 10%; (c) plot of the triplet exciton losses contribution of device 10%, direct output of Setfos; (d) The extracted TTA, TPQ-n and TPQ-p are plotted vs guest concentration of the EML in a log-lin scale; the dashed line indicates the fitting performed with Equation 4.1. The fitted coefficient c_1 and c_2 are indicated in Table 4.7.

and low guest concentration regimes). This approach allows us to explain the presence of transient EL decay overshoot in the device with 5% DMAC-TRZ guest concentration. For all the devices I found signs of a polar ETL in several experiments: injection-CELIV, capacitance-voltage and capacitance-frequency. I could replicate all these signatures of the polar ETL with simulations, allowing for the extraction of the specific sheet charge density inherent to spontaneous orientation polarization (SOP) inside the ETL. Regarding the device with 50% DMAC-TRZ concentration I observed a different polarity of the EML, which was quantified as well. By analysing the luminance efficiency roll-off I extracted the TTA, TPQ-n and TPQ-p rates which appear to be logarithmically dependent of the DMAC-TRZ molecule concentration in the EML. Additionally, TPQ-p appears to be the limiting factor of the luminance efficiency at low currents while TTA and TPQ-n are responsible for the luminance efficiency roll-off at high currents. Thanks to this comprehensive characterization I can link the strong influence of TPQ-p on the efficiency at low current with the polarity of the ETL. The strong polarity of TPBi induces a high density of holes in the EML at low voltage and, since TPQ-p depends on the hole density, this causes the effect of TPQ-p on the efficiency to be non-negligible even at low current/voltage. This comprehensive study which includes electronic, excitonic and optical aspects, provides a basis for upcoming work on simulation based guest concentration optimization in a complete OLED device.

5

ESTIMATING THE OLED LIFETIME IN DIFFERENT STRESSING CONDITIONS

A new OLED technology can possess wonderful properties in terms of efficiency, emitted wavelength or angle, but it will never reach the market if it is not stable enough. In this study I face the problem of estimating the OLED lifetime in different conditions of temperature and driving current. This approach is applicable in any emissive device, OLED or LED, and in this thesis it has been tested on TADF OLEDs.

5.1 INTRODUCTION

OLED displays are already commercialized in several products. As introduced in previous chapters, one of the main challenge faced by scientists is analyzing the stability of these devices. The operational lifetime requested for commercial application is in the range of thousands of hours.

Testing these characteristics is of course challenging since, considering a typical lifetime of 50000 hours, the test would require almost six years at standard operating conditions (SOC). It is therefore required to perform these tests under more stressful conditions. The typical way to fasten the degradation consists of applying high current (larger than driving current during operation) and high temperature. This type of analysis is called accelerated lifetime testing (ALT). Once the lifetime under these conditions is found, proper scaling lows allow to estimate it at SOC.[153–156] The key figure of merit in this analysis is LT70, which is defined as the amount of time after which the luminance has reached 70% of its initial value.

In this study I follow the analysis performed by Yoshioka *et al.*[157], where multiple stressing conditions are applied on nominally identical OLEDs. The same approach is used in this study, with the difference that I defined a global fitting algorithm to extract the model parameters. In the first part of the study I focus on the extraction of the model parameters, taking into account the entire sets of data. This approach allows to estimate LT70 in any current-temperature condition. In the second part I took into account only a subset of data, so that LT70 can be effectively estimated in accelerated conditions.

For this study, the platform *Litos* is used to apply the specific stressing conditions and record the luminance decay over time.

5.2 DEVICE FABRICATION

The samples have been fabricated at Merck KGaA. The device structure includes an ITO substrate topped off with an HIL. The organic layers are: 60 nm N,N′-Di(1-naphthyl)-N,N′-diphenyl-(1,1′-biphenyl)-4,4′-diamine (NPB), 20 nm 9,9′-Diphenyl-9H,9′H-3,3′-bicarbazole (BCzPh), the EML, 30 nm 2,4,6-tris(biphenyl-3-yl)-1,3,5-triazine (T2T). The cathod consist of a thin EIL and aluminum on top. The EML consist of 30 nm of DMAC-TRZ, mCBP-CN and BCzPh, mixed at a concentration of 10 wt%, 50 wt% and 40 wt%. The stack is shown in Figure 5.1.

The luminance decay over time follows a bi-exponential function. The first, and very fast, exponential decay occurs usually in the first few minutes of operation, and it is usually referred to as burn-in. The devices used in this study have been subjected to a high current for a few seconds right after fabrication, so that the burn-in decay has already occurred. The luminance decay seen in the experiments is therefore a single stretched exponential decay.

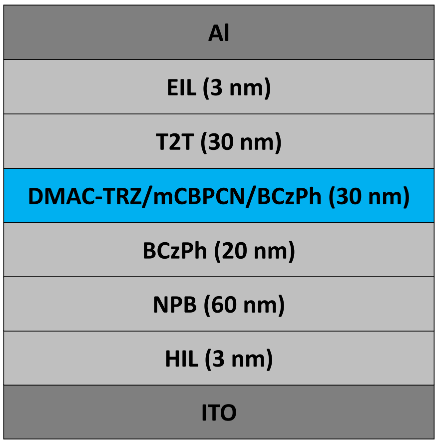

Figure 5.1: Structure of the devices studied in Chapter 5 and Chapter 6. The EML consists of a TADF emitter (DMAC-TRZ) embedded in a co-host matrix.

5.3 STRESSING CONDITIONS

Three nominally identical samples are used in this study, with four pixels each. In total twelve pixels have been stressed. The three devices are placed in three of the four chambers available in *Litos*. In each chamber the temperature is kept constant, at: 283, 298 and 313 K. In each chamber, the four pixels are stressed with four constant current densities: 5, 10, 20 and 30 mA/cm^2. In Figure 5.2 a schematic of the stressing conditions is shown. During stressing, two main quantities are measured for each pixel: the applied voltage and the emission intensity. For the ALT analysis, only the latter is further analyzed.

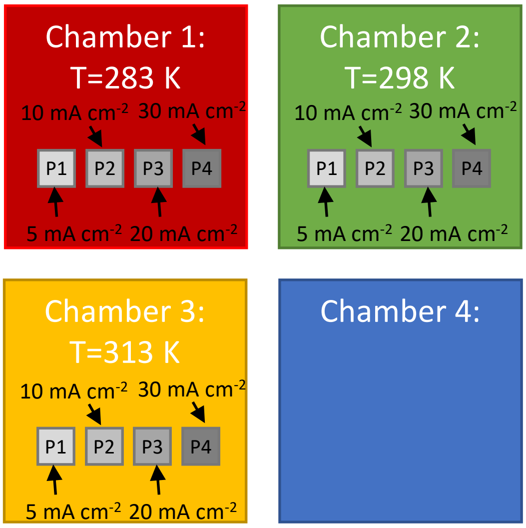

Figure 5.2: Schematics of stress the conditions in *Litos*chambers.

5.4 SCALING LAW AND GLOBAL FIT

To analyze the experimental results, I need first to understand the mathematical description of the luminance decay during operation under constant current.

The ALT method, which is known for inorganic LEDs, has been presented and refined for OLEDs by Yoshioka *et al.* [156]. In their study they found an empirical relation between the decay time constant and the stressing condition applied (current density and temperature):

$$L = L(0)e^{-(\frac{t}{\tau})^{\beta}} \tag{5.1}$$

$$\tau = AJ^{-\gamma}e^{\frac{E_a}{k_b T}} \tag{5.2}$$

where J, T and $L(0)$ are pixel specific current density, temperature and initial luminance; while β, A, γ and E_a are global model paramters; k_b is the Boltzmann constant. My analysis follows the study carried out by Yoshioka *et al.*, with the difference that I applied the concept of global fitting. Instead of fitting each decay curve individually, I fit all the twelve curves at the same time, extracting a single set of parameters. This method is beneficial since it allows to reduce the correlation between the extracted parameters. The schematic of the algorithm inputs and outputs is shown in Figure 5.3. The algorithm has been implemented in Python, using the scipy package, and is similar to the one described in Chapter 3.

A few points of clarification are necessary. First, I shall state that the luminance is measured at the current density of the specific stressing condition, this means that the larger the stressing current, the larger the measured light intensity, which might not be apparent at first sight when looking at the auto-scaled plots in Figure 5.4. As a second point, I can note that this is not always true, in the chamber with T = 283 K the intensity of the 20 mA/cm² is larger than the one with 30 mA/cm². This is due to the positioning of the photodiode. In each chamber there are four photodiodes but they are not precisely located below the pixels. However, this fact does not represent a problem because the first point of each experimental curve ($L(0)$) is taken as a known parameter of the fit. Another detail worth mentioning is weighting of the error of each curve. The core of the algorithm is a function which minimizes the error between the fit and the experimental curve. When multiple curves with different intensity, as in this case, are taken into account, the fit will automatically tend to be more precise when the intensity is larger (or the curve contains more points). To solve this issue, the concept of weights is introduced. The error associated to each curve is multiplied by a factor (the weight) calculated accordingly to the number of points and the intensity of each curve. In this way the fit is optimized.

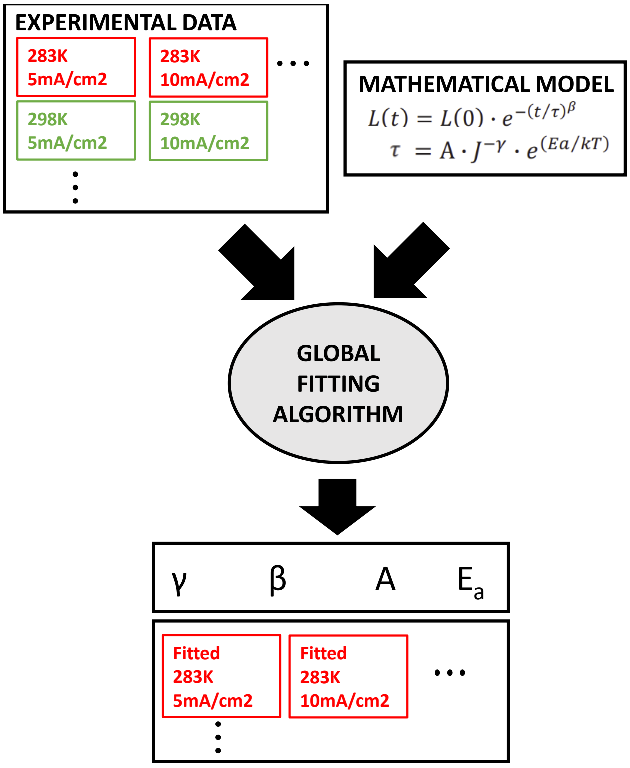

Figure 5.3: Schematics of the global fitting algorithm applied to the experimental results described in this chapter.

5.5 EXTRACTION OF THE MODEL PARAMETERS

The experimental luminance decay curves of all twelve pixels are shown in Figure 5.4 in black. The respective temperature and current density is provided in the insets. The extracted parameters are shown in Table 5.1. The current scaling factor γ and the stretching factor β are very similar to previous reports on phosphorescent OLEDs.[156–158] The value for the activation energy is about a factor of two smaller than in the previous reports, yet it is within a reasonable range that could potentially be linked to some internal barrier that is overcome at elevated temperature. The only parameter that could be linked to some underlying physical degradation phenomena is the current acceleration factor, γ. A value close to one indicates significant generation of luminescence quenching sites due to polarons, whereas values closer to two would be attributed to bi-molecular effects such as exciton-exciton, exciton-polaron quenching events.[159]

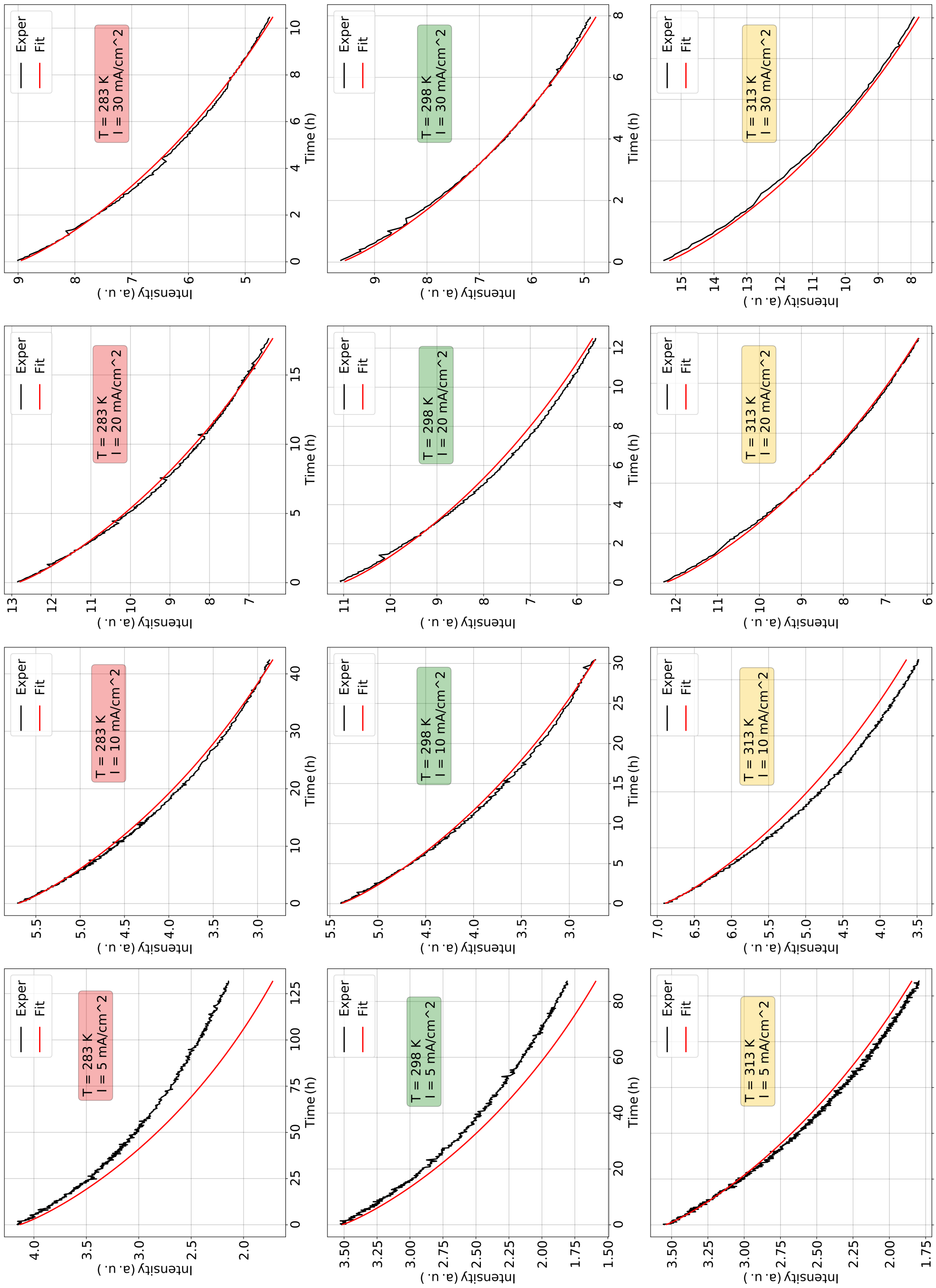

Figure 5.4: Experimental luminance decay during stressing and fit with different stressing conditions.

In the analysis discussed so far the luminance decay until the point in time at which the luminance has dropped 50% (LT50) has been taken into account. With this method I do not perform an accelerate stressing, since I apply currents which are in some cases lower than at SOC. However, this approach provides the scaling parameters which allows to perform a good estimation of the luminance decay at any current-temperature condition.

Parameter	Value
γ	1.25
β	0.85
A	3.35
E_a	142 meV

Table 5.1: Parameters extracted from the fit shown in Figure 5.4.

5.6 ACCELERATED LIFETIME TESTING (ALT)

The predictive power at SOC is only exploited if a reduced data set is used. I defined the stressing performed with $J = 10\,mA/cm^2$ at 298 K as the SOC, and three methods are used to estimate LT70 at SOC. In the first approach, LT70 at SOC is predicted by using only a few sets of temperatures and currents (currents of 20 and $30\,mA/cm^2$, at all the temperatures), not including the one at SOC. As I only take some devices into account for this analysis, I called it "reduced devices" (RD). In a second approach, LT70 is predicted using only the initial part of the luminance decay data. For clarity of exposition, I define the initial part of the decay, the one taken into account in the fit, as training set, while the second as test set. The limit between training and test sets are defined in term of percentage of decrease of the luminance from the initial point, and I call it training-test limit (TTL). This analysis has been done with three TTLs: 70%, 80% and 90%. In a third approach, the two methods are combined.

I evaluate the quality of lifetime predictions for all the approaches by calculating the difference between the measured and the fitted LT70 value. In addition, I include the saved measurement time (MT) to test the ALT method. The MT is calculated as the difference, in percentage, between the experimental LT70 at SOC and the maximum duration of the experiments taken into account in the fit.

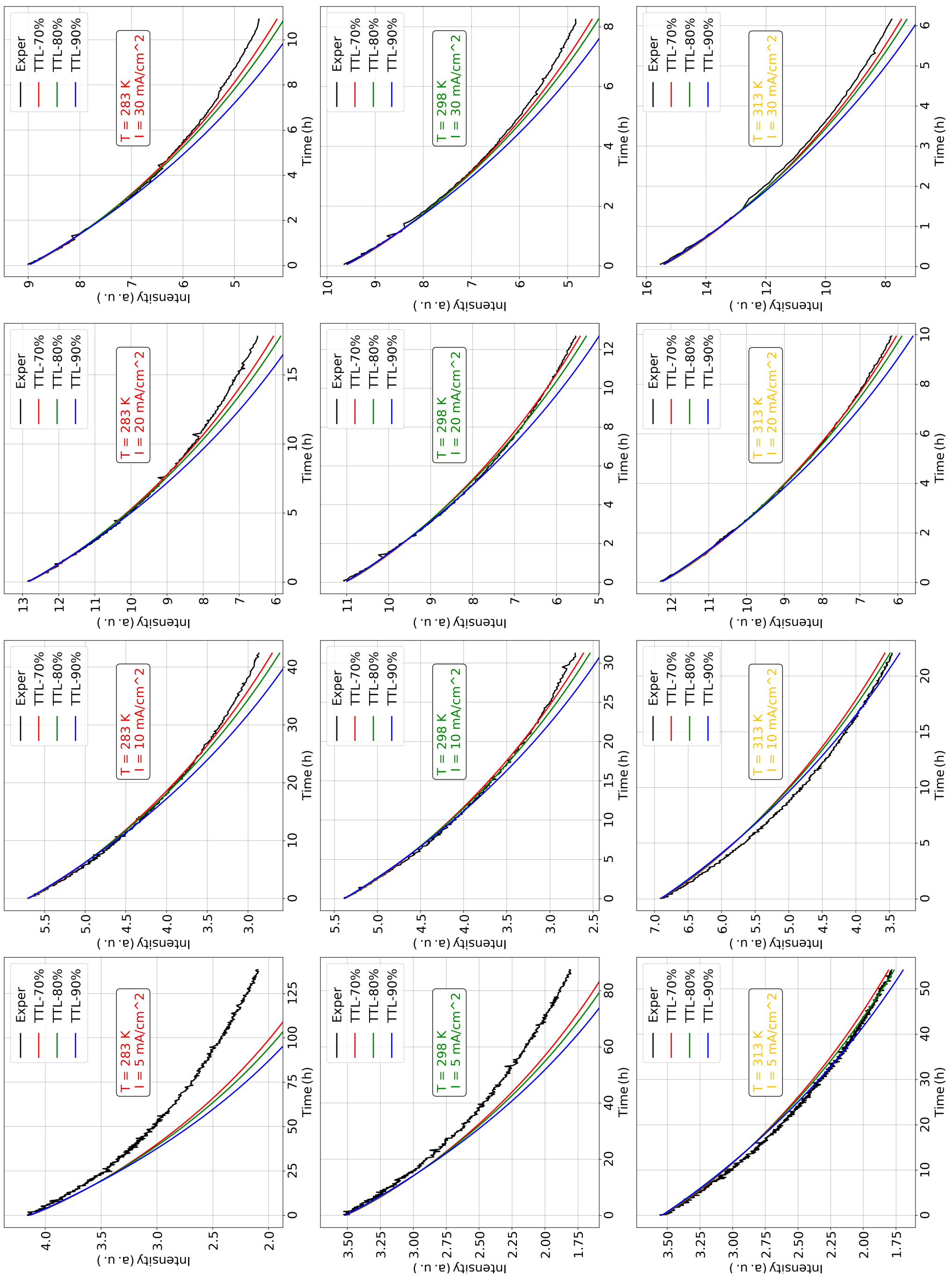

Figure 5.5: Experimental and fit luminance curves with the different TTLs approach. TTLs of 70%, 80% and 90% were used.

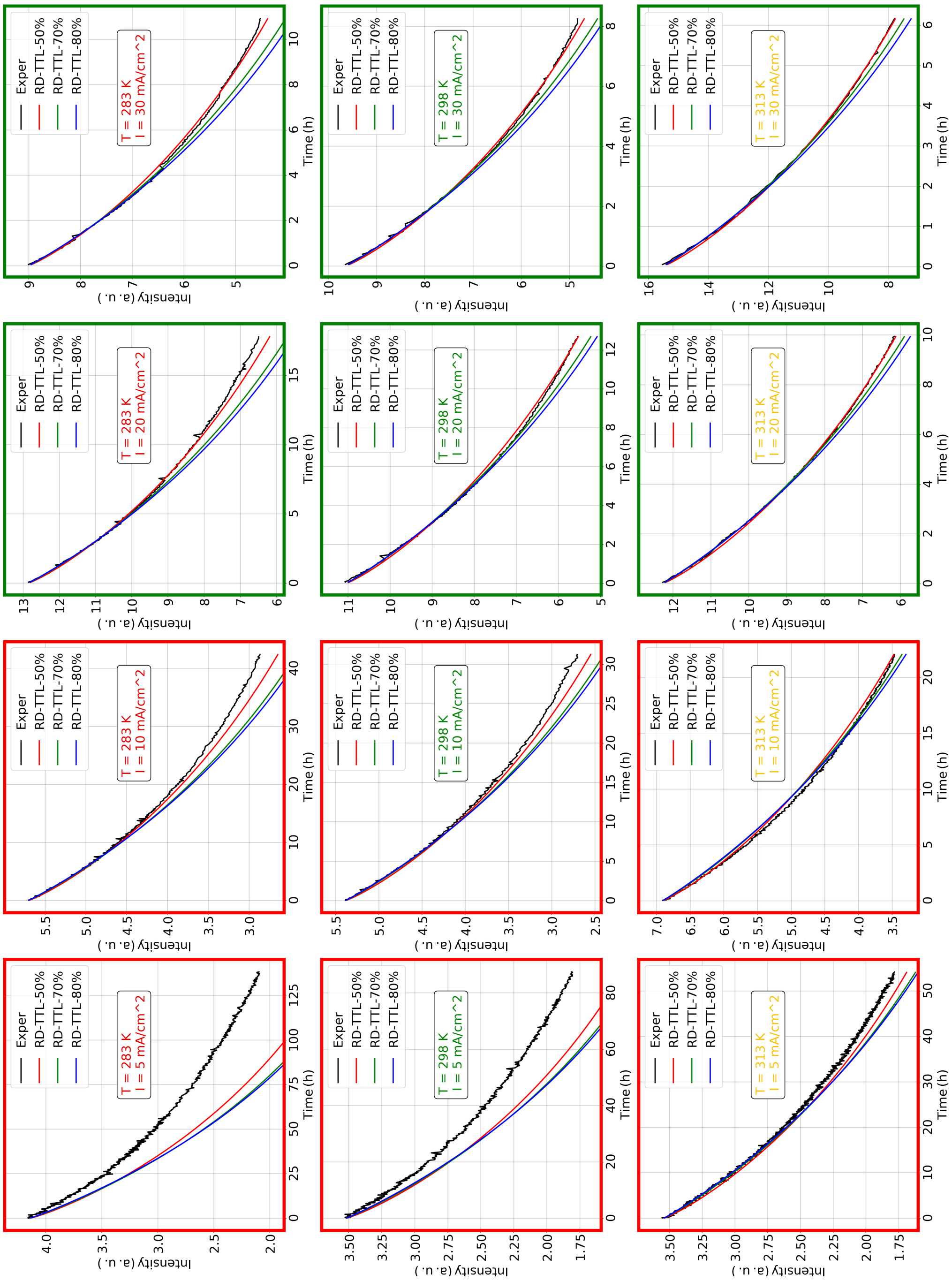

Figure 5.6: Experimental and fit luminance curves with the RD and different TTLs approaches. TTLs of 50%, 70% and 80% were used.

Data used for the fit	Fitted LT70 (h)	Error (%)	Meas. Time (h)	Time gain (%)
All data	14.4	4.4	138.5	-903
RD	13.3	-3.6	17.8	-29
TTL-70	14.2	2.9	58	-321
TTL-80	14.0	1.5	33.4	-142
TTL-90	13.4	-2.9	14	-1.5
RD + TTL-70	12.9	-6.6	7.7	44
RD + TTL-80	12.8	-7.3	4.5	67

Table 5.2: Fitted LT70 value for the device stressed at $J = 10\,\mathrm{mA/cm^2}$ and $T = 298\,\mathrm{K}$ using different sets of fitting curves. Measured LT70 of this device is 13.8 h.

Data used for the fit	β	γ	E_a (meV)	A
All data	0.85	1.26	143	3.3
RD	0.88	1.17	134	3.5
TTL-70	0.90	1.26	132	4.9
TTL-80	0.93	1.26	129	5.0
TTL-90	0.97	1.27	124	5.7
RD + TTL-70	0.93	1.17	120	5.5
RD + TTL-80	0.95	1.19	119	5.7

Table 5.3: β, γ, E_a and A parameters extracted from the fittings.

In Figure 5.5 the fit with different TTLs is shown, while in Figure 5.6 the fit with combined method (RD + TTL) is shown. The resulting estimation of LT70 and the ML of the SOC is summarized in Table 5.2. The error in the estimation of LT70 is rather small for all the methods. The RD + TTL80 approach is of course the one with the largest time gain (67%), since the measurement can be done in only 4.5 hours. Even in this case the error LT70 error is below below 8%.

The extracted sets of parameters are reported in Table 5.3. It can be observed that the variation of the parameters is rather small for all the methods. The largest variation is observed in the parameter A, which spans from 3.3, when all the data are used, to 5.7, when the RD+TTL80 method is considered. All the other parameters vary much less: β from 0.85 to 0.95; γ from 1.17 to 1.26; E_a from 119 to 143 meV. Such a small variation is firstly an indication that all the methods can be applied without loosing precision in the final results, additionally, is an indication that the fitting algorithm is stable.

5.7 CONCLUSIONS

In summary, I demonstrated the use of accelerated testing methods and the determination of scaling parameters for TADF OLEDs. The lifetime is predicted with an error of less than 8% when target data is reduced by including less devices or by fitting only the initial luminance decay. By combining both methods, up to 67% of the stress test time can be saved. The extracted parameters change only slightly when using different approaches. This fact confirms that the fitting algorithm is stable since a change in the inputs does not produce a dramatic variation of the extracted parameters.

6

EVIDENCE FOR GENERATION OF TRAP STATES DURING DEGRADATION OF TADF OLEDS

The method described in the previous chapter can certainly provide a good estimation of the device lifetime in different conditions, but no additional information about the underlying degradation mechanisms can be extracted. To really improve the lifetime of a specific OLED structure, a detailed understanding of the phenomena causing the luminance reduction is necessary. This knowledge can only be acquired by using advanced characterization techniques during device stressing.

In this chapter I applied this method to the same TADF OLEDs studied in Chapter 5. Steady-state, impedance and transient measurements are used to characterize these devices during stressing interruptions.

Additionally, electrical device simulations are used to qualitatively understand the main physical processes occurring during degradation.

6.1 INTRODUCTION

With *Litos* there is the possibility to run basic experiments during stressing, like JV measurements. Since in this case I have the possibility to combine it with *Paios*, the full characterization with all the experimental techniques described in Chapter 2 is performed.

The devices measured in this chapter are stressed with a current density of $10\,\mathrm{mA/cm^2}$ at a temperature of $283\,\mathrm{K}$. All the experiments shown in Section 6.5 and Section 6.4 are done on the same device, stressed until ≈LT60 apart from Figure 6.7 and Figure 6.8, which where done at ≈LT90. For completeness, I must note that, in this type of analysis, the reproducibility of the experimental results on several samples is fundamental in order to be able to draw meaningful conclusions. For this reason, several identical pixels were stressed at the same conditions and it was found that indeed the experimental results are identical. The stack is the same as the one studied in Chapter 5, and is shown again here in Figure 6.1.

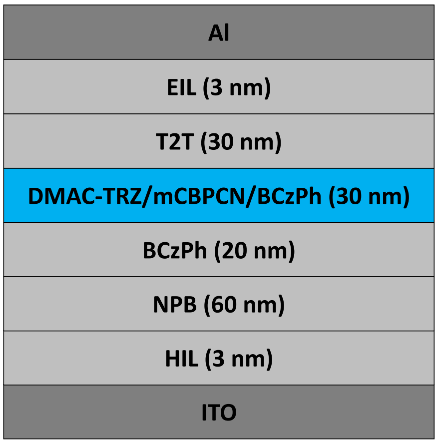

Figure 6.1: Structure of the devices studied in Chapter 5 and Chapter 6. The EML consists of a TADF emitter (DMAC-TRZ) embedded in a co-host matrix.

6.2 EXPERIMENTAL RESULTS DURING STRESS INTERRUPTIONS

The experimental results are shown in Figure 6.2. In Figure 6.2a the JV is shown and, as expected, there is a reduction of the current during degradation.

In Figure 6.2b the capacitance-voltage results are shown. A clear shift of the threshold voltage, V_{th}, can be observed, first towards lower voltage (in the initial 6/7 hours) and later to higher voltage. Below 0.7 V the geometric capacitance of 20 nF/cm^2 is reached and obviously does not change during degradation.

From the C-f plot, shown in Figure 6.2c, two main features can be observed: besides the strong reduction of the capacitance peak at low frequency, there is a continuous reduction of the first capacitance plateau, from 40 nF/cm^2 to roughly 25 nF/cm^2. The second effect is the variation of the transition frequency (from the first plateau to the geometric capacitance, at 25 nF/cm^2), which shifts from 10^5 Hz to 10^4 Hz. These two effects could indicate the presence of two separate processes occurring during degradation. This fact might also be linked to the shift of V_{th} in two directions seen in Figure 6.2b.

Figure 6.2d shows the injection CELIV experimental results. It is observed that there is a systematic decrease of the current peak during stressing, which might be an indication of a reduction of accumulated charge at some interfaces. However, it must be taken into account that at 2.5 V the current decreases during stressing, as visible in the JV plot. Clearly, a reduced current should reflect in a smaller amount of accumulated charge. Additionally, the current peak does not shift in time during degradation. This fact suggests that there is no visible modification of the charge carrier mobility in the organic layer/s up to which the charge accumulates.

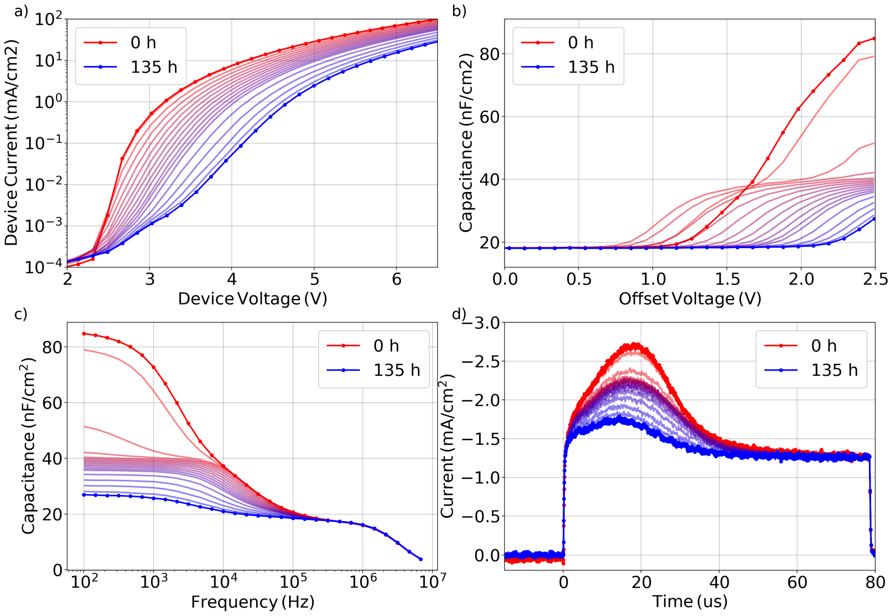

Figure 6.2: Experimental results during stressing interruptions. Stressing performed with 10 mA/cm² at a temperature of 283 K. (a) JV; (b) C-V with frequency = 100 Hz; (c) C-f with V_{offset} = 2.5 V; (d) injection-CELIV with V_{offset} = 2.5 V, V_{end} = -3 V and ramp-rate = 0.07 V/µs.

Despite the several interesting features observed, I specifically investigated the C-V experiments. Besides the clear reduction of the capacitance peak located at 2.5 V, which is probably related to a change/reduction of the accumulation of charges, the most interesting effect is the shift of V_{th}. In Figure 6.3 the C-V measurement during degradation can be seen in detail. In the first 7 hours, V_{th} shifts to lower voltage, while afterwards it shifts to higher voltage. In the following sections additional experiments and simulations are used to further investigate this effect.

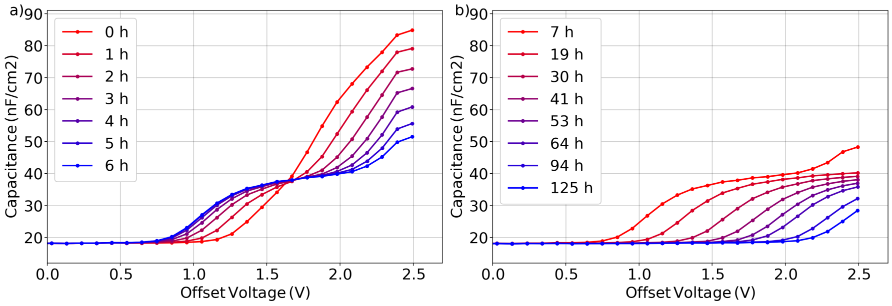

Figure 6.3: Experimental results of C-V with frequency = 100 Hz during stressing interruptions. (a) shift of V_{th} to lower voltage occurring in the first 7 hours; (b) shift of V_{th} to higher voltage.

6.3 IMPEDANCE SIMULATIONS - SHIFT OF V_{TH}

In C-V measurements, the presence of a V_{th} below V_{bi}, has been previously attributed to the presence of a polar layer inside the stack. In case of a polar layer, the alignment of charged molecules creates a permanent electric field inside the layer, which causes the injection of charges even below V_{bi}. This effect can be replicated with *Setfos*, as shown in this thesis in Section 4.4.5 or by Altazin *et al.*[96] In the C-V curve of the fresh device shown in Figure 6.3, the capacitance increase at $\approx 1.7\,\text{V}$ might be an indication that one or more layers are polar. Several materials contained in the stack could be responsible for the polarity, i. e. mCBP-CN, DMAC-TRZ and BCzPh.

Having one or more polar layers inside the stack explains the presence of V_{th} below V_{bi} well, but not its shifts. The shift to lower and then higher voltage could be interpreted with an initial increase and then decrease of the polarity. However, this explanation can not easily be established, and has never been described in literature.

A physical effect that is commonly happening during degradation is the creation of trap states. A trap state is a defect, which is typically generated by an exciton-exciton or exciton-polaron annihilation event, in which charges can get trapped.[160–162] Having a layer, or an interface, with filled trap states resembles well with the situation of a polar layer, but with only one charged interface. With *Setfos* I can model this situation by simply including trap states in the model, and I can simulate a C-V experiment in steady-state conditions. However, it must be observed that the layer/interface ends up being charged only when trap states are filled. In a steady-state C-V simulation, charges are heavily injected only when the turn-on voltage is reached. To better model the C-V experiment at stressing interruptions, I performed transient-impedance simulations. In this case, an initial steady-state forward voltage is applied, during which charges are injected (and eventually captured by trap states), followed by a simulation of the C-V scan.

The first simulation I have done to see the impact of filling the trap states, is a transient-impedance simulation on a forward-backward ramp. The applied voltage has a triangular shape, starting from -1 V, reaching 5 V and ending again at -1 V (ramp rate = +/-0.33 V/s). The simulated device is simplified with respect to the real one used in the stressing and is composed only of an HTL and an ETL. Traps are included in the model only in a small portion of the ETL, in which only electron trap states are defined (see Figure 6.4-inset).

The result is shown in Figure 6.4. During the forward ramp, no charges have been previously injected into the device and therefore the trap states are empty. In this condition there is no charged interface and the simulation shows a threshold voltage of 2.5 V. During the backward ramp instead, having filled trap states causes V_{th} to be shifted down to 0.7 V.

This result indicates that, when evaluating the C-V of a device where deep trap states are defined, a simple C-V simulated in steady-state can not precisely replicate the effect of having filled trap states. A transient impedance-simulation is in this case necessary.

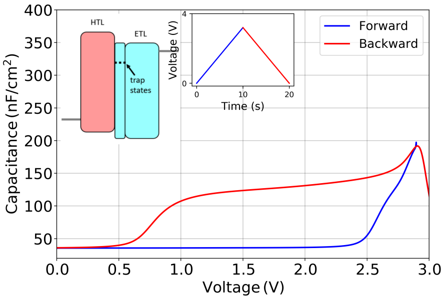

Figure 6.4: Transient-impedance simulation. The applied voltage is a forward and backward ramp, indicated in the inset. The simulation is done on a simple bi-layer stack, where electron-trap states are defined in a portion of the ETL layer.

In all the C-V simulations contained in the rest of this chapter, the following transient voltage is considered:

- initial steady state at 5 V, to replicate the device condition during stressing
- -1 V for 2 ms, to take into account the waiting time of the instrument before the C-V scan starts
- voltage ramp during which the capacitance is simulated (ramp rate = 0.33 V/s)

As discussed in Section 2.3, traps in *Setfos* are modeled with three parameters: the trap density ($n_{\text{t-e}}$), the energetic trap depth ($E_{\text{t-e}}$) and the charge capture rate ($c_{\text{t-e}}$). In the previous example the three parameters are set to: 10^{19} cm^{-3}, 0.7 eV and 10^{-10} cm^3/s. Of course all the three have an impact on these simulations. The effect of a variation of $n_{\text{t-e}}$ is shown in Figure 6.5. V_{th} is strongly dependent on the trap density. The amount of trapped electrons at 2 ms, before the voltage ramp starts (Figure 6.5b), is responsible for the change of V_{th}. It can be observed that the trapped electrons remain to the level assumed during steady-state voltage of 5 V. Applying -1 V for 2 ms seems to cause almost no release of trapped electrons.

6.4 EXPERIMENTAL RESULTS-MULTIPLE REPETITION C-V

To examine in depth the shift of V_{th}, additional experiments are done. To start this investigation, three C-V measurements are performed

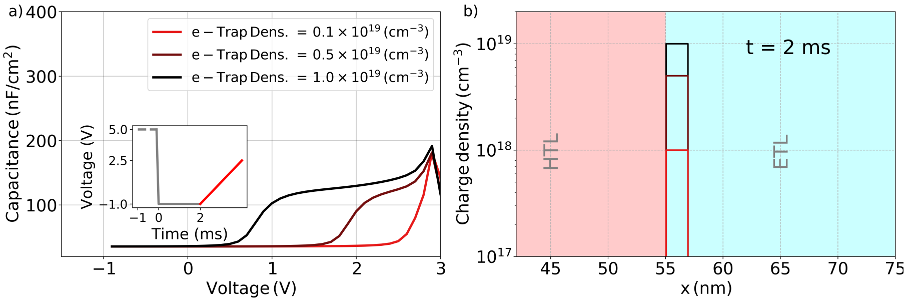

Figure 6.5: (a) Transient-impedance simulations with different $n_{\text{t-e}}$ of 0.1×10^{19}, 0.5×10^{19} and 1×10^{19} cm^{-3} ($E_{\text{t-e}}$ = 0.7 eV and $c_{\text{t-e}}$ = 10^{-10} cm^3/s); (a-inset) applied voltage sweep in forward direction (the ramp is not in scale); (b) Trapped electron distribution of the simulations shown in (a) at 2 ms.

with a different preconditioning (V$_{\text{prec}}$, constant voltage before the C-V scan): 5 V for 10 minutes, 4 V for 30 minutes, -5 V for 10 minutes. Additionally, each C-V scan is performed with two repetitions, one after the other (without a second preconditioning).

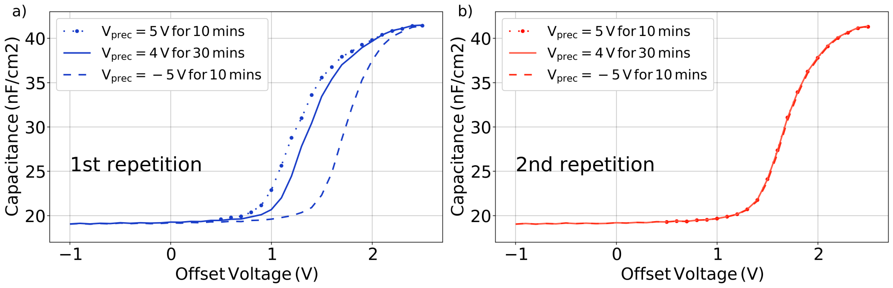

Figure 6.6: (a) First and (b) second repetition of a C-V scan done with a preconditioning of: 5 V, 4 V, and -1 V for 10, 30 and 10 minutes.

The result of the first repetition is shown in Figure 6.6a. It can be clearly observed that V$_{\text{th}}$ strongly depends on V$_{\text{prec}}$. Applying a larger V$_{\text{prec}}$ causes a larger shift of V$_{\text{th}}$ towards negative voltage, while when V$_{\text{prec}}$= -5 V, V$_{\text{th}}$is located at roughly 1.7 V.

Interestingly, the second repetition of the C-V scan looks identical in all the three conditions (Figure 6.6b), and V$_{\text{th}}$ is roughly at the same position as in the first repetition when V$_{\text{prec}}$= -5 V.

This experiment indicates that the position of V$_{\text{th}}$ is dynamic rather than static. This phenomenon can be caused by the formation of trap states. A larger V$_{\text{prec}}$ increases the amount of trapped charge, which causes a larger change of V$_{\text{th}}$. When a negative V$_{\text{prec}}$ is applied for a long time instead, the trapped charges can be extracted, and the threshold voltage, V$_{\text{th}}$ is observed at higher voltage. Following this reasoning, the fact that the second repetition is independent of V$_{\text{prec}}$, can be explained in two ways:

- the amount of trapped charges decreases with time. By the time the first repetition is done, almost all the charges are released from the trap states, and the V_{th} shifts to higher voltage
- reaching 2.5 V as a final voltage step of the first repetition, sets a specific distribution of trapped charges. The second repetition therefore is identical in all three cases

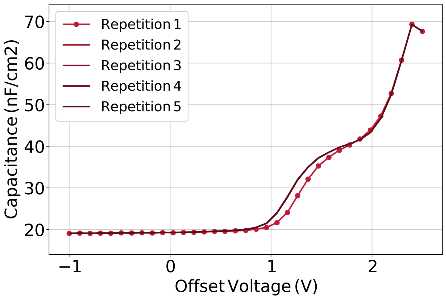

Figure 6.7: Multiple repetitions of a C-V scan performed after a preconditioning at 4 V for 10 minutes. For the plot, markers are used only in the first repetition, from the second to the fifth repetition the curves are identical.

To understand which of the two theories is correct, I first measured five repetitions of the C-V scan. Figure 6.7 shows that only the first repetition is different from the others. This result indicates that there is no continuous variation of the shift of V_{th} over time. However, the first theory cannot be excluded since one could argue that by the time the first repetition is performed, all the trapped charges are released, and therefore there is no possibility for V_{th} to further shift.

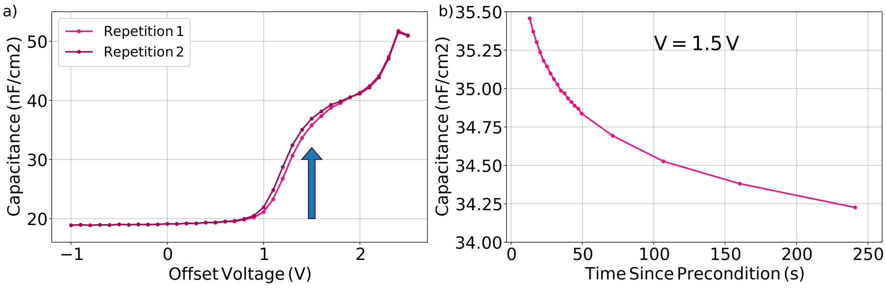

Figure 6.8: (a) Two repetitions C-V scan, V_{prec}= 4 V (10 minutes). (b) Transient-capacitance measured at 1.5 V, V_{prec}= 4 V (10 minutes).

To finally discern between the two theories, a two-repetitions C-V is compared with a transient capacitance measurement (Figure 6.8). During this experiment, after preconditioning, the device is set at a specific voltage (in this case 1.5 V), and capacitance is measured over time.

Figure 6.8a shows that the capacitance at 1.5 V increases from the first to the second repetition. Figure 6.8b instead shows that with the device kept at 1.5 V, the capacitance decreases over time. This result indicates that the first of the two theories described before is correct: the first two repetitions differ because applying 2.5 V has the effect of changing the distribution of trapped charges.

The results of this section can be summarized in three points:

- the shift of V_{th} is not permanent and it depends on the specific condition of the device before C-V is measured
- a simple C-V scan until 2.5 V modifies the state of the device so that two repetitions of a C-V give different results
- the capacitance decreases over time when measured at a specific voltage

These three points are perfectly in line with the hypothesis that the generation of trap states during degradation has an important influence on the shift of V_{th}.

It must be noted that the amount, and also the direction, of the shift of V_{th} differ between Figure 6.6 and Figure 6.7-Figure 6.8. The reason is that the first is measured at LT60, while the other two at LT90. Any other experiments shown in this thesis is performed at LT60.

6.5 EXPERIMENTAL RESULTS-EFFECT OF REACHING 2.5 V

From the discuss of the previous section, I reached the conclusion that trap states are responsible for the variation of V_{th}. Additionally, it is found that the density of trapped charges is strongly dependent on the last voltage applied when measuring a C-V scan. In particular, 2.5 V seems to be a level which reduces the amount of trapped charge. A schematic of this description during a two-repetitions C-V scan is shown in Figure 6.9.

To further investigate this effect, this experiment is performed: first, the device is preconditioned (V_{prec}=5 V for 10 minutes); afterwards, a voltage step of different duration of 2.5 V is applied; at the end, C-V is measured. The result in Figure 6.10 shows a clear and continuous variation of V_{th} from the first to the second repetition seen in Figure 6.6.

The fact that trapped charges are released when 2.5 V is applied for a few ms, is not straightforward to understand, especially considering the fact that during a C-V scan, -1 V, -0.5 V, ... are applied. Intuitively, one could expect that applying a negative bias can extract the trapped charge.

To understand the effect of applying a reversed bias, an experiment is done with the following routine: a voltage pulse of 5 V for 5 seconds is applied first, in order to set the device in a traps-filled condition; afterwards, a preconditioning of 2 seconds at a negative voltage is done (at a different level, from -1 V to 1 V); at the end C-V is measured,

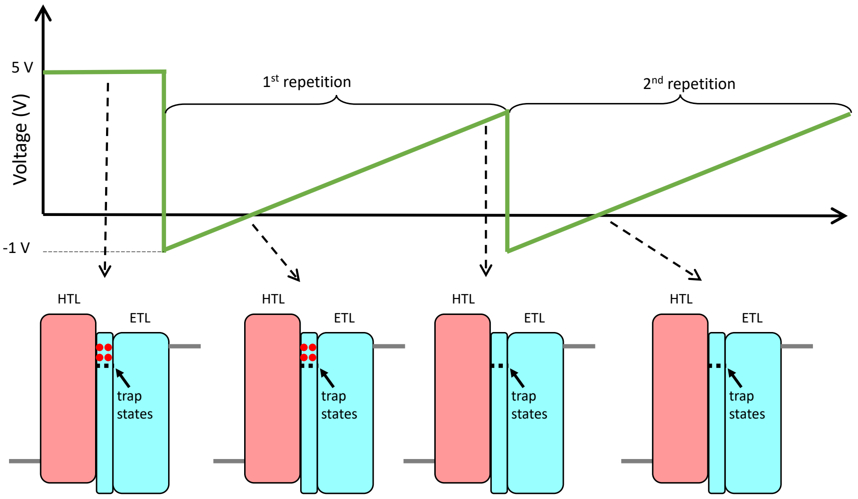

Figure 6.9: Schematics of the process of trap release during a two-repetition C-V scan. During steady-state of 5 V trap states are generated and filled with traps. The first C-V scan sees a device with a large amount of trapped charges. By reaching 2.5 V, at the end of the first C-V scan, trapped charges are released. The following ramps see a device without trapped charges.

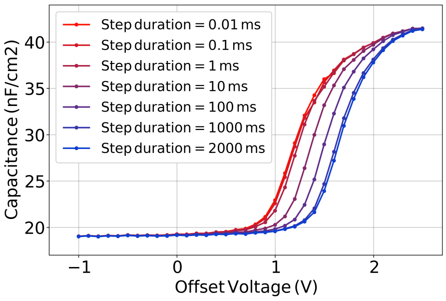

Figure 6.10: C-V scans, preconditioned at 5 V for 10 minutes. Between the preconditioning and the C-V measurements, 2.5 V are applied for a different amount of time.

starting from the preconditioning voltage. In this experiment V_{prec} is equal to the initial voltage of the C-V scan, and is called $V_{initial}$. It can be observed that in this case the initial voltage pulse of 5 seconds replaces the preconditioning of 10 minutes used in the previous experiments. This fact should not affect the result since 5 seconds are sufficient to reach a steady-state condition in forward voltage, allowing the trap states to be filled.

The result of this analysis is shown in Figure 6.11. The C-V curve is completely independent of $V_{initial}$. It is clear that applying a negative voltage does not induce the shift of V_{th} seen when 2.5 V is applied.

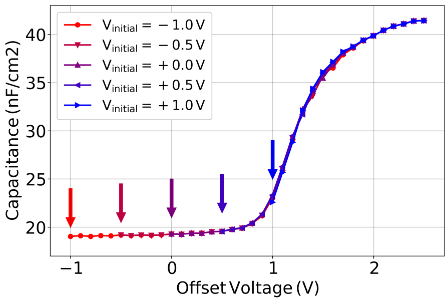

Figure 6.11: C-V performed starting from a different voltage, $V_{initial}$ (preconditioning for 2 seconds at $V_{initial}$). Before the experiment 5 V for 5 seconds are applied.

6.6 IMPEDANCE SIMULATIONS - INCLUDING SHOCKLEY-READ-HALL RECOMBINATION

One way to explain the reduction of trapped charges occurring when 2.5 V is reached, is to take into account Shockley-Read-Hall (SRH) recombination. As seen in the JV curves (Figure 6.2a), at 2.5 V charges are already injected into the device. The interaction between free and trapped charge, by means of SRH, could lead to a depletion of the trapped charge. This effect is investigated in the this section with the support of simulations.

Also in this case I consider the simplified stack used previously. SRH can be modeled with *Setfos* by simply activating it and indicating an additional parameter, the capture rate of the opposite charge carrier (in this case hole capture rate, having defined electron trap states), $c_{\text{t-e-h}}$.

Firstly, I compared the change in the density of trapped charge when an intermediate step of -1 or 2.8 V in between a steady-state voltage of 5 V and the C-V scan. The applied voltage consists of: 5 V steady-state; intermediate step for 2 ms at -1 V and 2.8 V; final voltage ramp during which the impedance simulation is performed. Again, only electron trap states are considered, with the following parameters (identical to the one chosen in the previous simulations): $E_{\text{t-e}} = 0.7\,\text{eV}$, $n_{\text{t-e}} = 10^{19}\,\text{cm}^{-3}$, $c_{\text{t-e}} = 10^{-10}\,\text{cm}^3/\text{s}$ and $c_{\text{t-e-h}} = 10^{-13}\,\text{cm}^3/\text{s}$. A voltage value of 2.8 V is used instead of 2.5 V because, in the simplified modeled device, injection starts at slightly larger voltage with respect to the real ones.

The results indicate that when -1 V is applied as intermediate step, the trapped electron density is still rather large. This causes the V_{th} of the C-V scan to be located at 1.5 V. Instead, when 2.8 V are applied, the trapped electron density is reduced, because they recombined with free holes through SRH. In this case the V_{th} occurs at 2.6 V.

Secondly, a three-repetition C-V scan is simulated. In Figure 6.13 the comparison between the model including or not SRH is shown. When SRH is considered (Figure 6.13a), the first repetition is the

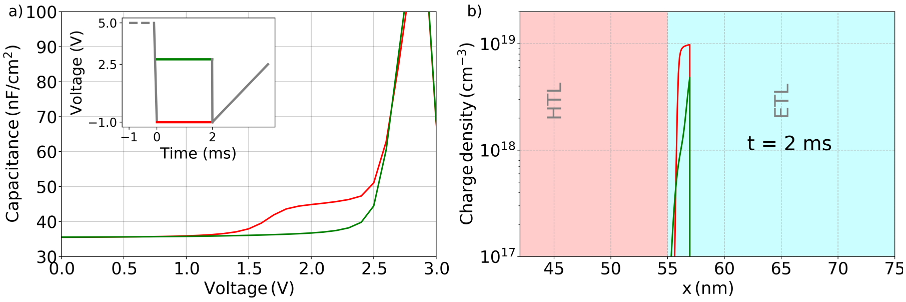

Figure 6.12: (a) Transient-impedance simulation. The applied voltage starts from the steady state value of 5 V, an intermediate step of -1 or 2.8 V and then the ramp starts; (a-inset) applied voltage (the ramp in gray is not in scale, a ramp rate of 0.33 V/s is used); (b) Distribution of trapped electrons at 2 ms, when the voltage ramp starts.

only one showing a V_{th} shifted to 1.5 V. By reaching 2.8 V in the first ramp, enough free charges are injected and can interact with trap states through SRH, causing a reduction of the trapped electrons. In the second repetition V_{th} is observed at higher voltage, since fewer electrons are still trapped. Without including SRH in the model, the C-V curves look identical for all repetitions (Figure 6.13b). This implies that SRH is a necessary model ingredient to explain the experimental observations of the sequential C-V ramps.

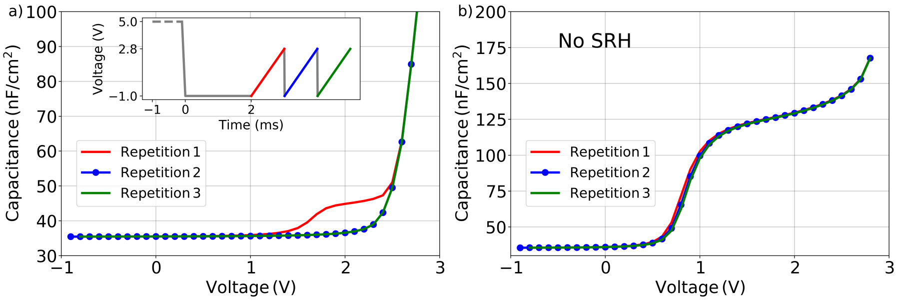

Figure 6.13: (a) Transient-impedance simulation including SRH recombination. The applied voltage starts from the steady state value of 5 V, an intermediate step at -1 V for 2 ms is considered before the ramps start; (a-inset) applied voltage (the ramp is not in scale, a ramp rate of 0.33 V/s is used). The end voltage of the ramp is 2.8 V; (b) The same simulations of (a) but without SRH recombination.

The only experimental result which can not be explained with this modeling approach including SRH is the shift of V_{th} in the opposite direction, occurring in devices at LT90 (Figure 6.7 and Figure 6.8a). In my opinion, the simplified stack used in the simulations presented in this chapter is certainly useful to understand the main influence that trapped charge has on a C-V scan, but it can not perfectly model the real device. For example, charge traps can form in the entire EML, at the interfaces with the blocking layers, or even in the transport layers. Moreover, only electron trap states are considered in these simulations, while in the real case hole trap states are equally possible. Additionally, polarity has not been included in the model, while it is probably present in the real stack.

From these considerations, I can assume that, during stressing, trap states are generated at different locations inside the stack. This fact might cause the opposite shift of V_{th} at different degradation stages observed in the experimental results. However, modeling the complete stack at different degradation stages is rather complex, and goes beyond the goal of this study.

6.7 CONCLUSIONS

The detailed electro-optical investigation during device stressing, performed in this study, allows to get important information about the degradation processes. In particular, the C-V measurements provides interesting results, showing an initial decrease followed by an increase of V_{th}.

More detailed experimental results allow to capture the dynamic nature of the shift. The shift of V_{th} to lower voltage is not a permanent effect, since it strongly depends on the last voltage applied to the OLED before measuring C-V. In particular, applying 2.5 V before measuring C-V, causes an increase of V_{th} of about 0.5 V with respect to the value observed when 5 V is applied.

By means of simulations I was able to show that trap states can cause the initial shift of V_{th} to lower voltage. The presence of trapped charge creates a charged interface, which is responsible for the shift.

Additionally, also the increase of V_{th}, when 2.5 V is applied, can be reproduced with simulations by taking SRH recombination into account. The interaction between free and trapped charge, introduced by SRH, has the effect of diminishing the amount of trapped charge, which in turns causes an increase of V_{th}.

7

SUMMARY AND OUTLOOK

Thermally-activated delayed fluorescence emitters will possibly be used in next generation of the OLED displays. Though offering attractive performance attributes, this technology does not meet the expected requirements to be used in commercial products at the moment, especially because of the short lifespan of these devices. The work presented in this thesis aims at supporting the research community by providing new methodologies to better understand, and possibly improve, the performance of TADF OLEDs.

In Chapter 3 the influence of non-radiative decay rates on the OLED efficiency is analyzed. The ability of TADF materials to convert triplet states into singlets is the key advantage of these emitters. However, the presence of non-radiative decay events of triplet or singlet states diminishes the overall efficiency of the OLED device. In this study the reduction of efficiency caused by such loss mechanisms is quantified. From the calculations, it is clear that the non-radiative decay events occurring on the triplet state are much more detrimental than the ones happening on the singlet. In the specific case considered in this study, the efficiency is reduced by 50% when the non-radiative decay rate is occuring entirely on the triplet state with respect to the singlet case. This result shows the importance of being able to determine these two quantities separately, in order to correctly foresee the expected efficiency of a specific TADF emitter. For this reason, a fitting algorithm is provided to estimate the entire set of decay rates by performing commonly used experimental techniques on TADF materials, such as photoluminescence quantum yield (with and without the presence of oxygen) and transient photoluminescence.

In Chapter 4 four OLEDs with different concentrations of TADF molecules in the emissive layer are investigated. The characterization of these devices is done using several experimental techniques, in steady-state, transient and frequency domain. With electro-optical simulations, a model for each device is created and optimized by comparing the experimental and simulated results. The fact that a multitude of techniques is used, reduces the correlation between the model parameters, ensuring the reliability of the final conclusions. With this analysis, I was able to observe that the charge transport and injection into the emissive layer can be classified in two regimes: the high and low dye concentration regimes. Moreover, the annihilation processes occurring in the different devices are quantified, and it is found that they scale logarithmically with the guest molecule concentration. This study provides a basis for upcoming work on simulation based guest concentration optimization in a complete OLED device.

In the last two chapters of the thesis, the limited lifetime and underlying degradation mechanisms of TADF OLEDs are investigated.

In Chapter 5 several identical devices are stressed at different current and temperature levels, and the emitted light is measured. A phenomenological mathematical model describing the light decay at specific current and temperature is used in a fitting algorithm. The fit is defined to take into account the entire set of curves at the same time, in this way the correlation between the free parameters is reduced. Once the fitting parameters are found, the model can be used to estimate the OLED degradation at any combination of current and temperature, without the need of actually measuring it. Additionally, the same fitting algorithm can be used to infer the light decay in standard operating conditions, though the actual measurements were only performed at accelerated conditions, namely at high current and temperature. This saves measurement time without lack of accuracy in determining the device lifetime. In this thesis I showed that by taking into account only accelerated degradation curves, the estimated light decay in standard conditions is predicted with an error of only 8% despite a reduction of almost 70% in measurement time.

Chapter 6 describes a detailed analysis of the degradation of a specific TADF OLED. In this chapter, the stressing at constant current used in Chapter 5 is combined with a detailed characterization, similar to the one performed in Chapter 4. A series of experiments is done during stressing interruptions and electrical simulations are used to qualitatively understand the nature of the processes occurring during degradation. From the experimental results, a clear shift of the transition voltage, in the capacitance-voltage measurements, is observed. The shift occurs first towards lower voltages, and later towards higher. With additional experiments and device simulations, I found evidence that the generation of trap states is the mechanism responsible for the shift. The presence of trapped charge causes the injection of free charges to occur at different voltage. The same result is obtained in simulations, when trap states are included into the model. Additionally, it is observed experimentally that the trapped charge cannot be released by simply applying a negative voltage for a few seconds. Instead, the application of 2.5 V for a few ms causes the release of almost the entire amount of trapped charge. Device simulations show that Shockley-Read-Hall recombination can be responsible for this release, because the free charges, injected at 2.5 V, can interact with the trapped charge.

The study presented in Chapter 6 was done on a single device stack, and for this reason a complete understanding of the dynamics of the generation of trap states is rather difficult. An analysis of several devices, with different thickness of the key layers, would allow a better understanding of the occurring processes, for example identifying the interface at which the trap states are generated.

This thesis hopefully demonstrated that further insights into the operating and degradation mechanisms of next generation OLEDs can be obtained by combining data collected from various measurement techniques with numerical device simulations.

ACKNOWLEDGMENTS

I acknowledge the following people who supported this work:

- Prof. Dr. Wolfgang Brütting (University of Augsburg), examiner
- Prof. Dr. Beat Ruhstaller (Fluxim AG, ZHAW), examiner
- Prof. Dr. Achim Wixfoth (University of Augsburg), board of examiners
- Prof. Dr. Liviu Chioncel (University of Augsburg), board of examiners
- Dr. Sandra Jenatsch (Fluxim AG) for proof-reading and discussions
- Dr. Simon Züfle (Fluxim AG, ZHAW) for discussions
- The research group at University of Augsburg for fabrication of OLED samples and providing experimental results (Prakhar Sahay, Dr. Markus Schmid and Prof. Dr. Wolfgang Brütting)
- The research group at University of Durham for providing experimental results (Kleitos Stavrou, Dr. Andrew Danos and Prof. Dr. Andrew P. Monkman)
- The research group at Merck KGaA for fabrication of OLED samples (Daniel Hudson and Dr. Christof Pflumm
- The Marie Skłodowska-Curie Actions for financial support via the Innovative Training Program (ITN) TADFlife (GA 812872)

PUBLICATION LIST

First author publications:

- **Determining non-radiative decay rates in TADF compounds using coupled transient and steady-state optical data** Stefano Sem, Sandra Jenatsch, Kleitos Stavrou, Andrew Danos, Andrew P. Monkman and Beat Ruhstaller. Journal of material chemistry C. DOI: 10.1039/d1tc05594a.
- **Detailed electro-optical modeling of thermally-activated delayed fluorescent OLEDs with different host-guest concentrations** Stefano Sem, Sandra Jenatsch, Prakhar Sahay, Simon Züfle, Markus Schmid, Wolfgang Brütting and Beat Ruhstaller. Organic Electronics. DOI: 10.1016/j.orgel.2022.

BIBLIOGRAPHY

[1] Web page: *https://www.marketsandmarkets.com/Market-Reports/display-market-925.html*.

[2] Pierre Boher, Thierry Leroux, and Pierre Blanc. "Viewing angle Color evaluation of QLED and OLED HDR displays using lab and ICtCp Color spaces." In: *Proceedings of the International Display Workshops* 2.January 2018 (2017), pp. 1036–1039. ISSN: 18832490.

[3] Pierre M. Boher, Thierry Leroux, and Pierre Blanc. "Color volumes in lab and ICtCp color spaces for viewing angle color characterization of QLED and OLED HDR/WCG displays." In: February (2018), p. 11. ISSN: 1996756X. DOI: 10.1117/12.2285371.

[4] Amlan K. Pal, Simonas Krotkus, Mattia Fontani, Campbell F.R. Mackenzie, David B. Cordes, Alexandra M.Z. Slawin, Ifor D.W. Samuel, and Eli Zysman-Colman. "High-Efficiency Deep-Blue-Emitting Organic Light-Emitting Diodes Based on Iridium(III) Carbene Complexes." In: *Advanced Materials* 30.50 (2018), pp. 1–10. ISSN: 15214095. DOI: 10.1002/adma.201804231.

[5] Cai Jun Zheng, Wei Ming Zhao, Zhi Qiang Wang, Da Huang, Jun Ye, Xue Mei Ou, Xiao Hong Zhang, Chun Sing Lee, and Shuit Tong Lee. "Highly efficient non-doped deep-blue organic light-emitting diodes based on anthracene derivatives." In: *Journal of Materials Chemistry* 20.8 (2010), pp. 1560–1566. ISSN: 09599428. DOI: 10.1039/b918739a.

[6] M. A. Baldo, M. E. Thompson, and S. R. Forrest. "High-efficiency fluorescent organic light-emitting devices using a phosphorescent sensitizer." In: *Nature* 403.6771 (2000), pp. 750–753. ISSN: 00280836. DOI: 10.1038/35001541.

[7] Jiun Haw Lee, Chia Hsun Chen, Pei Hsi Lee, Hung Yi Lin, Man Kit Leung, Tien Lung Chiu, and Chi Feng Lin. "Blue organic light-emitting diodes: Current status, challenges, and future outlook." In: *Journal of Materials Chemistry C* 7.20 (2019), pp. 5874–5888. ISSN: 20507526. DOI: 10.1039/c9tc00204a.

[8] Markus Regnat, Kurt P. Pernstich, Kwon Hyeon Kim, Jang Joo Kim, Frank Nüesch, and Beat Ruhstaller. "Routes for Efficiency Enhancement in Fluorescent TADF Exciplex Host OLEDs Gained from an Electro-Optical Device Model." In: *Advanced Electronic Materials* 6.2 (2020), pp. 1–8. ISSN: 2199160X. DOI: 10.1002/aelm.201900804.

[9] Christian Mayr, Sae Youn Lee, Tobias D. Schmidt, Takuma Yasuda, Chihaya Adachi, and Wolfgang Brütting. "Efficiency enhancement of organic light-emitting diodes incorporating a highly oriented thermally activated delayed fluorescence emitter." In: *Advanced Functional Materials* 24.33 (2014), pp. 5232–5239. ISSN: 16163028. DOI: `10.1002/adfm.201400495`.

[10] Ayataka Endo, Keigo Sato, Kazuaki Yoshimura, Takahiro Kai, Atsushi Kawada, Hiroshi Miyazaki, and Chihaya Adachi. "Efficient up-conversion of triplet excitons into a singlet state and its application for organic light emitting diodes." In: *Applied Physics Letters* 98.8 (2011), pp. 2011–2014. ISSN: 00036951. DOI: `10.1063/1.3558906`.

[11] Hajime Nakanotani, Takahiro Higuchi, Taro Furukawa, Kensuke Masui, Kei Morimoto, Masaki Numata, Hiroyuki Tanaka, Yuta Sagara, Takuma Yasuda, and Chihaya Adachi. "High-efficiency organic light-emitting diodes with fluorescent emitters." In: *Nature Communications* 5.May (2014), pp. 1–7. ISSN: 20411723. DOI: `10.1038/ncomms5016`.

[12] Paloma L. Dos Santos, Jonathan S. Ward, Martin R. Bryce, and Andrew P. Monkman. "Using Guest-Host Interactions to Optimize the Efficiency of TADF OLEDs." In: *Journal of Physical Chemistry Letters* 7.17 (2016), pp. 3341–3346. ISSN: 19487185. DOI: `10.1021/acs.jpclett.6b01542`.

[13] Lin Song Cui, Shi Bin Ruan, Fatima Bencheikh, Ryo Nagata, Lei Zhang, Ko Inada, Hajime Nakanotani, Liang Sheng Liao, and Chihaya Adachi. "Long-lived efficient delayed fluorescence organic light-emitting diodes using n-type hosts." In: *Nature Communications* 8.1 (2017), pp. 1–8. ISSN: 20411723. DOI: `10.1038/s41467-017-02419-x`. URL: `http://dx.doi.org/10.1038/s41467-017-02419-x`.

[14] Shi Jie Zou, Yang Shen, Feng Ming Xie, Jing De Chen, Yan Qing Li, and Jian Xin Tang. "Recent advances in organic light-emitting diodes: Toward smart lighting and displays." In: *Materials Chemistry Frontiers* 4.3 (2020), pp. 788–820. ISSN: 20521537. DOI: `10.1039/c9qm00716d`.

[15] Wolfgang Brütting, Stefan Berleb, and Anton G. Mückl. "Device physics of organic light-emitting diodes based on molecular materials." In: *Organic Electronics* 2.1 (2001), pp. 1–36. ISSN: 15661199. DOI: `10.1016/S1566-1199(01)00009-X`.

[16] Yoon Heung Tak, Ki Beom Kim, Hyoung Guen Park, Kwang Ho Lee, and Jong Ram Lee. "Criteria for ITO (indium-tin-oxide) thin film as the bottom electrode of an organic light emitting diode." In: *Thin Solid Films* 411.1 (2002), pp. 12–16. ISSN: 00406090. DOI: `10.1016/S0040-6090(02)00165-7`.

[17] R. H. Friend et al. “Electroluminescence in conjugated polymers.” In: *Nature* 397.6715 (1999), pp. 121–128. ISSN: 00280836. DOI: 10.1038/16393.

[18] S. A. Carter, M. Angelopoulos, S. Karg, P. J. Brock, and J. C. Scott. “Polymeric anodes for improved polymer light-emitting diode performance.” In: *Applied Physics Letters* 70.16 (1997), pp. 2067–2069. ISSN: 00036951. DOI: 10.1063/1.118953.

[19] Z. Y. Zhong and Y. D. Jiang. “The effect of electrode materials on the performance of OLEDs.” In: *ICO20: Display Devices and Systems* 6030 (2006), 60300J. ISSN: 0277786X. DOI: 10.1117/12.667376.

[20] Jwo Huei Jou, Sudhir Kumar, Abhishek Agrawal, Tsung Han Li, and Snehashis Sahoo. “Approaches for fabricating high efficiency organic light emitting diodes.” In: *Journal of Materials Chemistry C* 3.13 (2015), pp. 2974–3002. ISSN: 20507526. DOI: 10.1039/c4tc02495h. URL: http://dx.doi.org/10.1039/C4TC02495H.

[21] P. M. Borsenberger, L. Pautmeier, R. Richert, and H. Bässler. “Hole transport in 1,1-bis(di-4-tolylaminophenyl)cyclohexane.” In: *The Journal of Chemical Physics* 94.12 (1991), pp. 8276–8281. ISSN: 00219606. DOI: 10.1063/1.460112.

[22] Neetu Chopra, Jaewon Lee, Ying Zheng, Sang Hyun Eom, Jiangeng Xue, and Franky So. “High efficiency blue phosphorescent organic light-emitting device.” In: *Applied Physics Letters* 93.14 (2008), pp. 1–4. ISSN: 00036951. DOI: 10.1063/1.3000382.

[23] P. Strohriegl and J. V. Grazulevicius. “Charge-transporting molecular glasses.” In: *Advanced Materials* 14.20 (2002), pp. 1439–1452. ISSN: 09359648. DOI: 10.1002/1521-4095(20021016)14:20<1439::AID-ADMA1439>3.0.CO;2-H.

[24] Isao Tanaka, Yuichiro Tabata, and Shizuo Tokito. “Förster and Dexter energy-transfer processes in fluorescent BAlq thin films doped with phosphorescent Ir(ppy)3 molecules.” In: *Journal of Applied Physics* 99.7 (2006). ISSN: 00218979. DOI: 10.1063/1.2185835.

[25] Ming Han Tsai, Hao Wu Lin, Hai Ching Su, Tung Huei Ke, Chung Chih Wu, Fu Chuan Fang, Yuan Li Liao, Ken Tsung Wong, and Chih I. Wu. “Highly efficient organic blue electrophosphorescent devices based on 3,6-Bis(triphenylsilyl)carbazole as the host material.” In: *Advanced Materials* 18.9 (2006), pp. 1216–1220. ISSN: 09359648. DOI: 10.1002/adma.200502283.

[26] Chun Yu Chen et al. “Continuous blade coating for multi-layer large-area organic light-emitting diode and solar cell.” In: *Journal of Applied Physics* 110.9 (2011). ISSN: 00218979. DOI: 10.1063/1.3636398.

[27] Shubham Negi, Poornima Mittal, and Brijesh Kumar. "Performance analysis of OLED with hole block layer and impact of multiple hole block layer." In: *Communications in Computer and Information Science* 711 (2017), pp. 452–462. ISSN: 18650929. DOI: 10.1007/978-981-10-7470-7_45.

[28] Francesco Rodella, Sergey Bagnich, Eimantas Duda, Tobias Meier, Julian Kahle, Stavros Athanasopoulos, Anna Köhler, and Peter Strohriegl. "High Triplet Energy Host Materials for Blue TADF OLEDs—A Tool Box Approach." In: *Frontiers in Chemistry* 8.July (2020), pp. 1–16. ISSN: 22962646. DOI: 10.3389/fchem.2020.00657.

[29] Wook Song, Woochul Lee, Kong Kyeom Kim, and Jun Yeob Lee. "Correlation of doping concentration, charge transport of host, and lifetime of thermally activated delayed fluorescent devices." In: *Organic Electronics* 37 (2016), pp. 252–256. ISSN: 15661199. DOI: 10.1016/j.orgel.2016.07.002. URL: http://dx.doi.org/10.1016/j.orgel.2016.07.002.

[30] Kyu Sung Kim, Dong Uk Kim, Kuk Soung Joung, and Jae Woong Yu. "Balancing charge-transporting characteristics in bipolar host materials." In: *Thin Solid Films* 696.December 2019 (2020), p. 137781. ISSN: 00406090. DOI: 10.1016/j.tsf.2019.137781. URL: https://doi.org/10.1016/j.tsf.2019.137781.

[31] S. Sem, S. Jenatsch, P. Sahay, S. Züfle, M. Schmid, W. Brütting, and B. Ruhstaller. "Detailed electro-optical modeling of thermally-activated delayed fluorescent OLEDs with different host-guest concentrations." In: *Organic Electronics* 107.April (2022), p. 106553. ISSN: 15661199. DOI: 10.1016/j.orgel.2022.106553. URL: https://doi.org/10.1016/j.orgel.2022.106553.

[32] Shota Haseyama, Akitsugu Niwa, Takashi Kobayashi, Takashi Nagase, Kenichi Goushi, Chihaya Adachi, and Hiroyoshi Naito. "Control of the Singlet–Triplet Energy Gap in a Thermally Activated Delayed Fluorescence Emitter by Using a Polar Host Matrix." In: *Nanoscale Research Letters* 12.1 (2017), pp. 1–5. ISSN: 1556276X. DOI: 10.1186/s11671-017-2012-1.

[33] Gábor Méhes, Kenichi Goushi, William J. Potscavage, and Chihaya Adachi. "Influence of host matrix on thermally-activated delayed fluorescence: Effects on emission lifetime, photoluminescence quantum yield, and device performance." In: *Organic Electronics* 15.9 (2014), pp. 2027–2037. ISSN: 15661199. DOI: 10.1016/j.orgel.2014.05.027.

[34] Yi Lu Chang. *Efficient organic light-emitting diodes (OLEDs)*. 2015, pp. 1–114. ISBN: 9789814613811. DOI: 10.1201/b18760.

[35] Anna Köhler, Heinz Bässler, and Heinz Bässler Anna Köhler. *Electronic processes in organic semiconductors: An introduction*. 2015, pp. 1–405. ISBN: 9783527685172. DOI: `10.1002/9783527685172`.

[36] Jianzhang Zhao, Kepeng Chen, Yuqi Hou, Yuanyuan Che, Lang Liu, and Dianzeng Jia. "Recent progress in heavy atom-free organic compounds showing unexpected intersystem crossing (ISC) ability." In: *Organic and Biomolecular Chemistry* 16.20 (2018), pp. 3692–3701. ISSN: 14770520. DOI: `10.1039/c8ob00421h`.

[37] Miaosheng Wang, Tanmay Chatterjee, Camera Janelle Foster, Ting Wu, Chih Lun Yi, Haomiao Yu, Ken Tsung Wong, and Bin Hu. "Exploring mechanisms for generating spin-orbital coupling through donor-acceptor design to realize spin flipping in thermally activated delayed fluorescence." In: *Journal of Materials Chemistry C* 8.10 (2020), pp. 3395–3401. ISSN: 20507526. DOI: `10.1039/c9tc06078b`.

[38] Marc K Etherington, Jamie Gibson, Heather F Higginbotham, Thomas J Penfold, and Andrew P Monkman. "Revealing the spin–vibronic coupling mechanism of thermally activated delayed fluorescence." In: *Nature Communications* 7 (2016), pp. 1–7. DOI: `10.1038/ncomms13680`. URL: `http://dx.doi.org/10.1038/ncomms13680`.

[39] Jamie Gibson, Andrew P. Monkman, and Thomas J. Penfold. "The Importance of Vibronic Coupling for Efficient Reverse Intersystem Crossing in Thermally Activated Delayed Fluorescence Molecules." In: *ChemPhysChem* 1 (2016), pp. 2956–2961. ISSN: 14397641. DOI: `10.1002/cphc.201600662`.

[40] J. Gibson and T. J. Penfold. "Nonadiabatic coupling reduces the activation energy in thermally activated delayed fluorescence." In: *Physical Chemistry Chemical Physics* 19.12 (2017), pp. 8428–8434. ISSN: 14639076. DOI: `10.1039/c7cp00719a`.

[41] Fernando B. Dias et al. "The role of local triplet excited states and D-A relative orientation in thermally activated delayed fluorescence: Photophysics and devices." In: *Advanced Science* 3.12 (2016), pp. 1–10. ISSN: 21983844. DOI: `10.1002/advs.201600080`. arXiv: `advs.201600080 [DOI: 10.1002]`.

[42] Xinyi Cai, Bin Gao, Xiang Long Li, Yong Cao, and Shi Jian Su. "Singlet–Triplet Splitting Energy Management via Acceptor Substitution: Complanation Molecular Design for Deep-Blue Thermally Activated Delayed Fluorescence Emitters and Organic Light-Emitting Diodes Application." In: *Advanced Functional Materials* 26.44 (2016), pp. 8042–8052. ISSN: 16163028. DOI: `10.1002/adfm.201603520`.

[43] Hartmut Yersin, ed. *Highly Efficient OLEDs*. 2018. ISBN: 9783527339006. DOI: 10.1002/9783527691722.

[44] Masashi Mamada, Ko Inada, Takeshi Komino, William J. Potscavage, Hajime Nakanotani, and Chihaya Adachi. "Highly Efficient Thermally Activated Delayed Fluorescence from an Excited-State Intramolecular Proton Transfer System." In: *ACS Central Science* 3.7 (2017), pp. 769–777. ISSN: 23747951. DOI: 10.1021/acscentsci.7b00183.

[45] Ye Tao, Kai Yuan, Ting Chen, Peng Xu, Huanhuan Li, Runfeng Chen, Chao Zheng, Lei Zhang, and Wei Huang. "Thermally activated delayed fluorescence materials towards the breakthrough of organoelectronics." In: *Advanced Materials* 26.47 (2014), pp. 7931–7958. ISSN: 15214095. DOI: 10.1002/adma.201402532.

[46] Kleitos Stavrou, Larissa G. Franca, and Andrew P. Monkman. "Photophysics of TADF Guest-Host Systems: Introducing the Idea of Hosting Potential." In: *ACS Applied Electronic Materials* 2.9 (2020), pp. 2868–2881. ISSN: 26376113. DOI: 10.1021/acsaelm.0c00514.

[47] Brigitte Wex and Bilal R. Kaafarani. "Perspective on carbazole-based organic compounds as emitters and hosts in TADF applications." In: *Journal of Materials Chemistry C* 5.34 (2017), pp. 8622–8653. ISSN: 20507526. DOI: 10.1039/c7tc02156a.

[48] Jia Lin Cai, Wei Liu, Kai Wang, Jia Xiong Chen, Yi Zhong Shi, Ming Zhang, Cai Jun Zheng, Si Lu Tao, and Xiao Hong Zhang. "Highly efficient thermally activated delayed fluorescence emitter developed by replacing carbazole with 1,3,6,8-tetramethyl-carbazole." In: *Frontiers in Chemistry* 7.JAN (2019). ISSN: 22962646. DOI: 10.3389/fchem.2019.00017.

[49] Tomas Serevičius, Rokas Skaisgiris, Irina Fiodorova, Vytautas Steckis, Jelena Dodonova, Dovydas Banevičius, Karolis Kazlauskas, Saulius Juršėnas, and Sigitas Tumkevičius. "Achieving efficient deep-blue TADF in carbazole-pyrimidine compounds." In: *Organic Electronics* 82.March (2020). ISSN: 15661199. DOI: 10.1016/j.orgel.2020.105723.

[50] Hiroyuki Tanaka, Katsuyuki Shizu, Hiroshi Miyazaki, and Chihaya Adachi. "Efficient green thermally activated delayed fluorescence (TADF) from a phenoxazine–triphenyltriazine (PXZ–TRZ) derivative." In: *Chemical Communications* 48.93 (2012), pp. 11392–11394. ISSN: 1364548X. DOI: 10.1039/c2cc36237f.

[51] Tomas Serevičius, Rokas Skaisgiris, Jelena Dodonova, Laimis Jagintavičius, Dovydas Banevičius, Karolis Kazlauskas, Sigitas Tumkevičius, and Saulius Juršėnas. "Achieving Submicrosecond Thermally Activated Delayed Fluorescence Lifetime and

Highly Efficient Electroluminescence by Fine-Tuning of the Phenoxazine-Pyrimidine Structure.” In: *ACS Applied Materials and Interfaces* 12.9 (2020), pp. 10727–10736. ISSN: 19448252. DOI: 10.1021/acsami.9b21394.

[52] Sunyoung Sohn et al. “Synthesis and characterization of diphenylamine derivative containing malononitrile for thermally activated delayed fluorescent emitter.” In: *Dyes and Pigments* 140 (2017), pp. 14–21. ISSN: 18733743. DOI: 10.1016/j.dyepig.2017.01.010. URL: http://dx.doi.org/10.1016/j.dyepig.2017.01.010.

[53] Jie Li, Jincheng Zhang, Heqi Gong, Li Tao, Yanqing Wang, and Qiang Guo. “Efficient deep-blue electroluminescence employing heptazine-based thermally activated delayed fluorescence.” In: *Photonics* 8.8 (2021), pp. 4–11. ISSN: 23046732. DOI: 10.3390/photonics8080293.

[54] Tetsuya Nakagawa, Sung Yu Ku, Ken Tsung Wong, and Chihaya Adachi. “Electroluminescence based on thermally activated delayed fluorescence generated by a spirobifluorene donor–acceptor structure.” In: *Chemical Communications* 48.77 (2012), pp. 9580–9582. ISSN: 1364548X. DOI: 10.1039/c2cc31468a.

[55] Yang Liu, Xin Xiao, You Ran, Zhengyang Bin, and Jingsong You. “Molecular design of thermally activated delayed fluorescent emitters for narrowband orange-red OLEDs boosted by a cyano-functionalization strategy.” In: *Chemical Science* 12.27 (2021), pp. 9408–9412. ISSN: 20416539. DOI: 10.1039/d1sc02042k.

[56] Yirang Im and Jun Yeob Lee. “Above 20% external quantum efficiency in thermally activated delayed fluorescence device using furodipyridine-type host materials.” In: *Chemistry of Materials* 26.3 (2014), pp. 1413–1419. ISSN: 08974756. DOI: 10.1021/cm403358h.

[57] Hajime Nakanotani, Kensuke Masui, Junichi Nishide, Takumi Shibata, and Chihaya Adachi. “Promising operational stability of high-efficiency organic light-emitting diodes based on thermally activated delayed fluorescence.” In: *Scientific Reports* 3.Lt 50 (2013), pp. 1–6. ISSN: 20452322. DOI: 10.1038/srep02127.

[58] Rama Dhali, D. K.Andrea Phan Huu, Francesco Bertocchi, Cristina Sissa, Francesca Terenziani, and Anna Painelli. “Understanding TADF: a joint experimental and theoretical study of DMAC-TRZ.” In: *Physical chemistry chemical physics : PCCP* 23.1 (2021), pp. 378–387. ISSN: 14639084. DOI: 10.1039/d0cp05982j.

[59] Wei Lung Tsai et al. “A versatile thermally activated delayed fluorescence emitter for both highly efficient doped and non-doped organic light emitting devices.” In: *Chemical Commu-*

nications 51.71 (2015), pp. 13662–13665. ISSN: 1364548X. DOI: 10.1039/c5cc05022g.

[60] Dalius Gudeika, Oleksandr Bezvikonnyi, Dmytro Volyniuk, and Juozas V. Grazulevicius. "Differently substituted benzonitriles for non-doped OLEDs." In: *Dyes and Pigments* 172.August 2019 (2020), p. 107789. ISSN: 18733743. DOI: 10.1016/j.dyepig.2019.107789. URL: https://doi.org/10.1016/j.dyepig.2019.107789.

[61] Andrew Danos, Dalius Gudeika, Nadzeya A. Kukhta, Ramunas Lygaitis, Marco Colella, Heather F. Higginbotham, Aisha N. Bismillah, Paul R. McGonigal, Juozas Vidas Grazulevicius, and Andrew P. Monkman. "Not the sum of their parts: understanding multi-donor interactions in symmetric and asymmetric TADF emitters." In: *Journal of Materials Chemistry C* D (2022). ISSN: 2050-7526. DOI: 10.1039/d1tc04171a. URL: http://pubs.rsc.org/en/Content/ArticleLanding/2021/TC/D1TC04171A.

[62] Hiroki Hirai, Kiichi Nakajima, Soichiro Nakatsuka, Kazushi Shiren, Jingping Ni, Shintaro Nomura, Toshiaki Ikuta, and Takuji Hatakeyama. "One-Step Borylation of 1,3-Diaryloxybenzenes Towards Efficient Materials for Organic Light-Emitting Diodes." In: *Angewandte Chemie - International Edition* 54.46 (2015), pp. 13581–13585. ISSN: 15213773. DOI: 10.1002/anie.201506335.

[63] Subeesh Madayanad Suresh, David Hall, David Beljonne, Yoann Olivier, and Eli Zysman-Colman. "Multiresonant Thermally Activated Delayed Fluorescence Emitters Based on Heteroatom-Doped Nanographenes: Recent Advances and Prospects for Organic Light-Emitting Diodes." In: *Advanced Functional Materials* 30.33 (2020). ISSN: 16163028. DOI: 10.1002/adfm.201908677.

[64] T. Northey and T. J. Penfold. "The intersystem crossing mechanism of an ultrapure blue organoboron emitter." In: *Organic Electronics* 59 (2018), pp. 45–48. ISSN: 15661199. DOI: 10.1016/j.orgel.2018.04.038. URL: https://doi.org/10.1016/j.orgel.2018.04.038.

[65] Takuji Hatakeyama, Kazushi Shiren, Kiichi Nakajima, Shintaro Nomura, Soichiro Nakatsuka, Keisuke Kinoshita, Jingping Ni, Yohei Ono, and Toshiaki Ikuta. "Ultrapure Blue Thermally Activated Delayed Fluorescence Molecules: Efficient HOMO-LUMO Separation by the Multiple Resonance Effect." In: *Advanced Materials* 28.14 (2016), pp. 2777–2781. ISSN: 15214095. DOI: 10.1002/adma.201505491.

[66] Web Page: *https://en.wikipedia.org/wiki/CIE_1931_color_space*.

[67] Yasuhiro Kondo, Kazuki Yoshiura, Sayuri Kitera, Hiroki Nishi, Susumu Oda, Hajime Gotoh, Yasuyuki Sasada, Motoki Yanai, and Takuji Hatakeyama. "Narrowband deep-blue organic light-

emitting diode featuring an organoboron-based emitter." In: *Nature Photonics* 13.10 (2019), pp. 678–682. ISSN: 17494893. DOI: `10.1038/s41566-019-0476-5`. URL: `http://dx.doi.org/10.1038/s41566-019-0476-5`.

[68] Kleitos Stavrou, Andrew Danos, Toshiki Hama, Takuji Hatakeyama, and Andrew Monkman. "Hot vibrational states in a high-performance multiple resonance emitter and the effect of excimer quenching on organic light-emitting diodes." In: *ACS Applied Materials and Interfaces* 13.7 (2021), pp. 8643–8655. ISSN: 19448252. DOI: `10.1021/acsami.0c20619`.

[69] Chin Yiu Chan, Masaki Tanaka, Yi Ting Lee, Yiu Wing Wong, Hajime Nakanotani, Takuji Hatakeyama, and Chihaya Adachi. "Stable pure-blue hyperfluorescence organic light-emitting diodes with high-efficiency and narrow emission." In: *Nature Photonics* 15.3 (2021), pp. 203–207. ISSN: 17494893. DOI: `10.1038/s41566-020-00745-z`. URL: `http://dx.doi.org/10.1038/s41566-020-00745-z`.

[70] Hadi Abroshan, Veaceslav Coropceanu, and Jean Luc Brédas. "Hyperfluorescence-based emission in purely organic materials: Suppression of energy-loss mechanisms via alignment of triplet excited states." In: *ACS Materials Letters* 2.11 (2020), pp. 1412–1418. ISSN: 26394979. DOI: `10.1021/acsmaterialslett.0c00407`.

[71] "Fluxim AG, Switzerland, see www.fluxim.com for Paios." In: ().

[72] G Juska, K Arlauskas, and M Vili. "Extraction Current Transients: New Method of Study of Charge Transport in Microcrystalline Silicon." In: *Physical Review Letters* (2000), pp. 1–4.

[73] Stefan Nowy, Wei Ren, Andreas Elschner, Wilfried Lövenich, and Wolfgang Brütting. "Impedance spectroscopy as a probe for the degradation of organic light-emitting diodes." In: *Journal of Applied Physics* 107.5 (2010), pp. 1–10. ISSN: 00218979. DOI: `10.1063/1.3294642`.

[74] Simon Züfle, Stéphane Altazin, Alexander Hofmann, Lars Jäger, Martin T. Neukom, Tobias D. Schmidt, Wolfgang Brütting, and Beat Ruhstaller. "The use of charge extraction by linearly increasing voltage in polar organic light-emitting diodes." In: *Journal of Applied Physics* 121.17 (2017). ISSN: 10897550. DOI: `10.1063/1.4982903`.

[75] P. Chulkin, O. Vybornyi, M. Lapkowski, P. J. Skabara, and P. Data. "Impedance spectroscopy of OLEDs as a tool for estimating mobility and the concentration of charge carriers in transport layers." In: *Journal of Materials Chemistry C* 6.5 (2018),

pp. 1008–1014. ISSN: 20507526. DOI: 10.1039/c7tc04599a. URL: http://dx.doi.org/10.1039/C7TC04599A.

[76] Simon Züfle, Martin T. Neukom, Stéphane Altazin, Marc Zinggeler, Marek Chrapa, Ton Offermans, and Beat Ruhstaller. “An effective area approach to model lateral degradation in organic solar cells.” In: *Advanced Energy Materials* 5.20 (2015), pp. 1–9. ISSN: 16146840. DOI: 10.1002/aenm.201500835.

[77] Mingdong Wang, Fangyan Xie, Jun Du, Qin Tang, Shizhao Zheng, Qian Miao, Jian Chen, Ni Zhao, and J. B. Xu. “Degradation mechanism of organic solar cells with aluminum cathode.” In: *Solar Energy Materials and Solar Cells* 95.12 (2011), pp. 3303–3310. ISSN: 09270248. DOI: 10.1016/j.solmat.2011.07.020.

[78] Stefan Berleb, Wolfgang Brütting, and Gernot Paasch. “Interfacial charges and electric field distribution in organic heterolayer light-emitting devices.” In: *Organic Electronics* 1.1 (2000), pp. 41–47. ISSN: 15661199. DOI: 10.1016/S1566-1199(00)00007-0.

[79] Vladimir Petrovsky, Abhishek Manohar, and Fatih Dogan. “Dielectric constant of particles determined by impedance spectroscopy.” In: *Journal of Applied Physics* 100.1 (2006). ISSN: 00218979. DOI: 10.1063/1.2206411.

[80] S. Reineke, F. Lindner, Q. Huang, G. Schwartz, K. Walzer, and K. Leo. “Measuring carrier mobility in conventional multilayer organic light emitting devices by delayed exciton generation.” In: *Physica Status Solidi (B) Basic Research* 245.5 (2008), pp. 804–809. ISSN: 03701972. DOI: 10.1002/pssb.200743447.

[81] A. J. Pal, R. Österbacka, K. M. Källman, and H. Stubb. “Transient electroluminescence: Mobility and response time in quinquethiophene Langmuir-Blodgett films.” In: *Applied Physics Letters* 71.2 (1997), pp. 228–230. ISSN: 00036951. DOI: 10.1063/1.119917.

[82] Ming Te Lin, Minghang Li, Wei Hsuan Chen, Mohammad A. Omary, and Nigel D. Shepherd. “Transient electroluminescence determination of carrier mobility and charge trapping effects in heavily doped phosphorescent organic light-emitting diodes.” In: *Solid-State Electronics* 56.1 (2011), pp. 196–200. ISSN: 00381101. DOI: 10.1016/j.sse.2010.10.018. URL: http://dx.doi.org/10.1016/j.sse.2010.10.018.

[83] Markus Regnat, Kurt P. Pernstich, Simon Züfle, and Beat Ruhstaller. “Analysis of the Bias-Dependent Split Emission Zone in Phosphorescent OLEDs.” In: *ACS Applied Materials and Interfaces* 10.37 (2018), pp. 31552–31559. ISSN: 19448252. DOI: 10.1021/acsami.8b09595.

[84] Jooyoun Kang et al. “Time-Resolved Electroluminescence Study for the Effect of Charge Traps on the Luminescence Properties of Organic Light-Emitting Diodes.” In: *Physica Status Solidi (A) Applications and Materials Science* 217.17 (2020). ISSN: 18626319. DOI: `10.1002/pssa.202000081`.

[85] Jeannine Grüne, Nikolai Bunzmann, Moritz Meinecke, Vladimir Dyakonov, and Andreas Sperlich. “Kinetic Modeling of Transient Electroluminescence Reveals TTA as an Efficiency-Limiting Process in Exciplex-Based TADF OLEDs.” In: *Journal of Physical Chemistry C* 124.47 (2020), pp. 25667–25674. ISSN: 19327455. DOI: `10.1021/acs.jpcc.0c06528`.

[86] Gyeong Won Lee, Yoonsuk Choi, Heejin Kim, Jongwoo Park, Jong In Shim, and Dong Soo Shin. “Analysis of transient degradation behaviors of organic light-emitting diodes under electrical stress.” In: *Applied Sciences (Switzerland)* 11.16 (2021). ISSN: 20763417. DOI: `10.3390/app11167627`.

[87] Quan Niu, Paul W.M. Blom, Falk May, Paul Heimel, Minlu Zhang, Christian Eickhoff, Ute Heinemeyer, Christian Lennartz, and N. Irina Crăciun. “Transient electroluminescence on pristine and degraded phosphorescent blue OLEDs.” In: *Journal of Applied Physics* 122.18 (2017). ISSN: 10897550. DOI: `10.1063/1.5006587`.

[88] Hyunijong Kim, Jihoon Yang, Ye Seokmin, and Jeong Jaewook. “OLED degradation mechanism sudy using impedance spectroscopy.” In: ().

[89] Tobias D. Schmidt, Lars Jäger, Yutaka Noguchi, Hisao Ishii, and Wolfgang Brütting. “Analyzing degradation effects of organic light-emitting diodes via transient optical and electrical measurements.” In: *Journal of Applied Physics* 117.21 (2015). ISSN: 10897550. DOI: `10.1063/1.4921829`. URL: `http://dx.doi.org/10.1063/1.4921829`.

[90] C. A. Amorim, M. R. Cavallari, G. Santos, F. J. Fonseca, A. M. Andrade, and S. Mergulhão. “Determination of carrier mobility in MEH-PPV thin-films by stationary and transient current techniques.” In: *Journal of Non-Crystalline Solids* 358.3 (2012), pp. 484–491. ISSN: 00223093. DOI: `10.1016/j.jnoncrysol.2011.11.001`. URL: `http://dx.doi.org/10.1016/j.jnoncrysol.2011.11.001`.

[91] Bingjun Wang, Hao Ye, Moritz Riede, and Donal D.C. Bradley. “Chain conformation control of fluorene-benzothiadiazole copolymer light-emitting diode efficiency and lifetime.” In: *ACS Applied Materials and Interfaces* 13.2 (2021), pp. 2919–2931. ISSN: 19448252. DOI: `10.1021/acsami.0c18490`.

[92] S. Jenatsch, S. Züfle, B. Blülle, and B. Ruhstaller. "Combining steady-state with frequency and time domain data to quantitatively analyze charge transport in organic light-emitting diodes." In: *Journal of Applied Physics* 127.3 (2020). ISSN: 10897550. DOI: 10.1063/1.5132599.

[93] Fluxim AG. "Fluxim AG, Switzerland, see www.fluxim.com for simulation software Setfos." In: ().

[94] S. Altazin, C. Kirsch, E. Knapp, A. Stous, and B. Ruhstaller. "Refined drift-diffusion model for the simulation of charge transport across layer interfaces in organic semiconductor devices." In: *Journal of Applied Physics* 124.13 (2018). ISSN: 10897550. DOI: 10.1063/1.5043245.

[95] Francesco Santoni, Thomas Brown, Francesca Brunetti, Sara Pescetelli, Andrea Reale, Aldo Di Carlo, and Matthias Auf Der Maur. "A universal drift-diffusion simulator and its application to OLED simulations." In: *Proceedings of the International Conference on Numerical Simulation of Optoelectronic Devices, NUSOD* (2017), pp. 103–104. ISSN: 21583234. DOI: 10.1109/NUSOD.2017.8010012.

[96] S. Altazin, S. Züfle, E. Knapp, C. Kirsch, T. D. Schmidt, L. Jäger, Y. Noguchi, W. Brütting, and B. Ruhstaller. "Simulation of OLEDs with a polar electron transport layer." In: *Organic Electronics* 39 (2016), pp. 244–249. ISSN: 15661199. DOI: 10.1016/j.orgel.2016.10.014.

[97] Fluxim. "Setfos Manual - Fluxim AG, Switzerland, see www.fluxim.com for simulation software." In: ().

[98] P Langevin. "Recombinaison et mobilites des ions dans les gaz." In: *Annal. Chim. Phys.* 28.433 (1903).

[99] Wolfgang Tress. *Organic Solar Cells*. Vol. 39. 12. 2014, P–458–P–464. ISBN: 9783319100968. DOI: 10.2115/fiber.39.12_P458.

[100] Carlo Jacoboni. *Theory of Electron Transport in Semiconductors*. Vol. 53. 9. 2013, pp. 1689–1699. ISBN: 9788578110796. arXiv: arXiv:1011.1669v3.

[101] Hyunsu Cho, Jin Chung, Jinouk Song, Jaeho Lee, Hyunkoo Lee, Jonghee Lee, Jaehyun Moon, Seunghyup Yoo, and Nam Sung Cho. "Importance of Purcell factor for optimizing structure of organic light-emitting diodes." In: *Optics Express* 27.8 (2019), p. 11057. ISSN: 10944087. DOI: 10.1364/oe.27.011057.

[102] Stefano Sem, Sandra Jenatsch, Kleitos Stavrou, Andrew Danos, Andrew P. Monkman, and Beat Ruhstaller. "Determining non-radiative decay rates in TADF compounds using coupled transient and steady state optical data." In: *Journal of Materials Chemistry C* 10.12 (2022), pp. 4878–4885. ISSN: 20507534. DOI: 10.1039/d1tc05594a.

[103] T. J. Penfold, F. B. Dias, and A. P. Monkman. "The theory of thermally activated delayed fluorescence for organic light emitting diodes." In: *Chemical Communications* 54.32 (2018), pp. 3926–3935. ISSN: 1364548X. DOI: `10.1039/c7cc09612g`.

[104] Matthias Hempe, Nadzeya A. Kukhta, Andrew Danos, Mark A. Fox, Andrei S. Batsanov, Andrew P. Monkman, and Martin R. Bryce. "Vibrational Damping Reveals Vibronic Coupling in Thermally Activated Delayed Fluorescence Materials." In: *Chemistry of Materials* 33.9 (2021), pp. 3066–3080. ISSN: 15205002. DOI: `10.1021/acs.chemmater.0c03783`.

[105] Carlos Baleizão and Mário N. Berberan-Santos. "Thermally activated delayed fluorescence as a cycling process between excited singlet and triplet states: Application to the fullerenes." In: *Journal of Chemical Physics* 126.20 (2007). ISSN: 00219606. DOI: `10.1063/1.2734974`.

[106] Nils Haase, Andrew Danos, Christof Pflumm, Antonia Morherr, Patrycja Stachelek, Amel Mekic, Wolfgang Brütting, and Andrew P. Monkman. "Kinetic Modeling of Transient Photoluminescence from Thermally Activated Delayed Fluorescence." In: *Journal of Physical Chemistry C* 122.51 (2018), pp. 29173–29179. ISSN: 19327455. DOI: `sni`.

[107] Youichi Tsuchiya et al. "Exact Solution of Kinetic Analysis for Thermally Activated Delayed Fluorescence Materials." In: *Journal of Physical Chemistry A* 125.36 (2021), pp. 1–41. ISSN: 15205215. DOI: `10.1021/acs.jpca.1c04056`. URL: `https://chemrxiv.org/articles/preprint/Exact{\_}Solution{\_}of{\_}Kinetic{\_}Analysis{\_}for{\_}Thermally{\_}Activated{\_}Delayed{\_}Fluorescence{\_}Materials/14178113`.

[108] Ricardo Javier Vázquez, Ju Hui Yun, Angelar K. Muthike, Madeleine Howell, Hyungjun Kim, Ifeanyi K. Madu, Taesu Kim, Paul Zimmerman, Jun Yeob Lee, and Theodore Goodson Iii. "New Direct Approach for Determining the Reverse Intersystem Crossing Rate in Organic Thermally Activated Delayed Fluorescent (TADF) Emitters." In: *Journal of the American Chemical Society* 142.18 (2020), pp. 8074–8079. ISSN: 15205126. DOI: `10.1021/jacs.0c01225`.

[109] Ting An Lin et al. "Sky-Blue Organic Light Emitting Diode with 37% External Quantum Efficiency Using Thermally Activated Delayed Fluorescence from Spiroacridine-Triazine Hybrid." In: *Advanced Materials* 28.32 (2016), pp. 6976–6983. ISSN: 15214095. DOI: `10.1002/adma.201601675`.

[110] Jung Min Ha, Seon Hyoung Hur, Ambika Pathak, Ji Eun Jeong, and Han Young Woo. "Recent advances in organic luminescent materials with narrowband emission." In: *NPG Asia Materials*

13.1 (2021). ISSN: 18844057. DOI: 10.1038/s41427-021-00318-8. URL: http://dx.doi.org/10.1038/s41427-021-00318-8.

[111] Michael Y. Wong and Eli Zysman-Colman. "Purely Organic Thermally Activated Delayed Fluorescence Materials for Organic Light-Emitting Diodes." In: *Advanced Materials* 29.22 (2017). ISSN: 15214095. DOI: 10.1002/adma.201605444.

[112] B. Perucco, N. A. Reinke, D. Rezzonico, E. Knapp, S. Harkema, and B. Ruhstaller. "On the exciton profile in OLEDs-seamless optical and electrical modeling." In: *Organic Electronics* 13.10 (2012), pp. 1827–1835. ISSN: 15661199. DOI: 10.1016/j.orgel.2012.05.053. URL: http://dx.doi.org/10.1016/j.orgel.2012.05.053.

[113] Piotr Pander, Przemyslaw Data, and Fernando B. Dias. "Time-resolved photophysical characterization of triplet-harvesting organic compounds at an oxygen-free environment using an iCCD camera." In: *Journal of Visualized Experiments* 2018.142 (2018), pp. 1–9. ISSN: 1940087X. DOI: 10.3791/56614.

[114] Yun Long, Masashi Mamada, Chunyong Li, Paloma Lays Dos Santos, Marco Colella, Andrew Danos, Chihaya Adachi, and Andrew Monkman. "Excited State Dynamics of Thermally Activated Delayed Fluorescence from an Excited State Intramolecular Proton Transfer System." In: *Journal of Physical Chemistry Letters* 11.9 (2020), pp. 3305–3312. ISSN: 19487185. DOI: 10.1021/acs.jpclett.0c00498.

[115] Fernando B. Dias, Thomas J. Penfold, Mário N. Berberan-Santos, and Andrew P. Monkman. "Photophysics of Thermally Activated Delayed Fluorescence in Organic Molecules." In: (2018), pp. 227–261. DOI: 10.1142/9789813230194_0006.

[116] Otto Schmidt. "The mechanism of heterogeneous catayltic organic reactions. I. Catalytic hydrogenation." In: *Chemical Reviews* 12.3 (1933), pp. 363–417. ISSN: 15206890. DOI: 10.1021/cr60043a001.

[117] Ricardo Javier Vázquez, Hyungjun Kim, Paul M. Zimmerman, and Theodore Goodson. "Using ultra-fast spectroscopy to probe the excited state dynamics of a reported highly efficient thermally activated delayed fluorescence chromophore." In: *Journal of Materials Chemistry C* 7.14 (2019), pp. 4210–4221. ISSN: 20507526. DOI: 10.1039/c8tc05957h.

[118] Tomas Serevičius, Rokas Skaisgiris, Gediminas Kreiza, Jelena Dodonova, Karolis Kazlauskas, Edvinas Orentas, Sigitas Tumkevičius, and Saulius Juršenas. "TADF parameters in the solid state: An easy way to draw wrong conclusions." In: *Journal of Physical Chemistry A* 125.7 (2021), pp. 1637–1641. ISSN: 15205215. DOI: 10.1021/acs.jpca.0c10391.

[119] Monirul Hasan, Atul Shukla, Viqar Ahmad, Jan Sobus, Fatima Bencheikh, Sarah K.M. McGregor, Masashi Mamada, Chihaya Adachi, Shih Chun Lo, and Ebinazar B. Namdas. "Exciton–Exciton Annihilation in Thermally Activated Delayed Fluorescence Emitter." In: *Advanced Functional Materials* 2000580 (2020), pp. 1–8. ISSN: 16163028. DOI: 10.1002/adfm.202000580.

[120] Markus Regnat, Kurt P. Pernstich, and Beat Ruhstaller. "Influence of the Bias-dependent Emission Zone on Exciton Quenching and OLED Efficiency." In: *Organic Electronics* 70.April (2019), pp. 219–226. ISSN: 15661199. DOI: 10.1016/j.orgel.2019.04.027. URL: https://linkinghub.elsevier.com/retrieve/pii/S1566119919301922.

[121] Sebastian Wehrmeister, Lars Jäger, Thomas Wehlus, Andreas F. Rausch, Thilo C.G. Reusch, Tobias D. Schmidt, and Wolfgang Brütting. "Combined electrical and optical analysis of the efficiency roll-off in phosphorescent organic light-emitting diodes." In: *Physical Review Applied* 3.2 (2015), pp. 1–10. ISSN: 23317019. DOI: 10.1103/PhysRevApplied.3.024008.

[122] Simon Zeder, Christoph Kirsch, Urs Aeberhard, Balthasar Blülle, Sandra Jenatsch, and Beat Ruhstaller. "Coupled 3D master equation and 1D drift-diffusion approach for advanced OLED modeling." In: *Journal of the Society for Information Display* 28.5 (2020), pp. 440–449. ISSN: 19383657. DOI: 10.1002/jsid.903.

[123] Vygintas Jankus, Przemyslaw Data, David Graves, Callum McGuinness, Jose Santos, Martin R. Bryce, Fernando B. Dias, and Andrew P. Monkman. "Highly efficient TADF OLEDs: How the emitter-host interaction controls both the excited state species and electrical properties of the devices to achieve near 100% triplet harvesting and high efficiency." In: *Advanced Functional Materials* 24.39 (2014), pp. 6178–6186. ISSN: 16163028. DOI: 10.1002/adfm.201400948.

[124] Qianqian Du, Wenjun Wang, Shuhong Li, Dong Zhang, Wenlian Li, and Wanquan Zheng. "Study on blue organic light-emitting diodes doped with 4,4′-bis (9-ethyl-3carbazovinylene)-1,1′-biphenyl in various host materials." In: *Optics Communications* 366 (2016), pp. 253–259. ISSN: 00304018. DOI: 10.1016/j.optcom.2015.12.074. URL: http://dx.doi.org/10.1016/j.optcom.2015.12.074.

[125] S. J. He, Z. B. Wang, D. K. Wang, N. Jiang, and Z. H. Lu. "Highly efficient blue fluorescent organic light-emitting diodes with a high emitter/host ratio." In: *Applied Physics Letters* 103.8 (2013). ISSN: 00036951. DOI: 10.1063/1.4819155.

[126] Neng Liu, W. X. Shi, Y. M. Zhou, and X. A. Cao. "Impact of Dopant Aggregation on the EL of Blue Fluorescent Host-Dopant Emitters." In: *IEEE Electron Device Letters* 40.5 (2019), pp. 750–753. ISSN: 15580563. DOI: 10.1109/LED.2019.2908194.

[127] Hyung Suk Kim, So Ra Park, and Min Chul Suh. "Actual interpretation of concentration quenching effect on thermally activated delayed fluorescence in a solid film." In: *Digest of Technical Papers - SID International Symposium* 49.1 (2018), pp. 1842–1845. ISSN: 21680159. DOI: 10.1002/sdtp.12430.

[128] Yuichiro Kawamura, Kenichi Goushi, Jason Brooks, Julie J. Brown, Hiroyuki Sasabe, and Chihaya Adachi. "100% phosphorescence quantum efficiency of Ir (III) complexes in organic semiconductor films." In: *Applied Physics Letters* 86.7 (2005), pp. 1–3. ISSN: 00036951. DOI: 10.1063/1.1862777.

[129] Kwon Hyeon Kim, Chang Ki Moon, Jeong Hwan Lee, Sei Yong Kim, and Jang Joo Kim. "Highly efficient organic light-emitting diodes with phosphorescent emitters having high quantum yield and horizontal orientation of transition dipole moments." In: *Advanced Materials* 26.23 (2014), pp. 3844–3847. ISSN: 15214095. DOI: 10.1002/adma.201305733.

[130] Xiaoqing Zhang, Canek Fuentes-Hernandez, Yadong Zhang, Matthew W. Cooper, Stephen Barlow, Seth R. Marder, and Bernard Kippelen. "High performance blue-emitting organic light-emitting diodes from thermally activated delayed fluorescence: A guest/host ratio study." In: *Journal of Applied Physics* 124.5 (2018). ISSN: 10897550. DOI: 10.1063/1.5041447.

[131] S. Züfle, S. Altazin, A. Hofmann, L. Jäger, M. T. Neukom, W. Brütting, and B. Ruhstaller. "Determination of charge transport activation energy and injection barrier in organic semiconductor devices." In: *Journal of Applied Physics* 122.11 (2017). ISSN: 10897550. DOI: 10.1063/1.4992041.

[132] V. Savvate'ev, J. H. Friedl, L. Zou, J. Shinar, K. Christensen, W. Oldham, L. J. Rothberg, Z. Chen-Esterlit, and R. Kopelman. "Nanosecond transients in the electroluminescence from multilayer blue organic light-emitting devices based on 4,4'-bis(2,2'diphenyl vinyl)-1,1'-biphenyl." In: *Applied Physics Letters* 76.12 (2000), pp. 1501–1503. ISSN: 00036951. DOI: 10.1063/1.126076.

[133] Zhi Qiang Zhang, Yi Peng Liu, Yan Feng Dai, Jiang Shan Chen, Dong Ge Ma, and Hong Mei Zhang. "High-efficiency phosphorescent white organic light-emitting diodes with stable emission spectrum based on RGB separately monochromatic emission layers." In: *Chinese Physics Letters* 31.4 (2014). ISSN: 17413540. DOI: 10.1088/0256-307X/31/4/046801.

[134] R. Coehoorn, X. Lin, C. H.L. Weijtens, S. Gottardi, and H. Van Eersel. “Three-Dimensional Modeling of Organic Light-Emitting Diodes Containing Molecules with Large Electric Dipole Moments.” In: *Physical Review Applied* 16.3 (2021), p. 1. ISSN: 23317019. DOI: `10.1103/PhysRevApplied.16.034048`. URL: `https://doi.org/10.1103/PhysRevApplied.16.034048`.

[135] Nils Haase, Andrew Danos, Christof Pflumm, Patrycja Stachelek, Wolfgang Brütting, and Andrew P. Monkman. “Are the rates of dexter transfer in TADF hyperfluorescence systems optically accessible?” In: *Materials Horizons* 8.6 (2021), pp. 1805–1815. ISSN: 20516355. DOI: `10.1039/d0mh01666g`.

[136] Daniele Rezzonico. “Numerical analysis of exciton dynamics in organic light-emitting devices and solar cells.” In: *Journal of Photonics for Energy* 1.1 (2011), p. 011005. ISSN: 1947-7988. DOI: `10.1117/1.3528045`.

[137] Chaoyu Xiang, Wonhoe Koo, Franky So, Hisahiro Sasabe, and Junji Kido. “A systematic study on efficiency enhancements in phosphorescent green, red and blue microcavity organic light emitting devices.” In: *Light: Science and Applications* 2.JUNE (2013), pp. 1–7. ISSN: 20477538. DOI: `10.1038/lsa.2013.30`.

[138] Qisheng Zhang, Takeshi Komino, Shuping Huang, Shigeyuki Matsunami, Kenichi Goushi, and Chihaya Adachi. “Triplet exciton confinement in green organic light-emitting diodes containing luminescent charge-transfer Cu(I) complexes.” In: *Advanced Functional Materials* 22.11 (2012), pp. 2327–2336. ISSN: 1616301X. DOI: `10.1002/adfm.201101907`.

[139] Jing Zhang, Dongxue Ding, Ying Wei, and Hui Xu. “Extremely condensing triplet states of DPEPO-type hosts through constitutional isomerization for high-efficiency deep-blue thermally activated delayed fluorescence diodes.” In: *Chemical Science* 7.4 (2016), pp. 2870–2882. ISSN: 20416539. DOI: `10.1039/c5sc04848f`.

[140] Thomas D. Anthopoulos, Jonathan P.J. Markham, Ebinazar B. Namdas, Ifor D.W. Samuel, Shih Chun Lo, and Paul L. Burn. “Highly efficient single-layer dendrimer light-emitting diodes with balanced charge transport.” In: *Applied Physics Letters* 82.26 (2003), pp. 4824–4826. ISSN: 00036951. DOI: `10.1063/1.1586999`.

[141] Jing Wang et al. “High efficiency green phosphorescent organic light-emitting diodes with a low roll-off at high brightness.” In: *Organic Electronics* 14.11 (2013), pp. 2854–2858. ISSN: 15661199. DOI: `10.1016/j.orgel.2013.08.006`. URL: `http://dx.doi.org/10.1016/j.orgel.2013.08.006`.

[142] Fuh Shyang Juang, Chang Chi Lee, Jeng Yue Chen, Yen Hua Lin, and Ding Wen Zhang. “Lifetime study for solution processed organic light emitting diodes.” In: *IOP Conference Series: Materials Science and Engineering* 600.1 (2019). ISSN: 1757899X. DOI: 10.1088/1757-899X/600/1/012018.

[143] Yutaka Noguchi, Yukimasa Miyazaki, Yuya Tanaka, Naoki Sato, Yasuo Nakayama, Tobias D. Schmidt, Wolfgang Brütting, and Hisao Ishii. “Charge accumulation at organic semiconductor interfaces due to a permanent dipole moment and its orientational order in bilayer devices.” In: *Journal of Applied Physics* 111.11 (2012). ISSN: 00218979. DOI: 10.1063/1.4724349.

[144] Yutaka Noguchi, Yuya Tanaka, Yukimasa Miyazaki, Naoki Sato, Yasuo Nakayama, and Hisao Ishii. “Displacement Current Measurement for Exploring Charge Carrier Dynamics in Organic Semiconductor Devices.” In: *Physics of Organic Semiconductors: Second Edition*. 2013, pp. 119–154. ISBN: 9783527410538. DOI: 10.1002/9783527654949.ch5.

[145] John S. Bangsund, Jack R. Van Sambeek, Nolan M. Concannon, and Russell J. Holmes. “Sub-turn-on exciton quenching due to molecular orientation and polarization in organic light-emitting devices.” In: *Science Advances* 6.32 (2020), pp. 1–11. ISSN: 23752548. DOI: 10.1126/sciadv.abb2659.

[146] Pascal Friederich, Vadim Rodin, Florian Von Wrochem, and Wolfgang Wenzel. “Built-In Potentials Induced by Molecular Order in Amorphous Organic Thin Films.” In: *ACS Applied Materials and Interfaces* 10.2 (2018), pp. 1881–1887. ISSN: 19448252. DOI: 10.1021/acsami.7b11762.

[147] Caroline Murawski, Karl Leo, and Malte C. Gather. “Efficiency roll-off in organic light-emitting diodes.” In: *Advanced Materials* 25.47 (2013), pp. 6801–6827. ISSN: 09359648. DOI: 10.1002/adma.201301603.

[148] Bas van der Zee, Yungui Li, Gert Jan A.H. Wetzelaer, and Paul W.M. Blom. “Origin of the Efficiency Roll-Off in Single-Layer Organic Light-Emitting Diodes Based on Thermally Activated Delayed Fluorescence.” In: *Advanced Optical Materials* 9.19 (2021). ISSN: 21951071. DOI: 10.1002/adom.202100249.

[149] Takashi Kobayashi, Akitsugu Niwa, Kensho Takaki, Shota Haseyama, Takashi Nagase, Kenichi Goushi, Chihaya Adachi, and Hiroyoshi Naito. “Contributions of a Higher Triplet Excited State to the Emission Properties of a Thermally Activated Delayed-Fluorescence Emitter.” In: *Physical Review Applied* 7.3 (2017), pp. 1–10. ISSN: 23317019. DOI: 10.1103/PhysRevApplied.7.034002.

[150] H. Van Eersel, P. A. Bobbert, R. A.J. Janssen, and R. Coehoorn. "Monte Carlo study of efficiency roll-off of phosphorescent organic light-emitting diodes: Evidence for dominant role of triplet-polaron quenching." In: *Applied Physics Letters* 105.14 (2014), pp. 1–6. ISSN: 00036951. DOI: `10.1063/1.4897534`.

[151] Arnout Ligthart, Xander de Vries, Le Zhang, Mike C.W.M. Pols, Peter A. Bobbert, Harm van Eersel, and Reinder Coehoorn. "Effect of Triplet Confinement on Triplet–Triplet Annihilation in Organic Phosphorescent Host–Guest Systems." In: *Advanced Functional Materials* 28.52 (2018), pp. 1–10. ISSN: 16163028. DOI: `10.1002/adfm.201804618`.

[152] L. Zhang, H. van Eersel, P. A. Bobbert, and R. Coehoorn. "Analysis of the phosphorescent dye concentration dependence of triplet-triplet annihilation in organic host-guest systems." In: *Chemical Physics Letters* 662 (2016), pp. 221–227. ISSN: 00092614. DOI: `10.1016/j.cplett.2016.07.048`. URL: `http://dx.doi.org/10.1016/j.cplett.2016.07.048`.

[153] Takuya Kawata et al. "Highly efficient OLED devices with device architecture for reducing drive voltage." In: *Digest of Technical Papers - SID International Symposium* 44.1 (2013), pp. 685–688. ISSN: 21680159. DOI: `10.1002/j.2168-0159.2013.tb06305.x`.

[154] Jianping Zhang, Fang Liu, Yu Liu, Helen Wu, Wenli Wu, and Aixi Zhou. "A study of accelerated life test of white OLED based on maximum likelihood estimation using lognormal distribution." In: *IEEE Transactions on Electron Devices* 59.12 (2012), pp. 3401–3404. ISSN: 00189383. DOI: `10.1109/TED.2012.2215864`.

[155] E. Nogueira, V. Orlando, J. Ochoa, A. Fernandez, and M. Vazquez. "Accelerated Life Test of high luminosity blue LEDs." In: *Microelectronics Reliability* 64 (2016), pp. 631–634. ISSN: 00262714. DOI: `10.1016/j.microrel.2016.07.021`. URL: `http://dx.doi.org/10.1016/j.microrel.2016.07.021`.

[156] Toshihiro Yoshioka, Kazunori Sugimoto, Hiroshi Ohata, Satoshi Miyaguchi, and Tetsuo Tsutsui. "Comprehensive analysis of luminous decay curves for accelerated lifetime testing of OLEDs." In: *Digest of Technical Papers - SID International Symposium* 46.Book 3 (2015), pp. 1650–1653. ISSN: 21680159. DOI: `10.1002/sdtp.10149`.

[157] Toshihiro Yoshioka, Kazunori Sugimoto, Kyoko Katagi, Yoshiyuki Kitago, Masaru Tajima, Satoshi Miyaguchi, Tetsuo Tsutsui, Ryota Iwasaki, and Yukio Furukawa. "An improved method for lifetime prediction based on decoupling of the joule self-heating effect from coulombic degradation in accelerated aging tests of OLEDs." In: *Digest of Technical Papers - SID Interna-*

tional Symposium 45.1 (2014), pp. 642–645. ISSN: 21680159. DOI: 10.1002/j.2168-0159.2014.tb00168.x.

[158] Chemical Materials Evaluation and P-K Sugimoto. “Accelerated Lifetime Testing of White OLED Panels for Lighting Kazunori Sugimoto *, Toshihiro Yoshioka *, Hiroaki Kijima *, Hiroshi Ohata * Satoshi Miyaguchi *, Tetsuo Tsutsui *, Noriyuki Takada * , **, Hideyuki Murata ***.” In: 4 (2016), pp. 1730–1733.

[159] Bomi Sim, Jong Soo Kim, Hyejin Bae, Sungho Nam, Eunsuk Kwon, Ji Whan Kim, Hwa Young Cho, Sunghan Kim, and Jang Joo Kim. “Comprehensive model of the degradation of organic light-emitting diodes and application for efficient, stable blue phosphorescent devices with reduced influence of polarons.” In: *Physical Review Applied* 14.2 (2020), p. 1. ISSN: 23317019. DOI: 10.1103/PhysRevApplied.14.024002. arXiv: 1912.05073. URL: https://doi.org/10.1103/PhysRevApplied.14.024002.

[160] Jiho Sohn, Donghyun Ko, Hyunho Lee, Jongseok Han, Sin Doo Lee, and Changhee Lee. “Degradation mechanism of blue thermally activated delayed fluorescent organic light-emitting diodes under electrical stress.” In: *Organic Electronics* 70.February (2019), pp. 286–291. ISSN: 15661199. DOI: 10.1016/j.orgel.2019.04.033. URL: https://doi.org/10.1016/j.orgel.2019.04.033.

[161] Monirul Hasan, Siddhartha Saggar, Atul Shukla, Fatima Bencheikh, Jan Sobus, Sarah K.M. McGregor, Chihaya Adachi, Shih Chun Lo, and Ebinazar B. Namdas. “Probing polaron-induced exciton quenching in TADF based organic light-emitting diodes.” In: *Nature Communications* 13.1 (2022), pp. 1–7. ISSN: 20411723. DOI: 10.1038/s41467-021-27739-x.

[162] Yutaka Noguchi, Hyung Jun Kim, Ryuta Ishino, Kenichi Goushi, Chihaya Adachi, Yasuo Nakayama, and Hisao Ishii. “Charge carrier dynamics and degradation phenomena in organic light-emitting diodes doped by a thermally activated delayed fluorescence emitter.” In: *Organic Electronics* 17 (2015), pp. 184–191. ISSN: 15661199. DOI: 10.1016/j.orgel.2014.12.009. URL: http://dx.doi.org/10.1016/j.orgel.2014.12.009.